Experimental Investigation of Surface Pressure Fluctuations in a Laminar Separation Bubble Using Piezoelectric Sensor Array

Lorenzo Belli

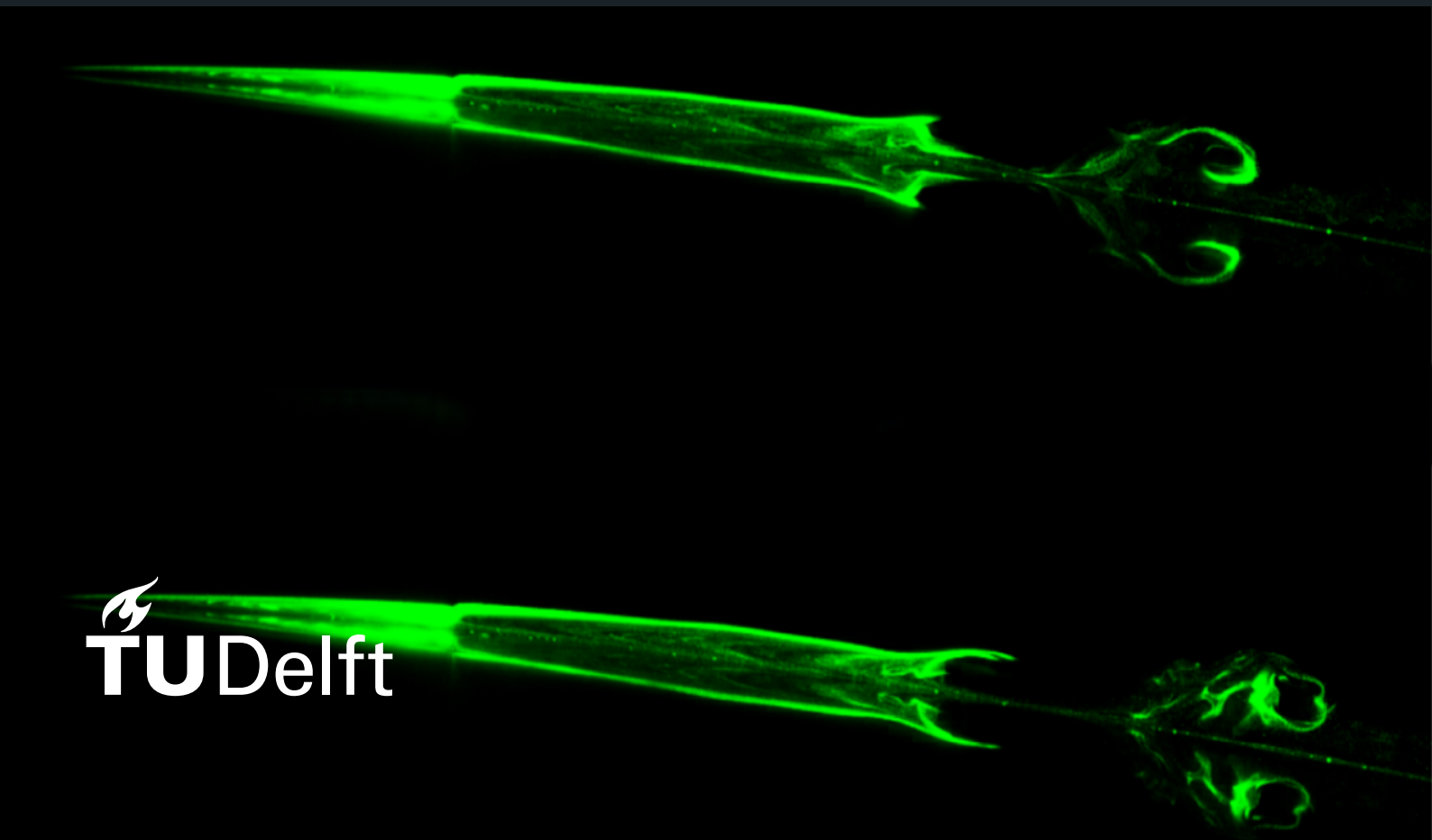

TU Delft

Experimental Investigation of Surface Pressure Fluctuations in a Laminar Separation Bubble Using Piezoelectric Sensor Array

Thesis report

by

Lorenzo Belli

to obtain the degree of Master of Science
at the Delft University of Technology
to be defended publicly on November 25, 2025 at 10:00

Thesis committee:

Chair:	Prof.dr.ir. Leo Veldhuis
Supervisors:	Dr.ir. Theo Michelis
	Prof. Dr.-Ing. Julien Weiss
External examiner:	Prof.dr.ir. Andrea Sciacchitano
Place:	Faculty of Aerospace Engineering, Delft
Project Duration:	March, 2025 - November, 2025
Student number:	6069118

An electronic version of this thesis is available at `http://repository.tudelft.nl/`.

Cover picture: Smoke flow of a laminar separation bubble from Kurelek et al. [1]

Faculty of Aerospace Engineering · Delft University of Technology

Preface

Thanking the plethora of dramatis personae who have accompanied me throughout this nine-months journey, and throughout the entire master's program, is easier said than done. To attempt it would risk producing a dry list of names, stripped of the emotions and memories each of them evokes. Nonetheless, I cannot refrain from expressing my gratitude to those who played a particularly meaningful role in the completion of this thesis.

First and foremost, gratitude to my supervisor, Theo Michelis, whose support, availability, and sense of humor have been invaluable.

My sincere thanks go to Julien Wiess, my supervisor at TU Berlin, without whose guidance this journey would never have begun.

I am also deeply indebted to Cosimo Corsi, PhD candidate at TU Berlin, without whom this project could not have reached its conclusion. His guidance, both in the depths of aerodynamics and in the mysterious dynamics of memes, was nothing short of essential.

Finally, my heartfelt thanks to the TU Berlin laboratory staff and the other PhD candidates, especially Bülent, whose presence was always a relieving sight during the countless hours of troubleshooting.

Ultimi ma non per importanza, il più grato dei ringraziamenti ai miei genitori e alla mia famiglia, il cui sostegno costante e incondizionato mi ha spinto a cercare, in ogni aspetto della vita, la direzione ostinata e contraria e a guardare dietro la faccia abusata delle cose, rendendomi la persona che sono oggi.

Abstract

Laminar separation bubbles (LSBs) play a crucial role in determining the aerodynamic performance of airfoils operating at low Reynolds numbers, conditions commonly encountered by unmanned aerial vehicles (UAVs), wind turbines, and small aircraft. Their inherently unsteady nature significantly influences lift, drag, and noise generation. This thesis investigates the dynamic behavior of LSBs that forms on the suction side of a NACA 0015 airfoil through surface pressure measurements obtained using piezoelectric sensors (”piezofoils”) integrated into a wing model tested in the Boundary Layer Wind Tunnel of the Technische Universität Berlin. The device are tested at chord-based Reynolds numbers of 144,000, 197,000 and 262,000 and at angles of attack comprised between 1 and 5 degrees, in 1 degree increments. Two different piezofoil designs are used, ”in-line”, spanning most of the airfoil chord and ”staggered”, shorter but with an improved spatial resolution. Complementary measurements are performed using surface hot wire anemometry, oil flow visualization, and surface pressure taps to provide a comprehensive characterization of both mean and fluctuating flow features.

The primary objective of the study is to relate the surface pressure fluctuations within the LSB to its dynamic phenomena, specifically, shear-layer flapping and vortex shedding, and to identify the optimal sensor placement for their detection. The existence and the characteristics of the laminar separation bubbles at the range of Reynolds number and angles of attack considered is confirmed through surface pressure measurements using pressure transducers and oil flow visualization. Analysis of the spectra and of the standard deviation in the separation and reattachment regions demonstrates that the piezofoil sensor successfully detects and accurately resolves vortex shedding, but is unable to capture the low-frequency flapping motion. The cross correlation analysis provided further insight into the vortex shedding process, enabling the estimation of the convective velocity and streamwise wavelength of the vortical structures. Heating of the piezofoil and appropriate signal filtering are found to be effective in enhancing the signal-to-noise ratio and mitigating electromagnetic interference effects.

Contents

Nomenclature

List of Abbreviations

DNS	Direct Numerical Simulation
HWA	Hot Wire Anemometry
LSB	Laminar Separation Bubble
MFD	Mean Flow Deformation
P(VDF-TrFE)	Poly(VinyliDeneFluoride-TriFluoroEthylene)
PE	Polyethylene
PIV	Particle Image Velocimetry
PLLA	Poly-L-Lactic Acid
PMMA	PolyMethyl-MethAcrylate
PSD	Power Spectral Density
PSP	Pressure Sensitive Paint
PVDF	PolyVinyliDine Fluoride
STD	Standard Deviation
TI	Turbulence Intensity
TS	Tollmien-Schlichting
UAV	Unmanned Aerial Vehicle

List of Symbols

$(l/c)_{LSB}$	Non-dimensional length of the LSB
$(R_{\delta^*})_s$	Boundary layer displacement thickness Reynolds number at separation
$(R_{\theta^*})_s$	Boundary layer momentum thickness Reynolds number at separation
α	Angle of attack
$\bar{x_r}$	Mean reattachment point
$\bar{x_r}/c$	Non-dimensional mean reattachment point
$\bar{x_s}$	Mean separation point
$\bar{x_s}/c$	Non-dimensional mean separation point
$\bar{x_t}$	Mean transition point
$\bar{x_t}/c$	Non-dimensional mean transition point
$\Delta T_{pz-\infty}$	Temperature difference between piezo-foil and freestream
λ_x/δ_s^*	Chordwise wavelength normalized on boundary layer displacement thickness at separation
λ_z/δ_s^*	Spanwise wavelength normalized on boundary layer displacement thickness at separation
λ_z/λ_x	Spanwise to streamwise wavelength ratio
σ	Standard deviation
σ/σ_t	Non-dimensional standard deviation
$\varnothing$	Diameter
$C_{xy}(f)$	Magnitude-squared coherence function of $x(t)$ and $y(t)$
Cp	Pressure coefficient
D_k	Electric displacement
d_{kij}	Piezoelectric charge constant
d^*_{kij}	Piezoelectric strain constant
E_k	Electric field
f	Frequency
f^*	Non-dimensional frequency normalized to the freestream velocity
f_0^*	Central disturbance frequency
f_{vs}	Vortex shedding frequency
$G_{nn}(f)$	Power spectral density of $n(t)$
$G_{xx}(f)$	Power spectral density of $x(t)$
$G_{yy}(f)$	Power spectral density of $y(t)$
l/δ_s^*	Total bubble length to boundary layer displacement thickness at separation
l_x	streamwise wavelength

l_z	Spanwise coherence
l_z/c	Non-dimensional spanwise coherence
$n(t)$	Fluctuating signal of the phenomenon of the single-input/single-output system
Re	Reynolds number
S_{ij}	Strain
St	Strouhal number
T_∞	Freestream Temperature
T_{ij}	Stress
$T_{piezofoil}$	Piezofoil Temperature
U_c	Convective velocity
U_c/U_e	Convective to edge velocity ratio
U_∞	Freestream Velocity
u_{rev}	Peak reverse flow velocity normalized to the freestream velocity
U_s	Velocity outside the boundary layer at separation
$x(t)$	Input of the single-input/single-output system
x/c	Non-dimensional x-coordinate
x_r/c	Non-dimensional mean reattachment point
x_t/c	Non-dimensional mean transition point
$y(t)$	Total output of the single-input/single-output system; $z(t) + n(t)$
$z(t)$	Output of the single-input/single-output system
z/c	Non-dimensional z-coordinate

List of Figures

List of Tables

1

Introduction

At low Reynolds numbers, below $Re = 500,000$, airfoil performance is strongly impacted by the presence of the laminar separation bubble (LSB). This phenomenon is characterized by boundary layer separation, flow transition in the separated shear layer and shear layer reattachment, creating an area of recirculating flow that alters the pressure distribution over the airfoil, detrimentally affecting lift and drag. At low Reynolds numbers the boundary layer can remain laminar past the suction peak and, when encountering the adverse pressure gradient, is more susceptible to separation than a turbulent one. When the boundary layer separates, the disturbances that have already started to be amplified in the boundary layer, further grow and develop through the Kelvin-Helmholtz instability. As these disturbances reach their maximum amplification they roll up into vortical structures that convect along the airfoil. These vortices, known as ”rollers”, are developed within the laminar separation bubble and play and important role in its characteristics. The rollers are the mechanism through which the separated shear layer reattaches to the surface, creating a turbulent boundary layer that extends until the trailing edge. Laminar separation bubbles are, hence, inherently unsteady and dynamic phenomena with areas of complex flow interaction. Figure 1.1 shows a snapshot of a laminar separation bubble over an airfoil, employing smoke flow visualization.

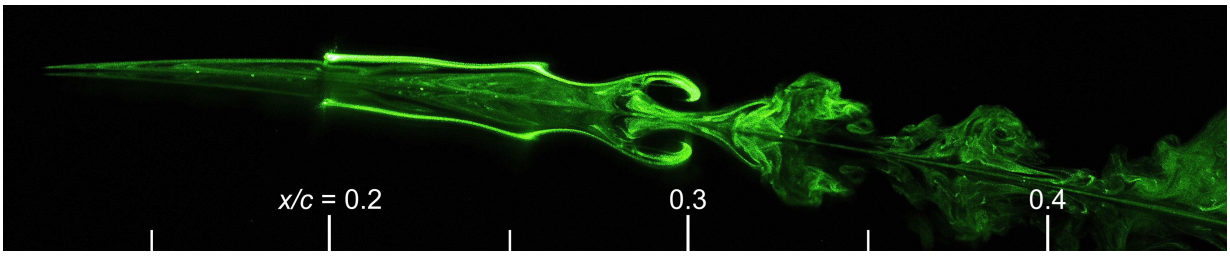

Figure 1.1: Smoke flow visualization of a laminar separation bubble over an airfoil. It can be clearly seen the point of flow separation and the roll up of vortical structures close to the flow reattachment point. [2]

In general, laminar separation bubbles are a topic of interest for all the applications where low Reynolds numbers are encountered, such as unmanned aerial vehicles (UAV), wind turbines, small manned aircraft or gliders. Speaking of UAVs, they have seen unprecedented level of growth in both civil and military applications, reaching in the last years a total market value of more than 16 billion dollars [3]. In civil applications UAVs are used in numerous scenarios such as firefighting and humanitarian aid, disaster response, border security, traffic surveillance and regulation, agricultural crop management, aerial photographing, logistics [3] [4]. Similarly, in the military sector UAVs use has gained momentum, especially since Operation Desert Storm during the First Gulf War in 1991, until recently where UAVs are used massively not only for reconnaissance and support but also for combat roles, as the Russo-Ukrainian war is demonstrating [5]. Speaking of wind turbines, they have become widely used as energy demand is growing and fossil fuels reduction is becoming central. Wind mills are one of the oldest energy harvesting technologies but it was only in the 1970s, with the oil crisis of 1973, that a large-scale wind energy penetration outbreak was encountered [6]. Wind farm installations have increased steadily in the last decades and wind turbines are now an extremely common view in many regions. Aerodynamically understanding of flow characteristics

formed over blades of wind turbines can increase the efficiency and the energy extraction from the flow. Investigations in this field are in priority because flow phenomena such as laminar separation bubbles directly affect the aerodynamic performance of turbines, their structural design and last but not least, noise. Hence, a deeper understanding of the flow features on the blade can help push the limits of this technology and encourage the transition to renewable energies.

Over the years, various flow measurement techniques have been employed to investigate laminar separation bubbles (LSBs). Some of these methods focus on measuring the velocity field within the bubble region, while others examine the wall effects induced by the LSB, such as changes in mean or fluctuating pressure, skin friction, or convective heat transfer. Among the available techniques, Particle Image Velocimetry (PIV) has become the most widely used for velocity measurements. PIV enables visualization of the flow velocity vectors over a plane defined by the laser sheet and the camera's field of view. However, the method involves several operational and setup complexities, including precise control of particle seeding, accurate alignment of laser optics and cameras, and the inherent difficulty of obtaining reliable measurements close to the surface. Microphones are another commonly used measurement device in studies of laminar separation bubbles, capable of resolving a wide range of pressure fluctuations with high frequency response. However, their use requires precise drilling of the installation surface and careful management of signal wiring, considerations that often make their integration impractical in model regions with limited internal space, such as wing trailing edges. Finally, hot wires and surface hot wires are also commonly employed measurement devices, capable of capturing flow characteristics in localized regions both near and away from the wall, with very high frequency response. However, conventional hot wire setups are unable to measure flow directionality, perform poorly in regions of low flow velocity, and are highly fragile due to the delicate nature of the sensing wires. A promising device for the study of the wall pressure fluctuations is the 'piezofoil', a thin foil with piezoelectric characteristics that is glued on a surface to investigate the surrounding flow behavior. Although the piezofoil is not a full-field measurement technique like PIV, it overcomes many of the major limitations associated with the aforementioned methods while maintaining good sensitivity and frequency response. As it is directly glued to the surface, the piezofoil can be utilized in regions with limited internal volume and requires no complex installation procedures. Its minimal thickness ensures negligible interference with the flow, and its screen-printing capability allows fabrication in virtually any desired shape and size. The present work focuses on the experimental investigation of laminar separation bubbles using the piezofoil, with the objective of assessing its advantages and limitations in subsonic flows characterized by complex and unsteady features.

1.1. Laminar Separation Bubble

In certain conditions, such as at high airfoils incidences angles and/or low Reynolds numbers, the laminar boundary layer can fail to remain attached to the surface, due to the influence of an adverse pressure gradient. The separated boundary layer can then either reattach or not. If the boundary layer fails to reattach, it becomes a shear layer between a turbulent wake and a laminar outer flow, leading the airfoil to the phenomenon of stall. The mechanism of stall on an airfoil is always caused by a separated boundary layer [7]. However, the laminar boundary layer can undergo transition to turbulence just after the separation point and subsequently reattach to the surface as a turbulent boundary layer, creating an area of recirculating flow, called ”laminar separation bubble” (LSB) [8]. Laminar separation bubbles are mainly found on airfoils but are also observed in other instances such as on circular cylinder under certain conditions and in the interaction between an oblique shock wave and a laminar boundary layer on a flat plate at supersonic speeds [9]. In the present work LSB will only be considered on airfoils. Laminar separation bubbles can have different effects on the performance of a lifting surface: first of all, the effect on lift depends on the size of the bubble: long bubbles (for the difference and the classification of short and long LSB see Section 1.1.1) will likely destroy the suction peak and thus reduce lift, if they are close enough to the leading edge. Short bubbles can have a positive effect on the lift generated due to the fact that the bubble give rise to an increase of the camber of the airfoil [10]. This effect can also be seen on the C_P plots of wings that have developed an LSB, as in Figure 1.2.

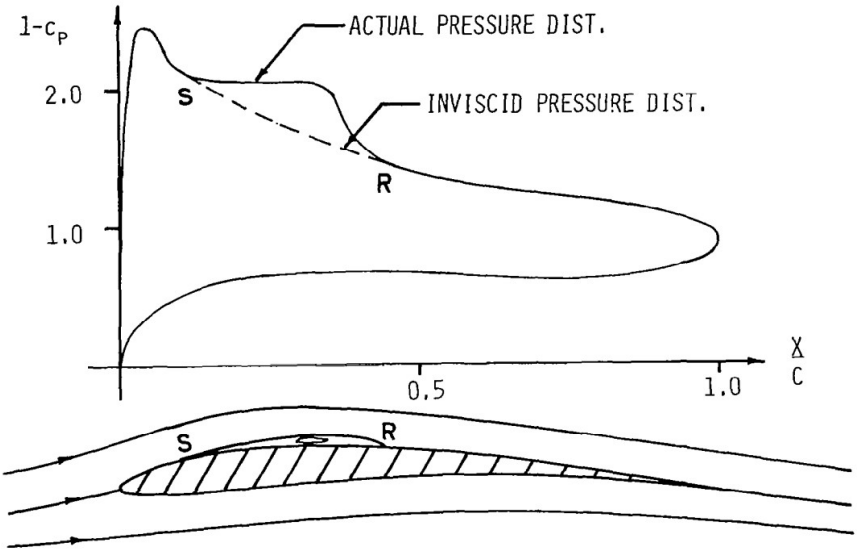

Figure 1.2: Pressure coefficient distribution in the inviscid case and considering the presence of a laminar separation bubble [11]

Speaking of drag, usually the laminar separation bubble brings an increase in drag: this is due to the increase in pressure drag that the bubble yields. The bigger the bubble, the bigger the negative effect on drag. Ultimately, if the bubble ”bursts” (for more on bursting see Section 1.1.3), transitioning from a ”shorter” state to a ”longer” state, the lifting surface can stall and a sudden increase of drag and loss of lift occur. It is worth to notice that the laminar separation bubble yields, as mentioned, an increase in pressure drag but a local decrease of friction drag or, in other words, the bubble generates a small thrust force due to the recirculation area inside it. This effect is usually negligible and is offset by the increase in pressure drag. Laminar separation bubbles are closely connected to the stall phenomena and are responsible for at least two different stall types: thin-airfoil stall and leading edge stall. Thin-airfoil stall, which not only pertains to thin airfoils, occurs when a laminar separation bubble start to expand downstream until when the flow is incapable of reattaching to the surface. At that point a turbulent wake forms and there is an instant loss of lift and a large increase in drag [7], [12], [13]. In the leading edge stall the mechanism is similar but more abrupt. Before the stall angle of attack is reached a small laminar separation bubble forms just after the suction peak. As the angle of attack increases the bubble move forward until the boundary layer is incapable of reattachment. The result is a very abrupt loss in lift and a the creation of a wake starting from the leading edge of the airfoil [7], [12], [13]. Another type of stall exist, the trailing edge stall.

In this case the mechanism is more gradual and it is connected to the progressive loss of momentum in the boundary layer near the wall. As the boundary layer progresses through the adverse pressure gradient region, it grows thicker and loses energy. At a certain angle of attack the boundary layer separated from the surface near the leading edge. Increasing the angle of attack further increases the adverse pressure gradient and thus moves the separation point upstream. Contextually a laminar separation bubble could form near the leading edge of the airfoil. With further increases of the angle of attack the two separated regions can merge creating a complete wake over the airfoil [7], [12], [13].

As can be seen, understanding and determining the behavior of the boundary layer plays an important role in the formation and classification of LSB and consequently in understanding negative dynamic behaviors such as the stalling characteristics of airfoils and noise production. In LSB noise is produced when vortical structures produced by the shear layer roll up, and still retaining sufficient strength and coherence, scatter at the trailing edge, leading to the radiation of sound waves [14].

LSB occur at relative low Reynolds numbers, approximately between $60,000 < Re < 500,000$, and thus are relevant for applications such as unmanned aerial vehicles, gliders, wind turbine blades, turbomachinery [15]. Regarding the behavior of the LSB in respect to changes in Reynolds number and angle of attack, roughly speaking, with increases of the Reynolds number the bubble size decreases and with increases of angle of attack the bubble size decreases and moves towards the leading edge of the airfoil [15].

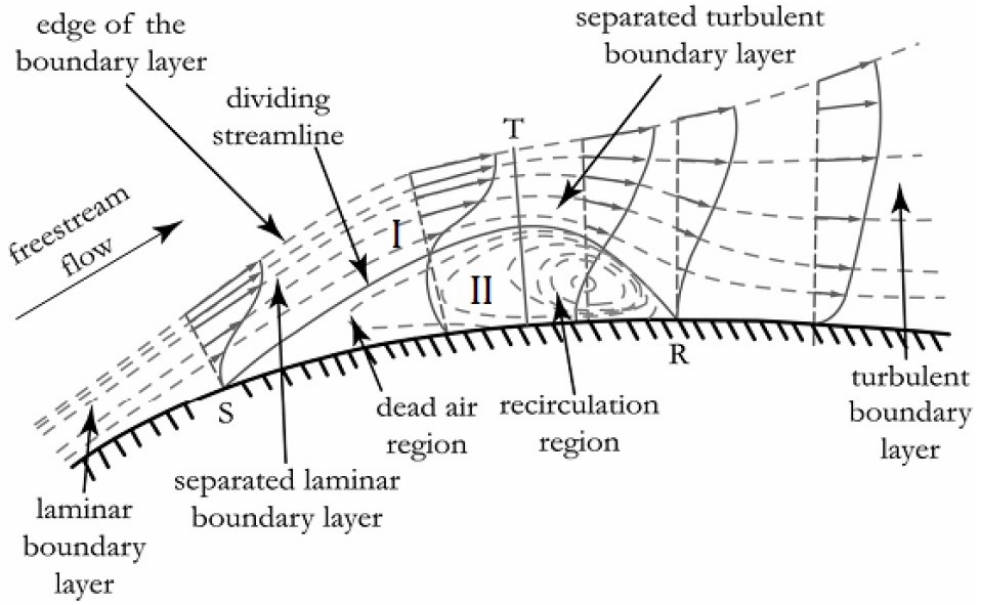

Figure 1.3: Structure of the time-averaged laminar separation bubble [16]

1.1.1. Long and Short Laminar Separation Bubbles

Two different types of laminar separation bubble can be distinguished: a ”short” bubble and a ”long” bubble. Initially Owen and Klanfer [17] classified the bubble as ”long” or ”short” depending on the ratio between total bubble length l (the distance between separation point and reattachment point) and the boundary layer displacement thickness at separation δ_s^*. According to the authors, short bubbles have an $l/\delta_s^* = O(10^2)$ and long bubbles have an $l/\delta_s^* = O(10^4)$. However, this kind of classification doesn't always lead to a clear distinction between the two types: in fact, in some cases, after bursting (for more on bursting see Section 1.1.3), a long bubble can be only a few times as long as the previous short bubble [8]. Tani [9] suggested that the two types of bubble could be distinguished based on the effect they have on the overall pressure distribution on the airfoil. A short separation bubble, which often has a length of one percent of the airfoil chord, has only a slight effect on the pressure distribution which is close to the inviscid flow solution, except for the appearance of a minute bump and for a slight reduction in the magnitude of the suction peak [8], [9]. On the other hand, a long bubble has a length of several percent of the airfoil chord and considerably modifies the pressure distribution over the whole airfoil and has the effect of destroying the pressure peak and creating a pressure plateau after separation [8], [9]. Hence, the long bubble makes

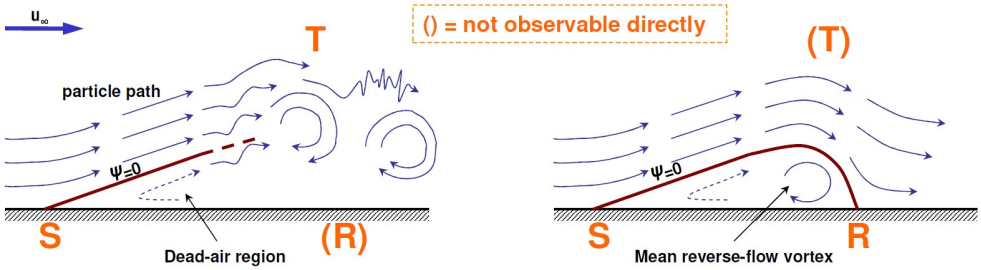

Figure 1.4: Instantaneous (left) and time-averaged (right) view of a laminar separation bubble [18]

the pressure distribution radically different from the inviscid one [9]. The two types of bubble can also be distinguished depending on the effect that changes of Reynolds number and incidence causes. Changes in Reynolds number have the same effect on both types of bubble: a decrease will cause the bubble to expand and vice versa. Increasing the incidence angle will cause a short bubble to contract (if the bursting incidence is not exceeded) and will cause a long bubble to rapidly expand. In general, long bubbles expand much more rapidly than short bubbles and long bubble flows are associated with large scale unsteadiness [8].

1.1.2. Mean Flow Behavior of Laminar Separation Bubbles

Analyzing more specifically the short bubble type, there are two conditions that are necessary for the formation of the short laminar bubble: first of all, it is needed a pressure distribution having a sufficiently large adverse pressure gradient to cause laminar separation; second of all, the conditions of the boundary layer upstream of the position of the laminar separation must be in such a way that the boundary layer will be laminar at the separation point. On top of these conditions, the surface must be smooth, the freestream must have low turbulence levels to keep the boundary layer laminar [8]. If these conditions are met than a short bubble will form. The structure of a short bubble, or more correctly of the time-averaged LSB, can be seen in Figure 1.3. The laminar boundary layer separates at the separation point S and reattaches downstream at the reattachment point R, and between the points S and R the flow is divided in two main regions: region I or the free shear layer, and region II or the recirculation bubble. The line separating these two regions is the ”mean dividing streamline” [8]. The free shear layer region is contained between the outer edge of the boundary layer and the dividing streamline, while the recirculation bubble is contained between the dividing streamline and the surface. These two main regions can be further divided by locating the transition line T. Considering the shear layer, upstream of T it is laminar and incapable of withstanding a significant pressure gradient. However, it should be noted that transition occurs over a region, and not at a specific location, and that the reattachment point oscillates, looking at the bubble in a time resolved sense [1]. Moreover, since the reattachment point position depends on transition, which in turn is very sensitive on the state of the bubble, it results that the presence of small disturbances in the flow will cause changes in the transition process which will affect the position of the reattachment point. Hence, the transition and reattachment points seen here are the mean transition and reattachment points obtained by superimposing many instantaneous captures of the bubble behavior. Between separation and transition the pressure is basically constant, and this pressure plateau is a feature of laminar separated flows [8]. After the shear layer has transitioned to turbulent, the pressure rises, thanks to the turbulent entrainment in the bubble which energizes the shear layer, and it then reattaches to the surface with a pressure value close to the inviscid one [8]. Both the pressure plateau and the subsequent pressure rise are easily identifiable on C_P plots and are a characteristic feature of laminar separation bubbles. Since the pressure rise take place in the turbulent region over the bubble, then the recirculation is mainly concentrated in the aft part of the bubble, downstream of T and it is referred as the ”reverse-flow vortex” [8], [19]. On the other hand, the region of the bubble upstream of T where the flow is almost stationary is called the ”dead-air region” [8], [19]. Changes of the Reynolds number have an effect on the dimensions of the laminar and turbulent parts of the bubble. At higher Reynolds number, the laminar part occupies most of the bubble, roughly 70% of the total bubble length [8]. Reducing the Reynolds number both the laminar and turbulent part increase, with the turbulent part increasing more. Just before bursting, the turbulent part represents more or less half of the bubble length [8].

Since the LSB is a highly dynamic and unstable phenomenon, the ”laminar separation bubble” as unique

and universal occurrence does not exist [20]. Each bubble heavily depends on the characteristics of the laminar boundary layer, on the pressure gradient and on the background turbulence level [20]. In particular, the background turbulence level can strongly affect the characteristics of the bubble, as it plays an important role in the transition process: if the initial turbulence levels are sufficiently large, the disturbances can grow to non-linear levels and lead to turbulent flow without resorting to Tollmien-Schlichting waves (the details of the transition phenomenon will be analyzed in more detail in Section 1.1.4) [21]. Thus, the image of the LSB as can be seen from Figure 1.3 only exist in a time averaged sense. At any given moment the LSB constitutes of a separated shear layer and shed vortices, as can be clearly seen in the left side of Figure 1.4. Thus, the main differences between the time averaged and instantaneous picture of the LSB are that an unsteady vortex shedding takes place instead of a steady turbulent reattachment, that there is not a definite and fixed transition point, and that the separation point is not at a fixed location [20].

1.1.3. Bursting of the Laminar Separation Bubble

After having spoken about the difference between the two types of bubbles, short and long, the focus should now be put on the mechanism behind the transition from short bubble to long bubble, also called ”bubble bursting”. Since long bubbles significantly alter the pressure distribution on an airfoil, contrary to the short bubbles, understanding the flow conditions that cause bubble bursting are particularly crucial, especially because this phenomenon is closely related to stall. During the years a wide variety of explanations of bursting have been proposed. The first explanation of bursting was proposed by von Doenhoff [22] in 1938 using a simple model which assumed that the laminar boundary layer separated tangentially from the surface and continued to follow this trajectory until laminar to turbulent transition. After having transitioned, the shear layer was assumed to follow a trajectory 15° from the previous trajectory. The reattachment point would then be determined geometrically by intersecting the direction of the shear layer with the airfoil surface. This method claimed that failure in reattachment occurs when the shear layer becomes tangential to the surface and fails to intersect the surface [8], [22]. This simple theory is able to predict qualitatively some of the bubble growth and bursting phenomena but it’s assumptions are, in general, invalid. For instance, the deflection angle after transition, has been found to vary widely from 6° to 52° [8]. Another bursting theory was proposed by Owen and Klanfer [17] in 1955. They postulated an analogy between the Reynolds number in the boundary layer at the separation point $(R_{\delta^*})_s = U_s\delta_s^*/\nu$ and the length of the bubble, where U_s is the freestream velocity outside the boundary layer, δ_s^* is the displacement thickness and are both measured at separation. This defined Reynolds number helped to define a limit above which the flow is unstable: in other words, is able to predict when the instabilities will set in and make the flow transition near the separation point (usually, a few hundred displacement thickness from the separation point). On the other hand, when $(R_{\delta^*})_s$ is below this critical value, the flow is ”less unstable” and the separated shear layer is able to remain laminar for longer distances from the separation point and, as instabilities develop, it eventually transitions to turbulent. In this second case the distance between the separation and transition point can be in the order of several thousands displacement thicknesses [8], [17]. Owen and Klanfer found out that an approximate critical value of Reynolds number is in the neighborhood of $(R_{\delta^*})_s \approx 400 - 500$: considering a specific case, if the Reynolds number exceeds this value, then the bubble will be short, otherwise it will be long [17]. In 1957 Crabtree [23] confirmed some of the hypotheses suggested by Owen and Klanfer and found out that if the boundary layer Reynolds number based on displacement thickness at separation is greater than 450, then the bubble will be short, and if this same Reynolds number is lower than 400 then a long bubble will form. For values of the aforementioned Reynolds number in the range of 400 to 450, it is unclear what kind of bubble will occur [23]. Gaster [24] conducted a comprehensive analysis of the bursting process and proposed a two-parameter criterion to predict changes in the bubble state. The two parameters he found are the momentum thickness Reynolds number at separation $(R_\theta)_s = (U_s\theta_s)/\nu$, where U_s is the freestream velocity at separation and θ_s the is the momentum thickness at separation (and not the Reynolds number depending on the displacement thickness, as previous authors have used), and the non-dimensional parameter $P_G = \theta_s^2/\nu(\Delta U/\Delta X)$, where $(\Delta U/\Delta X)$ is the velocity gradient across the bubble length, between reattachment and separation [24], [25]. With these two parameters a line can be traced in a plane having on the x-axis the separation Reynolds number and on the y-axis the P_G coefficient: this line is usually called ”Gaster’s bursting line”. Usually the line starts at $P_G = -0.09$ and a Reynolds number of around 125, which is the point where separation start to occur [8], [11], [24]. Gaster also theorized a sort of feedback mechanism between the bubble and the pressure distribution upstream of the bubble. As the freestream velocity is decreased, the perturbations on the pressure distribution caused by the bubble increase as the bubble expands, and they

increase in such a way that the boundary layer Reynolds number at separation is decreased, leading to a further increase in bubble size. This feedback loop continues until bursting occurs [8], [24]. In more recent years, Diwan et al. [26] introduced a single parameter criterion using the non-dimensional quantity $P_{DCR} = h^2/\nu(\Delta U/\Delta X)$ which comprises the maximum bubble height (h) as an influencing parameter. The authors found that bursting is likely to happen when $P_{DCR} < -28$ [25], [26]. All the aforementioned works highlight the complexity of bursting and show that this phenomenon is still not completely understood.

Qualitatively, bursting occurs when a reduction in vortex shedding occur or when strong upstream perturbations ”interrupt” the vortex shedding on the bubble altogether, thus breaking the mechanism responsible for the movement of momentum close to the wall and shear-layer reattachment [27]. Hence, with the disappearance of the reverse flow region the incoming disturbances will see a reduced growth and the shear layer will now need more space to transition and, possibly reattach, giving form to a longer bubble [27]. The reduction in the disturbances growth and the stabilization of the boundary layer is related to mean flow deformation (MFD): the mean flow in the aft part of the bubble is changed due to disturbance-induced MFD which in turn provokes a global change in the pressure distribution. The boundary layer reacts accordingly to the change in pressure and in such a way that the separation point moves downstream. Consequently the distance of the separated shear layer from the wall decreases and causes the stabilization of the laminar part of the bubble in respect to convectively amplified disturbances [19]. However, at some point the vortex shedding will start to happen again on this longer bubble, as the disturbances get amplified, bringing more and more momentum in the shear layer. As the vortex shedding grows in strength, the bubble grows until it reaches its most downstream location. At this point the mass accumulation inside the bubble caused by the spanwise vortices is not balanced by the mass discharge through vortex shedding until the vortices breakdown has moved sufficiently upstream. As this occurs, the LSB shrinks back to the unperturbed state. Also Marxen et al. [19] have noticed that the essential mechanism for reattachment is not the increases mixing associated with turbulence but rather the occurrence of large-scale mostly-two-dimensional vortical structures. The fact that mixing due to turbulence is not necessarily sufficient to cause shear layer reattachment can also be supposed by looking at turbulent separation bubbles, where the flow does not undergo a laminar to turbulent transition on the bubble [19]. The bursting of a short bubble will, hence, result in a longer bubble and, to correctly identify bursting, the features of short and long LSB needs to be clarified. Marxen et al. [19] identified in the existing literature five essential features of short laminar separation bubbles: (i) limited effect of the bubble on the flow around the bubble and on the pressure distribution; (ii) the ratio between laminar and turbulent portion of the bubble being approximately 1.6-3 (where the end of the laminar region is marked by the onset of nonlinear effects); (iii) almost stagnant flow only in the laminar portion of the shear layer and the presence of a plateau on the pressure distribution (for long bubbles the plateau extends beyond the point of shear layer transition); (iv) good agreement of disturbance amplification with linear stability theory; (v) sudden breakdown to three-dimensional small-scale turbulence. Not all short bubbles will exhibit all these features but long bubbles will not exhibit at least the first two. It needs to be precised that it is still not clear if bubble bursting is an unique phenomenon. Evidence in the literature suggest that at least two different forms might exist: one where the flow is laminar at reattachment and one where the flow is turbulent at reattachment [19].

It can be seen how bursting is an highly dynamic phenomenon which depends on the stability characteristics of the laminar separation bubble. Since the LSB topology depends on the boundary layer laminar to turbulent transition process, which is responsible for momentum entrainment and shear layer reattachment, it’s natural to expect this will be connected to bursting. Last but not least, even though laminar to turbulent transition in LSB has been studies in the past, the flow dynamics associate with bursting are still not completely clear. Thus, both a criterion to predict bursting and an accepted physical explanation for this phenomenon are currently lacking. [19]

1.1.4. Fundamentals of Boundary Layers and Free Shear Layers Transition

One of the most important fluid dynamic mechanisms behind the formation and the behavior of laminar separation bubbles is transition. In general, boundary layer transition is a very important and still somewhat obscure process concerning the passage from a laminar state to a turbulent state. The transition process consists of different stages that may occur consecutively or in parallel. The transition process is highly dependent on the conditions of the flow and differs, for instance, in boundary layers and free shear layers. Usually, in low disturbances environments this process will involve at least three stages: receptivity, linear

disturbance evolution and non-linear breakdown to turbulence. Receptivity consists in the conversion of external disturbances in boundary layer disturbances. In boundary layers and free shear layers this stage does not differs substantially [18]. The stage of linear disturbance evolution concerns the amplification of small-amplitude perturbations that can follow a modal or non-modal growth mechanism. Modal instabilities grow exponentially and are unbounded in time and space, while non-modal instabilities grow algebraically and occur for a limited time or spatial extent, being damped by viscosity [18]. Once the linearly amplified disturbances have grown to large amplitudes, the non-linear breakdown to turbulence starts, characterized by the appearance of coherent structures in the flow. Breakdown to turbulence happens when the primary flow structure reaches a sufficiently large amplitude to create a new instability, called ”secondary instability”. The secondary instability leads to the rapid disintegration of the coherent structures into small-scale vorticity. In the final stage of transition, localized instabilities can also occur. The different types of instabilities are further discussed in Section 1.1.5. Unlike for attached boundary layers, the transition stages are not necessarily serial: the coherent structures of the non-linear stage can influence the linear process that occurs upstream, thus affecting the whole process [18]. In the next paragraphs the transition process for attached boundary layers and free shear layers will be discussed.

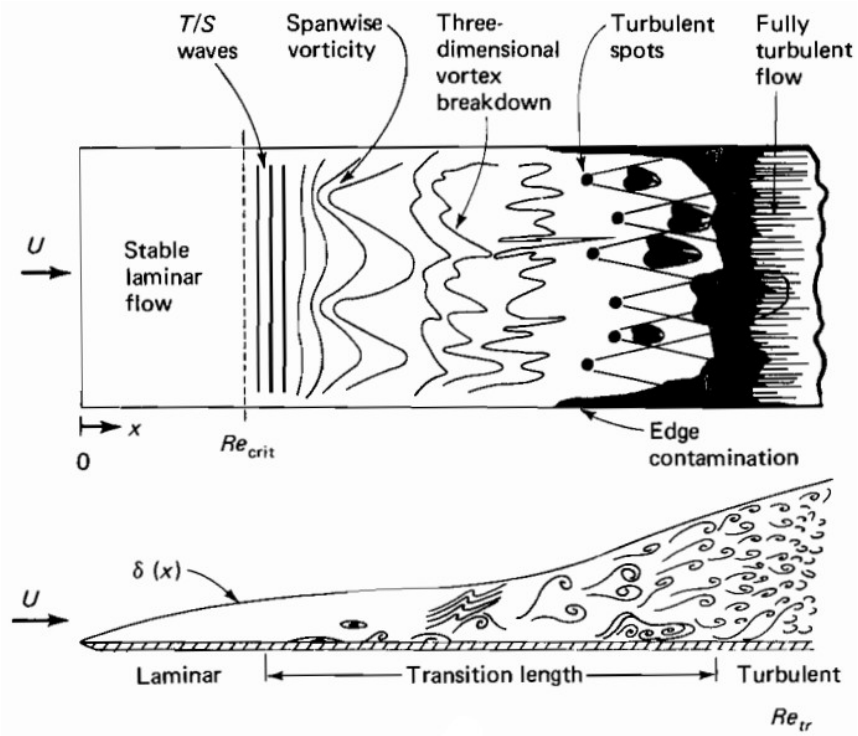

Figure 1.5: Transition process viewed from above and from the side. The Tollmien-Schlichting waves, the spanwise vorticity breakdown and the turbulent spots can be clearly seen. [28]

For what concerns attached boundary layers, above a certain Reynolds number, called ”critical Reynolds number”, the laminar boundary layer flow starts to become unstable and the small disturbances present get amplified until the flow reaches an unsteady and disorderly state called turbulence. The process of transition, as already mentioned, is complicated and yet not completely understood but, if the initial disturbance spectrum is nearly infinitesimal and random, the process sees some specific distinct phenomena. The first instabilities that can be identified are two-dimensional instabilities in the streamwise direction called ”Tollmien-Schlichting waves” (TS waves), which are the first infinitesimal indication of laminar flow instability [28]. As the flow progresses these first two-dimensional instabilities start to show spanwise variations and a tendency to become three-dimensional [28]. Tollmien-Schlichting waves can grow and develop in different ways: (i) ”in-phase Λ vortices”, having the same wavelength of the TS waves and arising at fluctuation amplitudes of $\approx 1\%$ of U_∞, and are called ”K-type vortices”. They have a spanwise wavelength of around one half of the streamwise value [28]. (ii) At lower fluctuation amplitudes of $\approx 0.3\%$ of U_∞ a

structure of staggered waves with a peak-following-valley configuration start to appear, and are called ”C-type vortices”. They have a streamwise wave number and frequency which are around half of the ones of the TS waves and a spanwise wavelength which is about 1.5 times the streamwise wavelength [28]. (iii) Finally, it exist another type of staggered vortex pattern, called ”H-type waves”, that have a streamwise wavelength of around double the TS waves wavelength and a spanwise wavelength of around 0.7 times the streamwise [28]. Then, the aforementioned three-dimensional vortices start to break down, cascading into smaller units until they become fully three-dimensional fluctuations. In this state, where there are intense local changes happening at random times and locations, ”turbulent spots” start to appear. These spots, when viewed from above, look like an arrow-head growing and moving in the flow direction: the leading edge travels at around $0.9U_\infty$ while the trailing edge at around $0.5U_\infty$ and thus they grow in size but maintaining the same shape [28]. These growing and intensely turbulent spots entrain the surrounding laminar flow. Spreading downstream they coalesce into a region where these spots continuously exist. From this point onward the flow is fully turbulent [28].

Looking at free shear layers, the process is different. While in attached boundary layers the instability amplification mechanism is viscous, in free shear layers the mechanism is mainly inviscid and relies on the velocity gradient. Free shear layers are basically parallel fluid streams with different velocities, and transition is connected to an instability happening at the interface between the fluid streams, called Kelvin-Helmholtz instability. The basic flow configuration that leads to this type of instability is shown in Figure 1.6. This instability is caused by the destabilizing effect of shear of amplifying small existing perturbations, which overcomes the stabilizing effect of stratification [29]. The source of energy required to generate this instability is drawn by the kinetic energy of the two streams [29]. The disturbances evolve to even out the gradients until they cannot grow any longer. The process forms vortical structures in the flow that enhance momentum transport and fluid mixing.

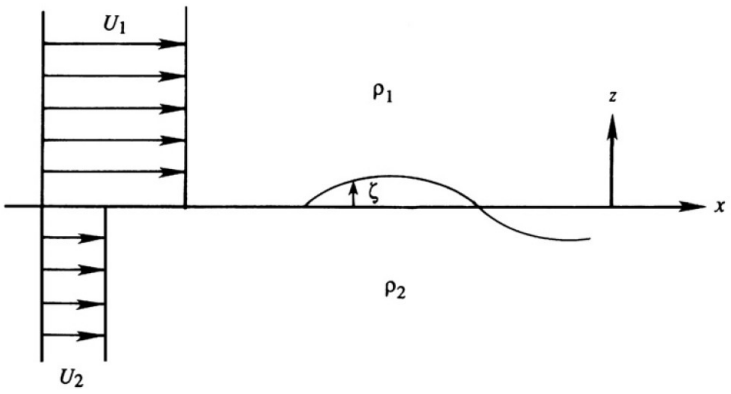

Figure 1.6: Basic flow configuration leading to the Kelvin-Helmholtz instability [29]

The two transition processes discussed above take place contextually in laminar separation bubbles. The initial disturbances present in the laminar boundary layer ahead of the bubble get amplified with viscous mechanisms typical of attached boundary layers; after the separation point, the disturbances continue to grow due to viscosity and velocity gradient, getting closer and closer to the transition process typical of free shear layers as the separated boundary layer gets further from the surface. Hence, the importance of being able to understand both transition mechanism in order to predict the behavior of laminar separation bubbles.

1.1.5. Unsteady Flow Behavior of Laminar Separation Bubbles

It can be seen how transition is a complex and poorly predictable process and different factors, for instance freestream turbulence, can significantly alter the process. In the scenario involving a laminar separation bubble the transition of the shear layer initiates with the amplification of the minuscule three-dimensional disturbances present in the freestream and that get entrained in the boundary layer. These disturbances already start to get amplified within a band of unstable frequencies in the adverse pressure gradient region well before the separation point and their growth can be approximated as linear [1], [30]. This initial stage of transition is characterized by the exponential growth of these disturbances and ends when the amplitude of the disturbances have increased such that non linear behaviors start to occur [1]. In

two-dimensional boundary layers exposed to adverse pressure gradients (as it is the case for LSB), the initial disturbances in the flow are three-dimensional but usually only the two-dimensional disturbances get amplified, forming structures similar to Tollmien-Schlichting waves. Many studies [1], [19], [31]–[33] have shown that these non-linear interactions lead to the formation of coherent structures that significantly affect the bubble characteristics. The continuous growth of these initial disturbances at some point ”saturates” and they evolve into two-dimensional spanwise vortical structures, the coherent structures mentioned above. This causes the separated shear layer to roll up into vortices that are shed at the same frequency of the most amplified disturbances [1]. The nature of the instability amplification mechanism on laminar separation bubbles is twofold: in the boundary layer the primary mechanism is viscous, or in other words viscosity is the responsible for the formation of shear; on the other hand, in the free shear layer the instability amplification mechanism is mainly inviscid and the main drive is the velocity gradient. In a laminar separation bubble these two mechanisms are combined. In fact, upstream of the separation point the instabilities are viscously driven, while after separation the mechanism start to become inviscid and connected to a Kelvin-Helmholtz instability: as the shear layer gets further from the surface the instability mechanism gets closer to a purely Kelvin-Helmholtz driven mechanism. As said before, the initially two-dimensional instabilities gets amplified up to the point at which they cannot grow more and they become spanwise vortices. These two-dimensional spanwise vortices, usually called ”rollers”, start to appear at the location where the Kelvin-Helmholtz instability wave reaches the maximum amplitude [31], [32]. The evolution of the rollers is characterized by strong unsteadiness and three-dimensionality [1]. The rollers, in the area of the transition point, start to see spanwise deformation and the formation of slight streamwise ”bulges” (when seen from above) as can be seen in Figure 1.7.

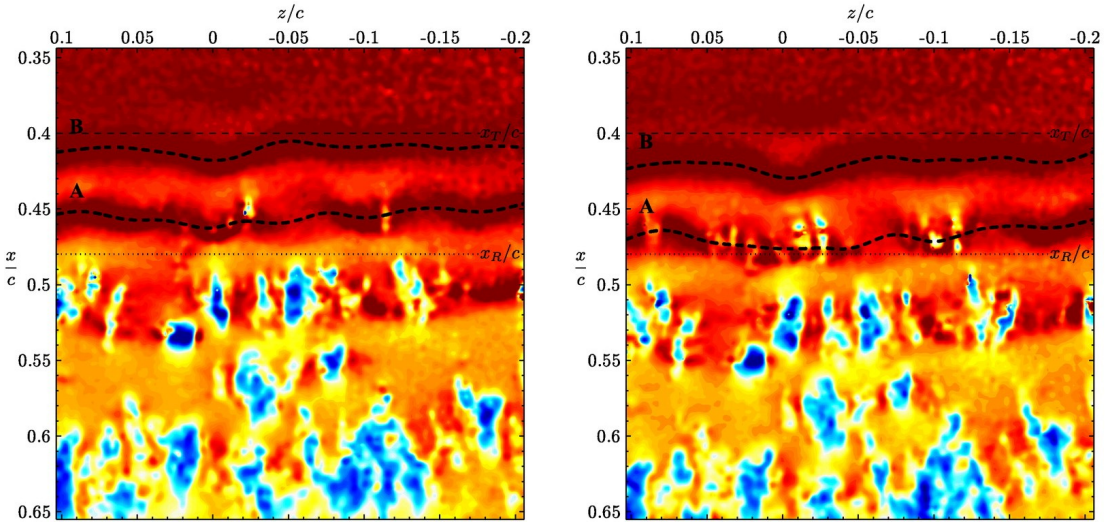

Figure 1.7: Contours of chordwise velocity over a NACA 0018 airfoil at $\alpha = 5$ deg and $Re = 100,000$. The thick dashed lines represent the spline fit to the center of two selected spanwise structures, the dashed line shows the mean transition point, and the dotted line shows the mean reattachment point. Flow direction is from top to bottom. [1]

These spanwise undulations get amplified as the rollers move downstream and start to significantly deform them, ultimately leading to vortex breakdown [1], [31]–[33]. At this stage of the vortex development, some streamwise-oriented vortex filaments connecting subsequent rollers, start to appear: these vortex filaments are called ”braids” [1], [33]. It has been suggested that secondary instabilities in the braid region are responsible for the rapid breakdown of the vortices into turbulence [1], [33]. Marxen et al. [33] classified the instability mechanisms into three main types: a primary global instability, a secondary instability and a highly localized instability. For what concerns the primary global instability of the whole bubble, a minimum amount of reverse flow is necessary (in the order of $10 - 20\%$ of the freestream velocity [27]) and it has a very low typical frequency. The spanwise length of this instability is typically in the order of size of the vortex inside the LSB [33] .The secondary instability regards the vortices shed from the bubble and it is already active in the region of vortex formation. This instability is in the order of the diameter of the shed vortices and it does not alter the topology of the whole LSB [33]. For spanwise vortices there are two

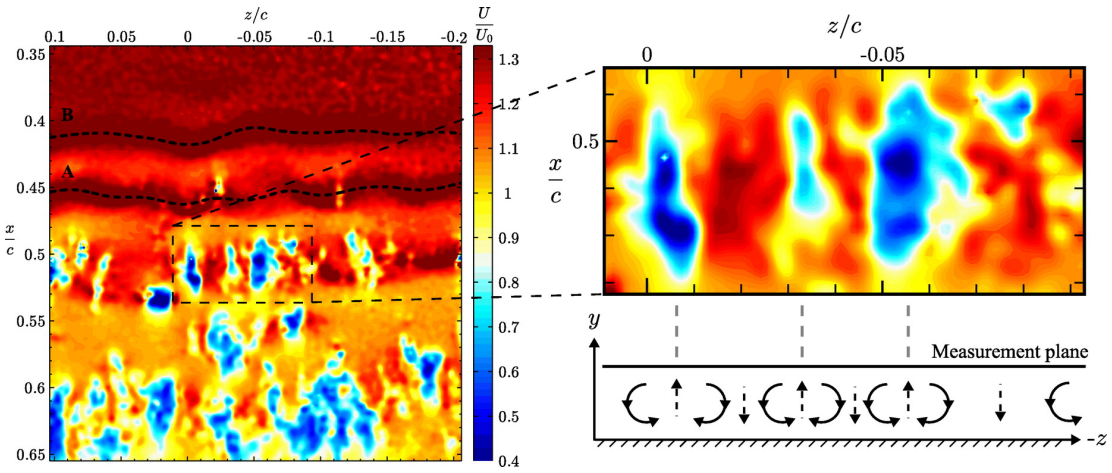

Figure 1.8: Chordwise velocity field. On the right, close up of the footprint of the streamwise vortex pairs in the x-z plane and their associated flow structure in the y-z plane. Flow direction in the z-x plane is from top to bottom. [1]

separate secondary instability mechanisms: elliptic and hyperbolic. The elliptic instability has the effect of yielding a spanwise deformation of the vortex cores while the hyperbolic instability concerns the flow between two consecutive vortices, and is responsible of the three-dimensionality of the braids [33]. The highly localized instability happens on the smallest scale and affects localized region of the shear layer [19]. It has been noted that after the formation of the rollers these vortical structures can sometimes coalesce in one structure, which is then separated from the closest downstream vortex by approximately double the wavelength that would be found between two non-merged rollers, as can be seen from Figure 1.9. However, a relatively small fraction of rollers end up coalescing and thus rollers merging is not a strongly periodic phenomenon [1]. For what concerns the convective velocity of the rollers, it has been seen that the ratio between the convective velocity and the edge velocity U_c/U_e is comprised between 0.3 and 0.5 and the rollers increase their convective velocity as they approach the mean reattachment point [1].

An interesting aspect concerns the ratio between the spanwise and chordwise wavelength of the rollers λ_z/λ_x which has been noticed to be around 2. Studies have found different values of spanwise to streamwise wavelength, such as 2.4 [19], 2.0 [1], 2.5 [31], 2.1 [32], 1,94 [34]. More specifically, Michelis et al. [32] have found that the normalized characteristic wavelengths λ_x/δ_s^* and λ_z/δ_s^* (where δ_s^* is the boundary layer displacement thickness at separation) are respectively in the order of 14.7 and 30.2. Observing this sequence of rollers development and breakup it can be noticed an overall flapping motion of the shear layer at a very low frequency, and, at the same time, low frequency excursions of the reattaching surface in the streamwise direction. In other words, the laminar separation bubble contracts and expands, mainly in its aft part [35], [36]. The overall behavior of the shear layer, and thus the flapping motion, is affected by the random incoming perturbations. However, despite the recorded presence of low frequency unsteadiness in LSB, the physical mechanism behind it remains not completely clear [36]. Malmir et al. [36] have suggested that the flapping motion of the bubble could be due to an array of spanwise alternating streaks. The passage of the streaks in the reattachment regions reduces the overall bubble size while in the absence of streaks the bubble is permitted to grow. Thus the low frequency fluctuations of flapping correspond to the time it takes for the streaks to form, amplify and pass over the LSB. Malmir et al. [36] found that the flapping occurs at a Strouhal number of around $St \approx 0.08$.

After the breakup of the rollers starting from the spanwise undulation, it seems that spanwise vorticity is reoriented in the streamwise direction, leading to the formation of pairs of counter-rotating streamwise-oriented vortices [1]. These streamwise vortices are another responsible mechanism of entrainment of high-momentum fluid toward the surface and the ejection of low-momentum fluid away from the surface [1], [37]. This mechanism can be seen in Figure 1.8 with the formation of alternating regions of high and low chordwise velocities [1]. Moreover, these streamwise vortices are responsible of the lift up from the wall of the spanwise shear layer vortices [1]. The onset of the streamwise vortices is closely connected to the reattachment of the shear layer, due to the momentum exchange that they drive and quickly results

in rapid distortion and breakup of the structures as the turbulent boundary layer develops. Thus, both the rollers and these streamwise vortices, since they manifest themselves in the reattachment area, are responsible for the reattachment process of the shear layer.

After having analyzed the behavior of the instabilities over a LSB it can be seen that the formation and evolution of the shear layer vortices and their breakdown into turbulence bear similarities with the transition process in attached boundary layer and in free shear layers. In the former, the transition process concerns the formation of TS-waves, their spanwise deformation, the formation of Λ structures and subsequently of turbulent spots that rapidly spread. In free shear layers transition is related to Kelvin-Helmholtz roller and to their spanwise deformation and breakdown which is responsible for the energy redistribution at smaller scales. Thus, it can be seen how in the later stages of transition on a laminar separation bubble these two mechanisms are combined [1]. Another important aspect which is worth to discuss in order to understand the evolution of the vortical structures is to relate the spanwise deformation of the shear layer vortices and their streamwise evolution by computing the spanwise coherence length l_z. This quantity can be helpful when assessing the noise emissions related to a LSB that forms close to the leading edge of an airfoil. In the vicinity of the mean transition point, l_z usually reaches the maximum values ($l_z/c \approx 0.12$ is a good reference value [1]), and soon after it rapidly decreases due to the spanwise deformation and breakup of the vortical structures. The minimum of spanwise coherence is reached just downstream of the mean reattachment point (with values of around $l_z/c \approx 0.01$ [1]). This also confirms the breakup of the main rollers in small-scale turbulence.

Up to this point it has been considered the case of non-zero freestream turbulence, which is representative of real scenarios. In general, in the absence of external disturbances only self-excited flow instabilities can initiate the transition process [38]. It has been assumed that this self-excited mechanism is originated by regions of absolute instability, such as a global oscillator, leading to synchronized oscillations across the LSB that eventually initiate the self-sustained shedding of spanwise vortices [38]. Subsequent secondary instabilities of the vortices would lead to three-dimensionality of the vortical structures and transition to turbulence [38]. To predict the onset of absolute instability the peak reversed flow velocity in the LSB scaled with the freestream velocity (u_{rev}) can be used. The threshold for the onset of the instability have been suggested to be $u_{rev} \approx 16 - 20\%$ [38]. Also, an approach considering global eigenmodes can be applied, leading to the identification of a three-dimensional temporally amplified eigenmode. This instability is of centrifugal nature and was found to become unstable for two-dimensional bubbles with a peak reversed flow of $u_{rev} \approx 6 - 8\%$ (substantially lower than for the global instability) [38]. This leads to the conclusion that two-dimensional separation bubbles would become three-dimensional prior to the onset of vortex shedding and that this instability would produce spanwise-periodic modulation of the bubble [38]. Numerical simulations have been performed in the case of zero freestream turbulence. One of such investigations is the one by Hosseinverdi & Fasel [37] which have run direct numerical simulations (DNS) on a flat plate. They found that after the laminar boundary layer separation and after the creation of a smooth separated shear layer there are some vortical structures confined in the inner region of the boundary layer. Downstream these vortices are lifted in the shear layer and three-dimensionality start to appear with the formation of ”legs”, counter rotating vortices, that protrude towards the wall. Proceeding even more downstream, the aforementioned legs touch the wall and start to fill out the boundary layer in the spanwise direction. These spanwise oriented structures result from the two-dimensional disturbances associated with the Kelvin-Helmholtz instability of the mean flow profile. Shortly after the shear layer undergoes transition, it is then followed by the shedding of strong coherent clockwise vortices and finally the shear layer reattaches to the surface. Near the reattachment area the large scale vortices have penetrated the boundary layer: these vortices maintain coherence in the spanwise direction at first but are then destroyed further downstream. Thus, in the case of zero freestream turbulence transition is delayed and coherent structures persist even downstream of reattachment and do not get quickly destroyed as in the case of non-zero freestream turbulence.

All this being said, it’s important to keep in mind that the investigation of laminar separation bubbles is strongly dependent on the conditions selected: pressure distribution and the type and level of perturbations present in the boundary layer upstream of the bubble will significantly affect the results.

1.1.5.1.Spectral Content of Wall Pressure Fluctuations

Since laminar separation bubbles are highly unsteady phenomena, it is worth to analyze the spectra of the wall pressure fluctuations to properly investigate their dynamic behavior.

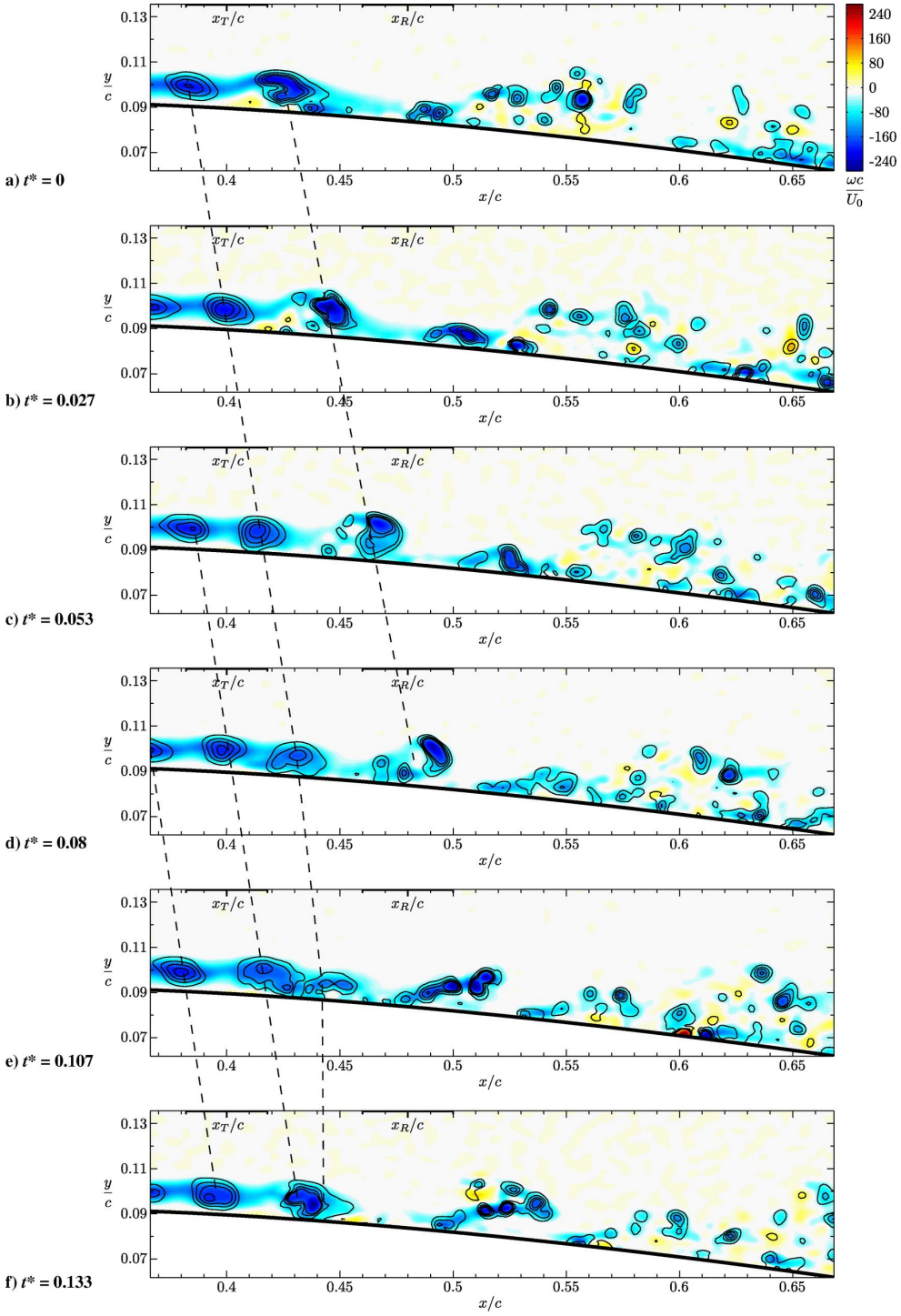

Figure 1.9: Contours of spanwise vorticity. The solid lines visualize the vortices and the dashed lines connect the same structures [1]

Far upstream, close to the leading edge of the airfoil, the frequency spectrum does not show the presence of dominant frequencies. Moving downstream towards the separation area the disturbances will start to amplify within a certain frequency band centered at a specific frequency called ”central frequency” [39]. The disturbances are amplified in the shear layer and further growth of disturbances results in fluctuations of higher amplitude and lower periodicity [40]. Further downstream the energy content broadens across a wider range of frequencies denoting laminar to turbulent transition and the breakdown of the spanwise

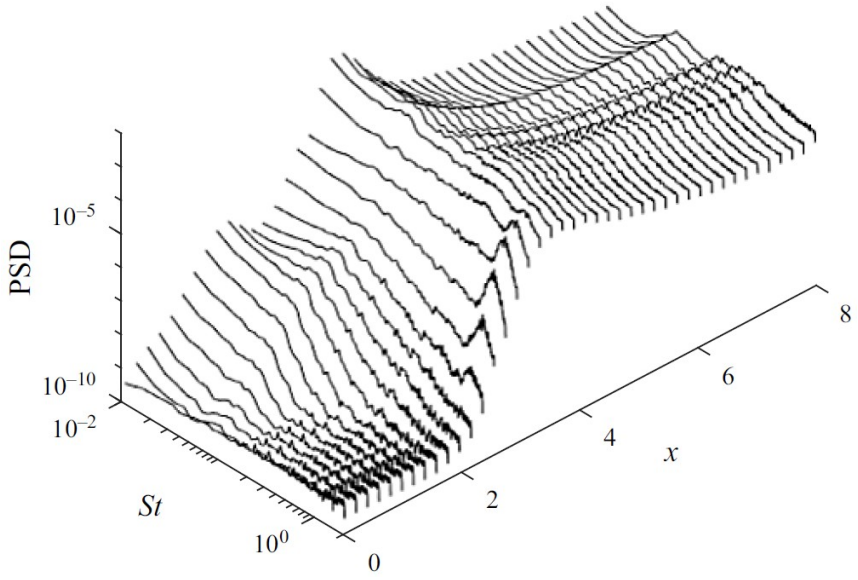

Figure 1.10: Power spectral density of wall pressure fluctuations. Mean separation point $\bar{x_s} = 1.76$, mean reattachment point $\bar{x_r} = 3.80$ [36]

vortical structures created by the shear layer roll up [36], [39], [41]. Beyond this point only a weak signature of fluctuations appear within the unstable frequency band, thus signaling the presence of turbulence flow [1], [39]. Considering the lower end of the frequency spectra, it can be seen that disturbances will start to amplify around the separation location, suggesting that low frequency upstream disturbances exist ahead of separation and are selectively amplified by the adverse pressure gradient and by the bubble itself [36]. Malmir et al. [36] investigated the dynamic phenomena on a LSB on a flat plate using DNS. Their work shows the presence of a peak centered at a Strouhal number of $St \approx 0.08$ in the separation area and that continues to grow up to the reattachment area, persisting also far downstream. They linked the persistence of this low frequency with the advection of coherent structures downstream. Malmir et al. [36] also noticed the presence of a higher frequency peak centered at $St \approx 1.52$ that begins to emerge and amplify between the separation and reattachment areas and that can be linked to vortex shedding. This peak rapidly decays in the reattachment area, unlike the low frequency peak, due to the rapid breakdown of the spanwise vortical structures in that area. Both peaks on the frequency spectrum can be seen in Figure 1.10. On average the vortex shedding frequency matches the central frequency of the unstable frequency band, hence, in the case of natural, uncontrolled transition, the central frequency of the band gives the most probably time scale for shedding: however, the shedding varies from cycle to cycle in a probabilistic way within the bounds of the unstable frequency band [39]. It has been seen that the shedding frequency increases linearly with increases in angle of attack due to the shrinking of the bubble [39]. Figure 1.11, from the work of Kurelek et al. [1], shows a similar image to the one depicted above: the presence of a low frequency peak that persist far downstream, the presence, already before the mean transition point ($x_t/c = 0.40$), of a peak centered around the central frequency of the unstable band, and the broadening of the unstable band after the mean reattachment point ($x_r/c = 0.48$) can all be seen in the image.

The one discussed above is a general case of the spectral content of a LSB with natural, uncontrolled transition. Each case will show differences depending on the test conditions.

1.1.6. Measuring Techniques of Laminar Separation Bubbles

Looking at the existing literature on experimental studies of laminar separation bubbles (for instance on the Scopus database) the vast majority of the researches employed particle image velocimetry (PIV) to characterize mean and instantaneous behavior of LSB. PIV can be a powerful tool because it allows the visualization of the flow velocity vector, is useful to study the velocity fluctuations and the vortex dynamics, and, at the same time, it gives the possibility to study the mean flow behavior by superimposing multiple instantaneous measurements. Despite being a powerful technique, PIV also have some disadvantages, most notably regarding the setup: the PIV setup is complex, requiring optical access to the test section,

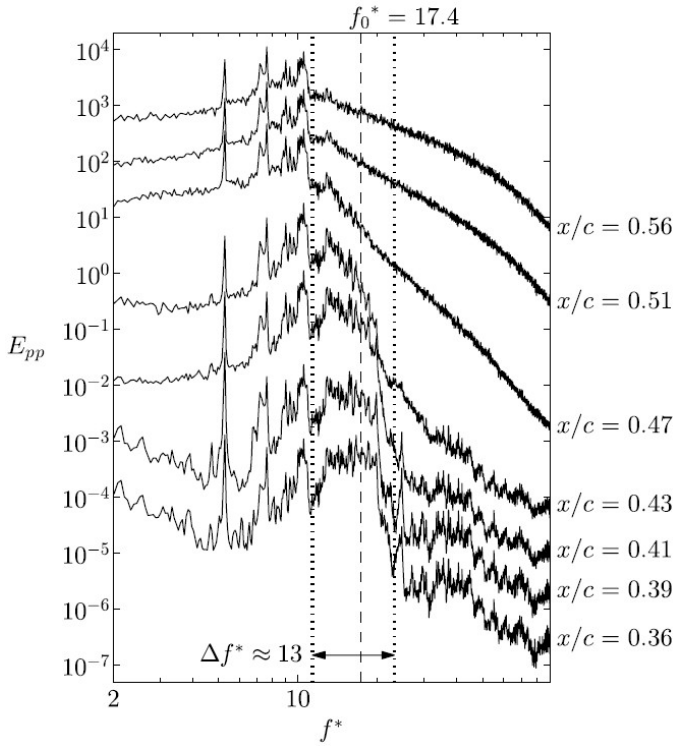

Figure 1.11: Spectra of wall pressure fluctuations. Each spectrum is stepped by an order of magnitude for clarity. Non dimensional frequency $f^* = f/U_\infty$, central disturbance frequency f_0^*. [1]

powerful lasers, optical lenses, cameras, and a way to introduce seeding in the test section, not to mention the inherent difficulty of obtaining reliable measurements close to the surface. Apart from the challenges related to the set up of the experiment and the cost of the equipment, it needs to be bore in mind that the use of high power lasers and seeding can pose hazards and contaminate or damage the test facility.

Another velocity-related measuring technique is hot wire anemometry. Hot wire anemometry (HWA) can be extremely useful when the velocity magnitude and fluctuations needs to be measured in specific regions of the flow, with high accuracy and frequency resolution. Moreover, it can prove useful when performing measurements along the normal direction to the surface inside the LSB. Albeit small, however, hot wires are more intrusive than other techniques and their use becomes less justified as the number of measurement locations increases, or when the evolution of a flow structure must be monitored in both time and space. In such cases, surface hot-wire anemometry can be advantageous, as it allows simultaneous recording from multiple hot wires distributed over a surface. In general, the main drawback of single-wire hot-wire anemometry in the study of laminar separation bubbles is its inability to resolve flow direction, as well as the fact that it can only measure the velocity component perpendicular to the wire. As a result, identifying flow recirculation within the bubble can be particularly challenging, since the reversing motion and multidirectional nature of the flow are not adequately captured by hot-wire anemometry. Multi-wire probes can be used to assess the flow directionality.

The second most common experimental technique when measuring laminar separation bubbles is related to wall pressure measurements. When only the mean flow behavior of the bubble is investigated, wall taps to measure the static pressure are sufficient. They provide information about the mean dimension and location of the bubble by looking at a pressure coefficient plot. However, being the LSB highly unsteady phenomena, this technique only provides little information and measuring techniques capable of capturing wall pressure fluctuations need to be used. In this case flush mounted or cavity mounted microphones are the most common measuring device. Depending on the working principle, on the head size and on the mounting type, microphones can provide excellent dynamic response and can resolve the pressure fluctuations associated to small scale vortices. Usually, measuring the wall pressure is a much easier experimental task than measuring the flow velocity with PIV but it also comes with some disadvantages and

challenges. Most notably, since the microphones needs to be installed inside the model, the challenges concern the drilling of the taps on the model surface and the placement of the devices and electrical wiring inside the model. This can prove complicated, if not impossible, in areas such as the trailing edge of airfoils.

Among wall pressure measuring techniques, a promising device is represented by piezoelectric foils or ”piezofoils” which work by relating the electric charge accumulating on its surface to the pressure applied. Their characteristics and working principles will be explained in detail in Section 1.2.3 Their use in laminar separation bubbles is still relatively unexplored, especially in subsonic flows but they promise to solve some of the challenges associated to particle image velocimetry and microphones. Most notably piezofoils require minimum space inside the model (just the space for some electrical wires and small circuitry) as the foil itself is glued on the external surface of the model, greatly reducing set up complexity and enabling measures in areas of the model with low internal volume. Its low thickness and flexibility allows to closely follow the surface shape and to avoid interferences with the flow. Moreover, if properly designed and shielded against electromagnetic interference, its spatial resolution and dynamic response can be comparable to that of microphones. Last but not least, cost is orders of magnitude lower than PIV or microphones, techniques that require investments in the order of tens of thousand of euros, when measuring and investigating the same phenomena in a similar experimental setup.

Hence, a measuring technique capable of measuring wall pressure fluctuations over a wide area at low cost and low set up complexity is currently lacking. This uncovered experimental segment could be filled in with the use of piezofoils. Since LSB are phenomena taking place over large areas with different streamwise and spanwise unsteady pressure imprints and whose investigation would benefit of a technique capable of assessing the pressure imprint over a larger area, the piezofoil seems a promising candidate for such studies.

1.2. Unsteady Pressure Measuring Devices

In order to have a a complete understanding of the fluid flow under consideration, fundamental quantities, such as pressure, temperature, density, flow velocity vectors, must be measured or computed. In an experimental setup, a direct measurement of density is very often impossible and the velocity can be easily determined from measures of total and static pressure (even though flow velocity can be measured in many other ways, such as hot wire anemometry and particle image velocimetry). Therefore, experimentally, it's quite common to only measure temperature and pressure to retrieve all the other quantities [42]. Hence the reason why many different types of pressure measuring devices exist. Since laminar separation bubbles are an highly dynamic and unsteady phenomena, to analyze the flow behavior the pressure trend over time needs to be recorded. Different devices can be used to measure the pressure fluctuations happening over time: the present chapter will give an overview of such devices, their functioning and their characteristics.

1.2.1. Pressure Transducers

Pressure transducers are devices that provide and electrical response to a pressure or changes in pressure. Many different types of pressure transducers exist based on the principle they use to measure pressure. Pressure transducers are often miniaturized, in order to be placed within the model to be tested and can measure both steady and unsteady pressure and are the most used pressure measuring device in experimental facilities. Pressure transducers require an initial calibration and frequent calibration checks to maintain the required accuracy [43]. The devices that only measure the fluctuating part of pressure are called "microphones" [42]. Thus, in this chapter, the different types of microphones will be analyzed.

There are several categories of microphones, for instance: piezoelectric, capacitive, resistive. Piezoelectric transducers take advantage of the piezoelectric properties of certain materials to generate an electric potential difference between two surfaces when subjected to a force (more on piezoelectricity will be explained in Section 1.2.3). Piezoelectric transducers don't have a response to zero frequency, hence they cannot measure stationary or slowly varying pressures. Roughly they have a pressure range going from 10^2 Pa to 10^9 Pa and a maximum frequency response of around 300 kHz [44], [45]. Piezoresistive transducers utilize semiconductors, such as silicon crystals, that show a change in resistivity when deflected (similarly to strain gauges). The silicon crystal is at the same time the element that deforms and the transducer [44]. They can have different dimensions and a frequency range that can arrive to several kHz [44]. The transducers produced by the brand "Kulite" mostly use this technology. Their sensors are composed by three layers of different silicon types: the first layer is the pressure sensitive diaphragm which deforms under pressure, the second layer provides dielectric isolation and the third layer contains four silicon strain gauges patterned in a Wheatstone bridge configuration that sense the change in resistivity when the silicon deforms [46]. A common Kulite transducer of this type is the XCQ-093-10D which has a pressure range from 0 to 700 kPa and a frequency range that goes from 0 to around 20 kHz [47], [48]. Capacitive transducers, also called "condenser microphones", are the most used measuring device for dynamic pressure measurements. They work by measuring the change in capacitance in a small air gap between two electrically charged metallic surfaces. One of the two surfaces is rigid and the other one flexible and is subjected to the pressure fluctuations [42]. Capacitive transducers cannot measure steady pressure. They have a wide frequency response ranging from a few hertz to 100 kHz, a large dynamic range capability, and they are quite rugged [43], [49]. A common condenser microphone is the Brüel & Kjær type 4180: it has a frequency range from around 2 Hz to 20 kHz and a dynamic range going from around 224 μPa to 2 kPa (corresponding to a range going from 21 to 160 dB) [50].

1.2.2. Pressure Sensitive Paint

Pressure sensitive paint (PSP) is an optical method through which surface pressure can be related to the local oxygen concentration in the air. Pressure sensitive paint consists of a luminescent dye and an oxygen permeable binder. When the paint is excited by light radiation three different effects can take place: a part of the incoming light is re-emitted with a different wavelength (fluorescence or radiation), part of the incoming light is transformed into internal energy (internal conversion), and part of the incoming energy excites oxygen molecules (oxygen quenching) [44]. This last mechanism is the one mainly responsible for the basic functioning of this measuring technique: in fact, when oxygen quenching happens no photons are emitted. It can be easily seen that in presence of higher amounts of oxygen molecules, and thus at a higher pressure, luminescence is reduced: in other words, the higher the oxygen partial pressure, the less the paint glows [51]. Hence, the pressure distribution on the surface can be traced by looking at how the

intensity of the light emitted changes [44], [51]. Pressure sensitive paints present many advantages: they allow the continuous measurement of pressure on the whole surface; their intrusiveness is minimal, the time and cost to prepare the model is lower in respect to other pressure measuring techniques (where orifices needs to be drilled and transducers inserted into the model) [51]; they provide high resolution data, only limited by the resolution of the acquisition system [44]. The PSP response time is directly proportional to the square of the paint thickness on the surface and inversely proportional to the diffusion coefficient of the binder, and in general, is quite low, in the order of 20 Hz [51]. The usual pressure range of PSP goes from 0 to around 200 kPa [52]. More recently, the so called ”fast PSP” have been able to achieve frequency response in the order of the kHz by creating a porous binder to facilitate oxygen diffusion and enable faster interaction between the oxygen and the excited luminescent molecules [53]. Another characteristic of PSP is the requirement of a precise calibration procedure. Calibration is done in order to retrieve the necessary constants to relate the luminescence intensity with the pressure [49]. Two different types of calibration are usually employed: in a calibration chamber where paint samples are tested at carefully controlled values of pressure and temperature and in situ calibration using conventional pressure taps, to provide known pressures, and thermocouples for temperature readings applied directly on the model [49]. Usually, after the in situ calibration procedure the paint is used right away (often the model is directly sprayed in the test section to reduce installation time) because PSP is sensitive to aging: this means that the paint changes its properties with time, because the environment around the individual molecules changes with time, leaving some luminous molecules that are unable to be quenched [51]. This introduces an offset in the luminous signal and an error in the results. Moreover, the paint employed in the in situ calibration is the same paint that is being used: this makes sure that impurities in the paint, different paint compositions or unevenness in the paint thickness can affect the results [49].

1.2.3. Pressure Sensitive Foils

Pressure sensitive foils are rather new measuring devices that utilize piezoelectric polymers and which allow the measure of pressure fluctuations by converting the voltage that accumulates over them to a pressure reading through a calibration curve. The present chapter will touch on the basic principles behind piezoelectricity, analyzing the working principles behind the piezoelectric polymers and their applications, before focusing on the specific device that will be used during this work: the piezofoil.

1.2.3.1.Piezoelectric Materials

Piezoelectric materials have been known since 1880, year in which the Curie brothers discovered piezoelectricity while working on crystals [54]. The word ”piezoelectric” comes from Greek, where ”piezo” means ”pressure”, and thus ”piezoelectricity” means ”pressure electricity”, in other words, ”electricity that results from pressure”. In piezoelectric materials, applying mechanical stress makes electrical charges appear on the material, and thus a voltage which is proportional to the applied load. This effect is called ”piezoelectric effect” or ”direct piezoelectric effect” [54]–[56]. However, in piezoelectric materials, the opposite is also true: when an electric field is applied to the material, mechanical strain will be generated according to the polarity of the applied electric field and proportional to its strength. This effect is called ”inverse piezoelectric effect” and was experimentally confirmed by the Curie brothers in 1881 [55], [56]. The direct and inverse piezoelectric effects are schematized in Figure 1.12. Piezoelectric research already saw some impulse with the discovery of ferroelectricity of the Rochelle salt in 1920 [55], [57]. Ferroelectric materials have a spontaneous polarization, even when there is no applied external electric field, and their polarization can be reversed by the application of an electric field [57]. Piezoelectricity and ferroelectricity are closely related properties of a material: piezoelectric materials are ferroelectric materials in which the ferroelectric behavior does not appear above a certain temperature. Below this temperature a ferroelectric transition takes place and thus the ferroelectric state is at the same time a piezoelectric state [57].

Research on ferroelectric and piezoelectric materials really gained momentum with the discovery of barium titanate ($BaTiO_3$) in 1945, material that has a perovskite structure with which confer it outstanding ferroelectric properties [55], [57]. Thus piezoelectric materials with a perovskite structure represent the best candidates for a wide range of applications that will be discussed in a subsequent chapter [55].

Piezoelectric materials can be categorized as natural or manmade: materials like quartz, topaz, Rochelle salt, tourmaline have natural piezoelectric properties and thus are categorized as natural; on the other hand, ceramics like barium titanate ($BaTiO_3$), lithium niobate ($LiNbO_3$), potassium niobate ($KNbO_3$) or polymers like polyvinylidene fluoride (PVDF) are categorized as manmade.

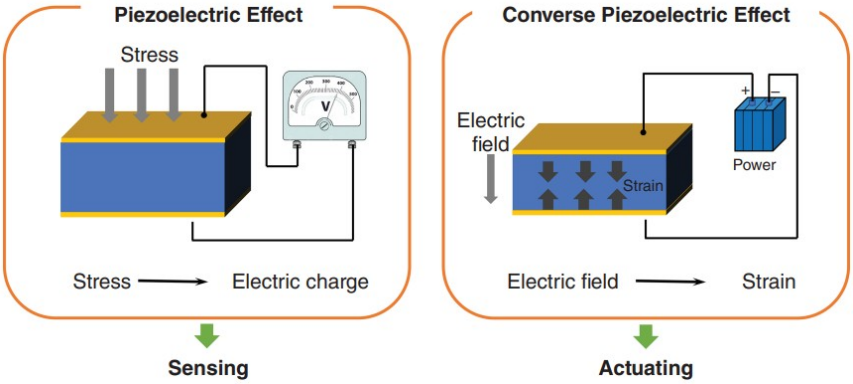

Figure 1.12: Direct and inverse piezoelectric effect [58]

1.2.3.2.Working Principles of Piezoelectric Polymers

As already introduced in Section 1.2.3.1 piezoelectric materials are able to develop an electric charge proportional to the mechanical stress applied and, vice versa, are able to deform when an external voltage is applied. This behavior holds for all sort of piezoelectric materials, including the piezoelectric polymers. Among these, the most common and used is polyvinylidene fluoride (PVDF) which is made from a non-reactive thermoplastic fluoropolymer, having a semicrystalline structure consisting of long-chain molecules [54]. The molecules constituting PVDF are carbon, which constitutes the molecule's backbone, fluorine, which is electronegative, and hydrogen, electropositive. Fluorine and hydrogen form dipoles in the molecule and thus, each chain possesses a dipole moment perpendicular to the polymer chain [54], [59]. If the long molecular chains crystallize in parallel rows, and in the ferroelectric state, then the dipoles present in the chains will align along a crystalline axis leading to a macroscopic polarization, as can be seen from Figure 1.13 [54].

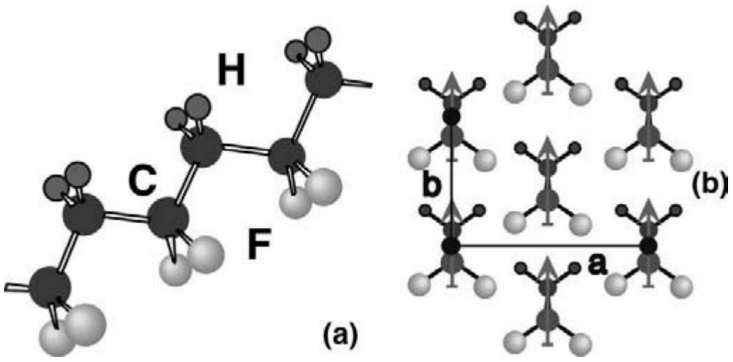

Figure 1.13: PVDF molecular structure, showing the alignment of the dipoles [60]

The crystalline phase of PVDF present five crystal polymorphs: phase I or $\beta - phase$, phase II or $\alpha - phase$, phase III or $\gamma - phase$, δ, ϵ, which depend on the crystallization conditions. $\beta-$, $\alpha-$ and $\gamma - phases$ are the most frequent crystalline polymorphs of PVDF [61]. $\alpha-$ and $\beta - phases$ are the most interesting due to their unique properties. The $\alpha - phase$ has a molecular chain with fluorine and hydrogen atoms alternating on each side of the chain and is the most thermodynamically stable phase but it's non-polar due to the antiparallel packing of the dipoles within the unit cell; the $\beta - phase$, on the other hand, shows the highest dipolar moment per unit cell and thus has the highest piezoelectric coefficient. Hence, when piezoelectricity is the wanted property, the $\beta - phase$ should be promoted as much as possible in the material [54], [61].

Another important consideration related to piezoelectricity concerns the symmetry of the crystal structure. Fundamentally, piezoelectricity arises due to the displacement of atoms within non-centrosymmetric unit cells, and in it quite easy to imagine in case of materials with a regular crystal structure like ceramics. However, polymers consist of long molecules and have areas where the polymer chain can form small crystal

structures which are surrounded by the amorphous matrix of the remaining polymer chains and thus, it's not immediately clear if the same model of piezoelectricity can be applied [62]. Nonetheless, the requirement of non-centrosymmetry still holds to piezoelectric polymers and can be explained with Neumann's principle: the principle states that the symmetry of a material must be represented by the symmetry of its properties, and the statement is true for all material properties including the piezoelectric properties [62]. This principle leads to the conclusion that a centrosymmetric material cannot be piezoelectric or, in other words, that overall the material cannot contain a center of symmetry if it is piezoelectric [62]. When the polymer crystallizes, multiple crystalline region will appear, exhibiting a random orientation distribution. Similarly as the random distribution of polymer chains which is isotropic, the random distribution of crystal structure is also isotropic and thus it will have a center of symmetry. To remove the center of symmetry, it's necessary to generate some anisotropy in the material and different processing methods are available. One common method concerns the stretching of the polymer to several times its original length and it's called drawing. During the stretching the polymer chains align with the drawing direction and this also aligns the crystalline regions in the amorphous matrix, yielding a polymer which is radially symmetric about the drawing axis [62]. The drawing of the polymer results in a strain-induced phase transition to the $\beta - phase$, which is known to enhance piezoelectricity [62]. Some copolymers spontaneously crystallize to the $\beta - phase$, and thus, in theory, they would not require drawing: however, in many cases it's performed anyway in order to enhance the $\beta - phase$ content and increase piezoelectricity [62]. Another method to introduce anisotropy is electrical poling, process in which a large electric field (300 kV/cm [63]) is applied to align the dipoles in the structure of the material [62]. Poling is only possible in ferroelectric materials, that is materials which have a residual polarization that can be switched using an electric field. Polycrystalline ferroelectric materials are usually isotropic, hence without piezoelectric properties, and thus poling is required to align the dipole moments in the material, removing the center of symmetry and enabling piezoelectricity [62]. Usually, drawing and poling are both used, and their combination, coupled with the inherent symmetry elements of the polymer will be determining of the final symmetry of the sample [62].

Knowing that the piezoelectric properties come from the type of crystal structure present in the material, the piezoelectric effects can be analyzed.

$$D_k = d_{kij} T_{ij} \tag{1.1}$$

$$S_{ij} = d^*_{kij} E_k \tag{1.2}$$

Equation 1.1 and Equation 1.2 show respectively the direct and inverse piezoelectric effects, where D_k is the electric displacement, E_k is the electric field component, S_{ij} is the strain component, T_{ij} is the stress component, d_{kij} or d^*_{kij} are respectively the piezoelectric charge constant and the piezoelectric strain constant; both of them are called piezoelectric constant or coefficient but they have different units. d is a third rank tensor coupling the first rank tensor (vector) which is an electric displacement or an electric field, and the second rank tensor which is a stress or a strain [58]. Usually the subscripts of the piezoelectric coefficients are expressed with the reduced Voigt matrix notation d_{km}, where k denotes the component of electric displacement D or field E in the Cartesian reference frame (x_1, x_2, x_3), and the index $m = 1, ..., 6$ defines to mechanical stress or strain: $m = 1, 2, 3$ correspond to normal stresses (or normal modes) along the axes x_1, x_2, x_3 and $m = 4, 5, 6$ stand for the shear stresses (or shear modes) T_{23}, T_{13}, T_{12} [58], [62].

Having said all this, it needs to be acknowledged that not all polymers are piezoelectric and an universal theory describing piezoelectricity in polymers does not exist at the moment. This is likely due to the fact that the piezoelectric mechanisms in different polymers are somewhat different [62]. As already discussed, at a fundamental level the effect arises due to electrical charges within the material and thus, a certain degree of polarity in the molecule must be necessary, probably related to electronegative elements like fluorine or oxygen. However, numerous polymers exist that contain fluorine or oxygen and that can be manipulated to generate the correct symmetry but that still do not show piezoelectric properties. Hence, the phenomena is likely related to determining how the charges are coupled through the polymer chain and polymer structure to the external mechanical or electric stimulus [62]. Nevertheless this would require a titanic effort due to the incredibly intricacies and complexity of polymer systems.

1.2.3.3.Piezoelectric Polymers

As seen in Section 1.2.3.1, piezoceramic materials are some of the best piezoelectric materials, however, the piezoelectric behavior is a common property of many polymers, such as fluoropolymers, polyureas, polyamides, polypeptides, polyesters, and others [62]. Also a wide variety of biopolymers, notably collagen, cellulose, silk, also have piezoelectric properties, and the extensive presence of piezoelectric properties in biological materials made researchers think that piezoelectricity was a fundamental aspect of many biological processes [62]. Polymers with piezoelectric properties have notable advantages over the ceramic ones due to their flexibility and toughness which make them suitable for applications where bending and twisting is required [54]. Thankfully, as already stated, piezoelectricity is not restricted to ceramic materials and it is also observed in some polymeric materials, with polyvinylidene fluoride (PVDF) the first being discovered in 1969 [62], [64]. PVDF can also be modified at molecular level to form to so called ”copolymers”, adding different molecules like chlorine (for instance to form P(VDF-HFP)) or just modyfing the molecular structure increasing the number of atoms of fluorine (as in the case of P(VDF-TrFE)) [59]. Specifically, P(VDF-TrFE) or Poly(vinylidene fluoride-Trifluoroethylene) is a well known and interesting copolymer which, contrary to PVDF, presents a naturally higher ratio of $\beta - phase$ in its crystal structure, which contributes to increase the piezoelectricity of the material (the $\beta - phase$ is always present also in PVDF but in lower concentrations) [59]. Other interesting piezoelectric polymers are odd-numbered Nylons and poly-L-lactic acid (PLLA).

Albeit the above mentioned polymers all show piezoelectric behavior, they show different characteristics. For example P(VDF-TrFE) and odd-numbered Nylon have both normal and shear modes of piezoelectricity, PLLA only shows shear modes [62]. Moreover, P(VDF-TrFE) and odd-numbered Nylon need poling before being able to show piezoelectric effects, while PLLA does not require poling. These differences can be explained by considering the symmetry of each polymer: the PLLA molecule has a helical structure and thus, simply aligning the polymer chains is enough to remove a possible center of symmetry that might be present. On the other hand, P(VDF-TrFE) and odd-numbered Nylon possess a planar conformation of the polymer chain and thus, aligning them is not sufficient to allow piezoelectricity [62]. Instead the process to remove the center of symmetry is poling. This process is only possible if the material exhibit ferroelectric behavior, making possible to manipulate the polarization of the material through the application of a suitable electric field. The symmetry that is then obtained allows P(VDF-TrFE) and odd-numbered Nylon to have both normal and shear piezoelectric coefficients [62]. Table 1.1 gives an idea of the actual draw ratios D_R, temperatures T, electric field strengths for poling E and piezoelectric coefficient d. The draw ratio D_R is the ratio of the final to the initial length of the polymer.

$\boldsymbol{PolymerName}$	$\boldsymbol{D_R}[-]$	$\boldsymbol{T}[°\boldsymbol{C}]$	$\boldsymbol{E}[\boldsymbol{V/\mu m}]$	$\boldsymbol{d}[\boldsymbol{pC/N}]$
P(VDF-TrFE)	7	150	200	30
Odd-numbered Nylon	4	170	300	3
PLLA	4	80	-	10

Table 1.1: Drawing ratio, drawing temperature, poling electric field strength and piezoelectric coefficient for three commonly used piezoelectric polymers P(VDF-TrFE), Odd-numbered Nylon, PLLA [62]

1.2.3.4.Applications of Piezoelectric Polymers

Piezoelectric polymers (and piezoelectric materials in general) find countless applications especially in sensing and actuation devices, and more specifically for medical instrumentation, robotics, ultrasonic, underwater, biomedics, energy harvesting, etc. This wide variety of applications is closely connected to their advantages, such as low weight, high flexibility, high sensitivity and bio-compatibility [65].

One promising applications of piezoelectric polymers is as energy harvesting devices. This is due to the fact that under an external force, the piezoelectrical material deforms and generate a voltage, thus converting mechanical energy into electrical energy [65]. An interesting application concerns the creation of a cloth made with PVDF nanofibers which can harvest mechanical energy from human motion, such as finger tapping, arm movement or footsteps, in order to increase the lifetime of batteries [65], [66]. A similar device was developed by Mokhtari et al. [67] from a piezofiber obtained using barium titanate nanoparticle and PVDF and that could be used for the production of smart textiles able to harvest energy from the human motion. Another application concerns a self-charging pacemaker based on PVDF piezoelectric film

which converts the energy of the heartbeat in electricity to charge the peacemaker battery. This would create an effective energy source that would eliminate the need of surgery to change the pacemaker battery [68]. Taylor et al. [69] developed the ”Energy Harvesting Eel” (Eel) which uses the piezoelectric polymer PVDF to convert the mechanical flow energy in rivers and oceans to electrical power by making use of the trailing vortices developing behind a bluff body to strain the piezoelectric elements. Internal batteries are used to store the energy and the Eel has the capacity of generating from milli-Watts to many Watts depending on system size and flow conditions. A similar application, but using air as working fluid, is the one developed by Asghari and Dardel [70] which designed an energy harvester consisting of a beam with piezoelectric layers on both sides which gets excited by the flow vortices detaching from a cylinder which is positioned in front of the beam.

Another common application, also related to the energy harvesting, are the physical sensors. The flexible and wearable pressure sensor used in sensing applications are made of piezoelectric polymers like PVDF. Often, the polymer is turned into a nanofiber membrane or nanostructures [65]. A very common application concerns touch pads, for instance in mobile devices, field where PVDF is extensively used. Due to the accuracy of the piezoelectric based transduction mechanism, to faster fabrication processes and low material waste, they gained traction over optical, capacitive and resistive transduction mechanisms [55]. Lee et al. [71] developed a very thin film fabricated from PVDF and ZnO nanostructures with graphene electrodes able to simultaneously measure pressure and temperature measuring changes in pressure as small as 10 Pa.

Last but not least, a promising sector for the application of piezoelectric polymers is biomedics. Already in the past decades, implantable medical electronics have been used to enhance the quality of human life and have been used in many human body parts such as cochlear implants, cardioverter defibrillators, artificial retinas, cardiac pacemakers, etc [55]. The bio-compatibility and environmental friendliness of some piezoelectric polymers, make them perfect candidates for the next generation of medical implantable [55]. For instance, the self-curing polymer polymethyl-methacrylate (PMMA) is widely used for biological bone repair [55].

1.2.3.5.Piezofoil

PVDF can be extruded into very thin foils, reaching thicknesses of 9 micrometers, making possible the design of systems characterized by low intrusion and by great flexibility, in order to adapt to the required shape. The PVDF foil can be coated with a metal material acting as the collector for the charges that are generated on the polymer’s faces due to the applied load [63], [72]. By choosing a specific pattern of the metal coating it’s possible to create specific sensing areas which will collect the charges generated by the piezoelectric layer and will transfer the resulting voltage to the circuitry, which comprises an amplifier, and the acquisition board [63], [72]. The aforementioned device is usually referred to ”piezofoil”. Moreover, the piezofoil is characterized by great mechanical strength and the possibility of operating it in a wide range of temperatures: the maximum range lies between -40 and 150 degrees Celsius, as at 150 degrees the PVDF starts to melt, but already at lower temperatures the piezoelectric effect starts to decrease, thus setting an operative limit at around 80-100 degrees Celsius. [63], [72]. Having the PVDF in the piezofoil a capacitive behavior, the charges collected by the two electrodes slowly cancel each other, thus this sensor can only measure pressure fluctuations and not the mean pressure field [63]. Being the piezofilm very sensitive and with a small mechanical attenuation, it has an almost inertialess measurement of the unsteady surface forces [72].

Hence, the main advantages of piezofoils over the other pressure measuring devices such as the transducers, concern the far lower manufacturing cost, the simpler installation process and the almost unlimited freedom the user has in the shape and placement of the sensing areas. This is especially true when working near the trailing edge area of an airfoil: in that case, finding the space for the pressure transducers or for the tubing inside the model can be very complicated. On the other hand, the piezofoil doesn’t require space inside the model, apart for some small circuitry, and has a clear advantage in all these situations. All this while having a very broad pressure range that can be measured, usually broader than pressure transducers of the same size, and with high frequency ranges.

1.3. Research Objective and Research Questions

Laminar separation bubbles are highly dynamic and unsteady phenomena taking place when a laminar boundary layer subjected to an adverse pressure gradient separates from the surface and subsequently reattaches creating an area of recirculating flow. Following the literature study it has been seen that vortical structures start to appear in the reattachment area, deforming and evolving as they convect downstream and later disintegrating into small scale vortices and turbulence; moreover, the separated shear layer oscillates in a random fashion giving rise to the phenomenon of flapping. Different measurement techniques can be employed to investigate such vortical structures and their dynamic behavior: particle image velocimetry is a commonly used techniques but present some disadvantages, namely cost and complexity. Another common technique concerns the use of pressure transducers to record the wall pressure fluctuations. The advantage of the wall-mounted pressure transducers is their ability to accurately measure fluctuations at the wall (which cannot be taken for granted with PIV) but have the disadvantage of having a lower spatial resolution (especially when considering wide areas) and their installation can pose problems when they need to be fit in tight spaces. In general, being able to infer the relevant dynamic phenomena from the wall pressure fluctuations is quite appealing since it simplifies the experimental setup. If the pressure fluctuations are recorded using a piezoelectric foil, the advantages are even greater and new experimental possibilities can open.

Hence, the present study aims to relate the surface pressure distribution of laminar separation bubbles to their dynamic phenomena, namely flapping and vortex shedding. The focus will be on measuring the frequency and amplitude of the pressure fluctuations in the bubble and characterizing the pressure imprint of flapping and vortex shedding. Moreover, the study also aims of investigating the best measurement location to capture flapping and vortex shedding in the separation and reattachment area respectively. The formulation of the research objective is the following:

Research Objective

Investigate the effects on the surface pressure distribution of the relevant dynamic phenomena in a LSB employing piezoelectric sensors.

To address the research objective stated above, the following research questions and subquestions will need to be answered:

Research Question

How do the pressure fluctuations frequency and amplitude vary in a LSB?

1. What is the streamwise pressure fluctuation distribution in the laminar separation bubble?
2. Can piezofoil and surface hot wires capture shear layer flapping and what is the best location to capture it?
3. Can piezofoil and surface hot wires capture vortex shedding and what is the best location to capture it?
4. Do the velocity and pressure fluctuations match in the reattachment area and, in general, along the length of the LSB?

2

Methodology

2.1. Wind Tunnel Facility

The Boundary Layer Wind Tunnel of the aerodynamic department of the Technische Universität of Berlin is a closed-loop, low-speed wind tunnel with a top velocity of 27 m/s and a test section of 0.60 m x 0.43 m x 1.20 m (width x height x length). The test section is made out of wood and has acrylic panels to allow for optical access. Adjacent to the test section, a three-axis traverse system can be used to position experimental equipment, including probes and laser-optical hardware. The temperature inside the tunnel is regulated by a heat exchanger with a cold water supply. During the tests the temperature was held at around 22°C. The freestream turbulence intensity between 10 and 5000 Hz was below TI=0.14% in the range of freestream velocities between 8 and 20 m/s. The velocity in the wind tunnel is set and adjusted knowing the static pressure difference between a set of pressure taps located at the beginning and at the end of the contraption section. Through a calibration curve, the pressure difference is referred to the flow velocity, measured with a pitot tube. The error on the set velocity is $\approx +0.68\%$ and $\approx +0.78\%$ at 10 and 20 m/s, respectively. The solid blockage was computed and amounted to 1.5%. Due to the small value no solid blockage corrections were applied. The test section has straight walls and thus does not take into account the effect of buoyancy: however, the effect of buoyancy was not corrected, as it is usually insignificant for wings, as opposed to fuselages and nacelles [49]. The structure of the boundary layer wind tunnel can be seen in Figure 2.1.

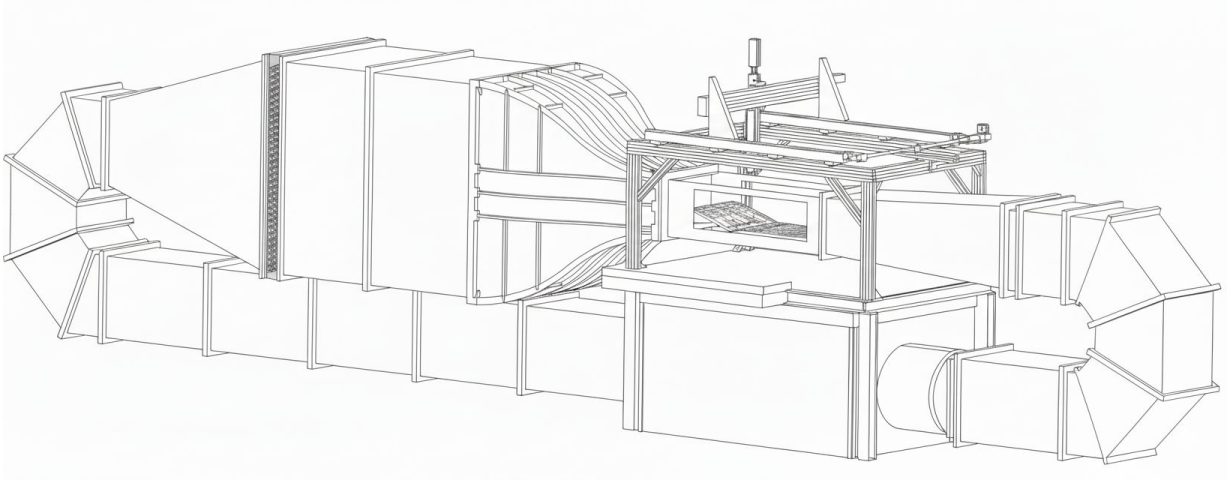

Figure 2.1: Boundary layer wind tunnel of the Technische Universität of Berlin (flow is from left to right in the test section part) [73]

2.2. Wing Model

The model used during the test was a balsa wood wing spanning the whole test section width with a NACA 0015 airfoil section. The wing had a chord length of 0.2 m and the same span as the test section width,

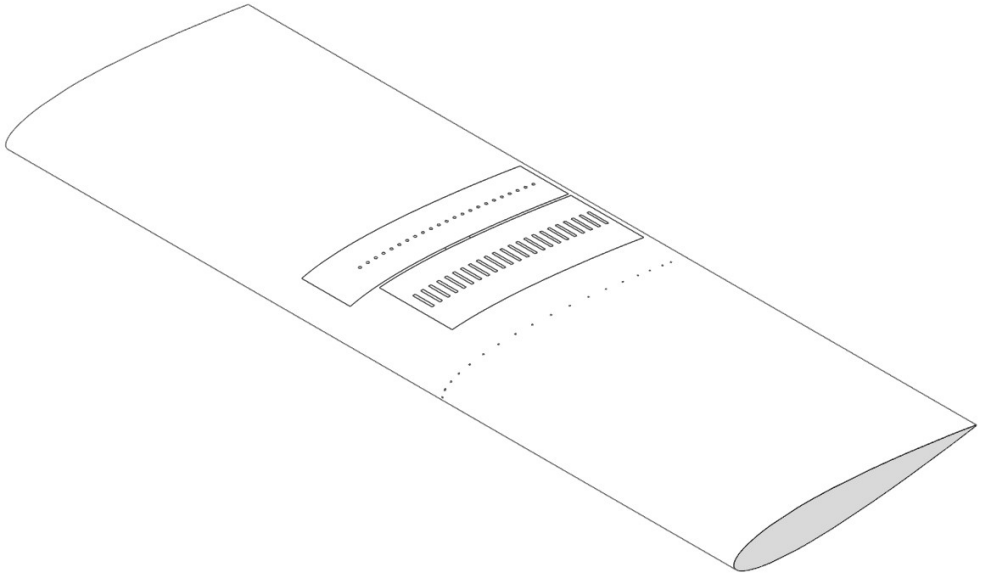

Figure 2.2

that is 0.6 m. The wing was built in-house at TU Berlin. The instrumentation on the wing includes 28 pressure taps distributed on both the suction and pressure side of the wing that can be connected to pressure transducers. Moreover, the wing features a ”slot” on one of the sides of 60 mm x 158 mm, where an instrumented 3D printed plug can be inserted. An instrumented plug with surface hot wires has been used in the test campaign. The wing angle of attack was set manually using the reading from an electronic level with a maximum error of 0.1 degrees and, for angles of attack between 0 and 9 degrees the angle was mechanically set using a pin.

2.3. Surface Pressure Taps

Surface pressure taps are one the most common measurement techniques in wind tunnel testing and they are used extensively to obtain static pressure coefficient distributions. Depending on the tube length between the pressure taps and the pressure transducer and on the pressure transducer itself, they can also be used to investigate the pressure fluctuations.

The wing model featured 28 pressure taps, 19 on the top surface and 9 on the bottom surface, located on a plane at around z/c=0.4. The pressure taps had a diameter of 0.4 mm and the tube length between the taps and the pressure transducers was around 1.45 m. The pressure transducers used in the experiments were All Sensors 1 INCH-D2 P4V-MINI which have a pressure range from -1 to +1 inch of H_2O corresponding to ± 249.089 Pa and All Sensors 5 INCH-D2 P4V-MINI which have a pressure range of ± 1244.2 Pa. Five 5-inch pressure transducers were connected to the first five pressure taps while the remaining pressure taps were connected to the 1-inch sensors. The 5-inch transducers where used close to the leading edge on the suction side, because the local pressure, at certain freestream velocities, could drop out of the pressure range of the 1-inch transducers, saturating them.

The sampling frequency and sampling time chosen for the measures were 5000 Hz and 30 s, respectively. Due to the long connecting tubes between pressure taps and pressure transducers the high frequency fluctuations would have been dampened out and thus, the selected sampling frequency is relatively low. The 30 s of sampling time guaranteed the convergence of the statistical quantities. The pressure transducers were calibrated using a Halstrup Walcher KAL 84 pressure calibration device to get the individual calibration curves and thus, the individual calibration constants.

2.4. Piezofoil

2.4.1. Design

As already discussed in Section 1.2.3, the piezofoil uses a piezoelectric material that develops electric charges when strain is applied. The mechanic deformation of the material due to pressure is hence converted in an electric signal.

The piezofoils were fabricated by screen-printing of a $28\mu m$-thick PVDF foil (PolyK®) on which the sensing elements were printed with silver conductive ink (Bectron® CP 6667). The PVDF layer lies on top of the Flex-PCB layer, constituted of a Polyethylene (PE) layer that has been printed with silver ink to create electrical connection between the sensing elements and the acquisition system. The two layers are then joined with the 3M™ 9703 anisotropic conductive adhesive, a special adhesive containing dispersed silver nanoparticles, facilitating electrical conductivity between the Flex-PCB and the PVDF layer [63]. The different piezofoil layers can be seen in Figure 2.3. The sensor production process for the PVDF and Flex-PCB layers is conducted in the laboratory of Hochschule für Technik und Wirtschaft Berlin. The production process starts by creating a stencil of the desired pattern and then using it to screen print onto the PVDF and PE layer with silver ink. After printing, the material is heated to allow the metallic ink to cure and enhance its electrical and mechanical properties. This process guarantees almost unlimited versatility in the creation of patterns making it suitable for a wide range of applications. More information about the piezofoil manufacturing process can be found in the reference by Wang et al. [74].

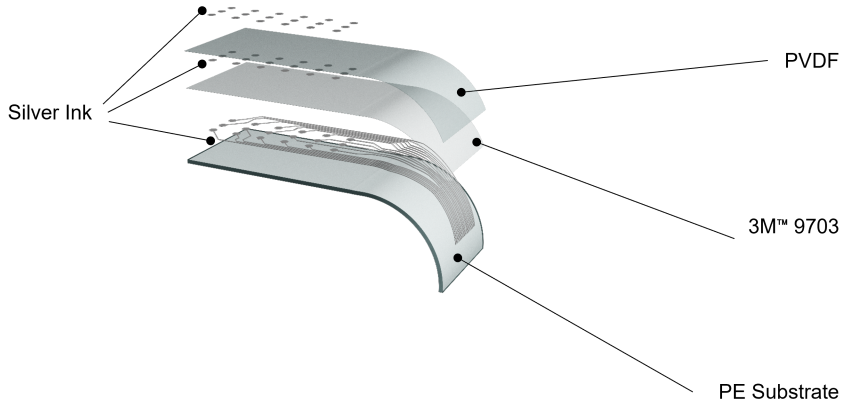

Figure 2.3: Piezofoil schematics. The actual sensing elements lie on the PVDF layer, while the ink traces on the PE substrate provide the electrical connection to the amplifier. The 3M™ 9703 has the double function of keeping the two layers together and allowing electrical connection between ink traces on the PVDF and on the PE substrate.

In the present investigation, two different piezofoil designs have been employed, both featuring 24 circular sensing elements of 3 mm of diameter each: the first design, referred to as the "*in-line design*", featured sensing elements evenly spaced along a single line, with 6.5 mm between each element. Spanning from $x/c \approx 0.21$ to $x/c \approx 0.96$, it covers almost all the wing chord maintaining nonetheless an acceptable spatial resolution. The spacing of the sensing elements was validated using pressure coefficient distributions and found to be adequate for the investigated speeds and angles of attack, as at least six elements were always located within the laminar separation bubble. The second design, referred to as the "*staggered design*", was divided into two halves: the part closer to the leading edge only featured 4 sensing elements distanced 12.5 mm; the part closer to the trailing edge featured the remaining 19 sensors, spaced 2.6 mm in the streamwise direction and staggered by 4 mm in the spanwise direction. The staggered design was significantly shorter than the previous one, spanning from $x/c \approx 0.16$ to $x/c \approx 0.65$. This configuration allowed for a denser spatial resolution in the half of the wing closer to the trailing edge, region where the reattachment area would lie for low angles of attack, but still maintaining some sensing elements inside and before the laminar separation bubble. The two piezofoil designs can be seen in Figure 2.4.

The number of sensing elements was primarily determined by the available amplifier setup, which included 24 channels, thus setting the maximum number of sensors that could be installed. However, both piezofoils show 26 circular elements: the first and last elements are not active elements but electrical

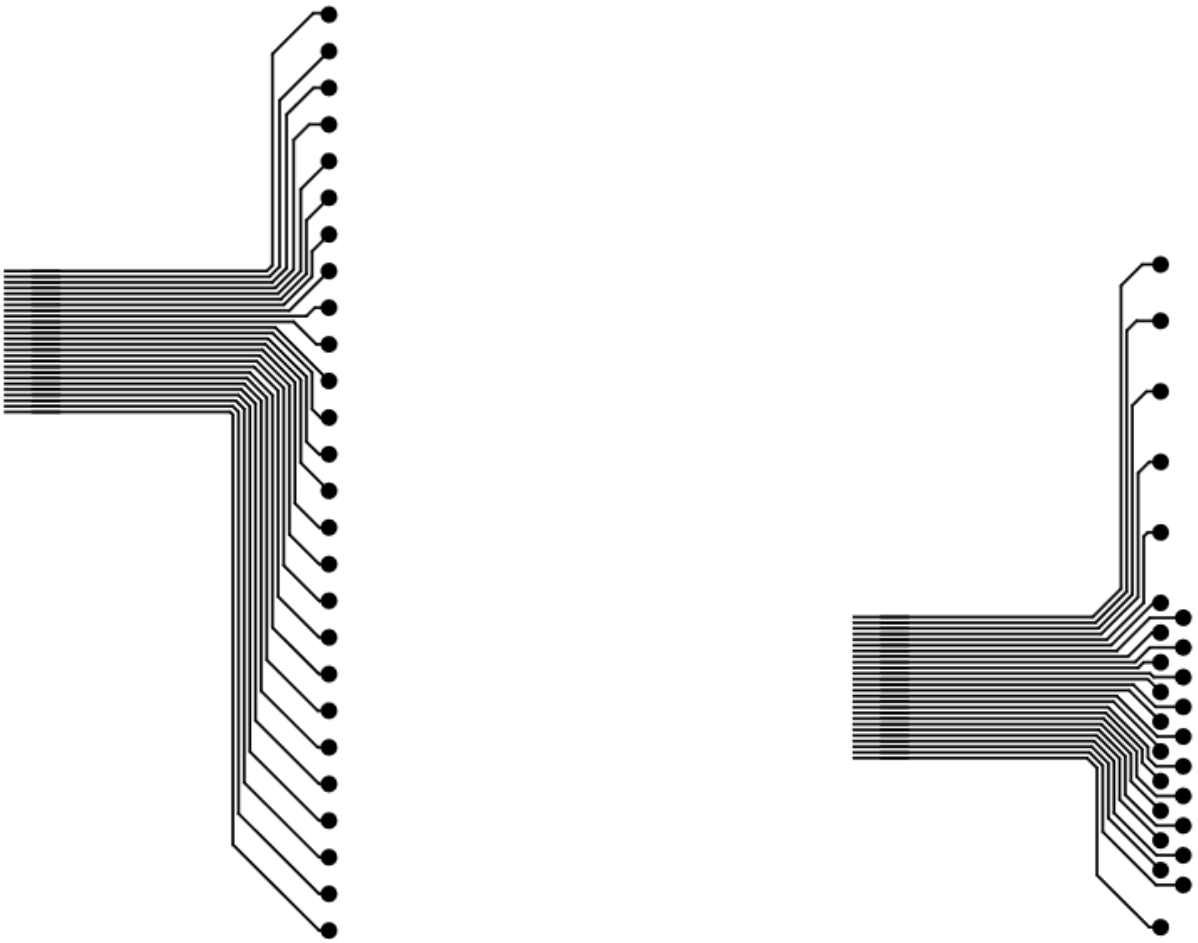

Figure 2.4: Piezofoil designs used in the investigation. Both designs feature 24 circular sensing elements of 3 mm of diameter each. First and last circular elements in each design are ground connections. (a) In-line piezofoil design. (b) Staggered piezofoil design. Shown are the silver ink traces screen-printed on the PE substrate.

grounds, necessary to have a return path for the 24 single ended channels. For what concerns the sensing element size, it was chosen keeping in mind the minimum requirements for frequency response and sensitivity. From a frequency response perspective, the sensing element should have the smallest possible area to resolve small-scale flow structures. However, reducing the sensor area significantly decreases sensitivity, and not in a linear manner. Therefore, it was necessary to find a compromise that would resolve smaller scale vortices while maintaining sufficient sensitivity to detect the relevant flow phenomena. Previous studies conducted at TU Berlin had investigated sensor diameters between 2 and 4 mm: Wang et al. [74] found out that the 4 mm diameters sensors exhibit the highest sensitivity with values of around $14\mu V/Pa$, the 3 mm diameter sensors show a sensitivity in the range of $7.7\mu V/Pa$, and the 2 mm diameter sensors present the lowest sensitivity with around $3.2\mu V/Pa$. Therefore, for the present study, a sensor side of 3 mm was chosen, offering the optimal balance between frequency response and sensitivity.

While the piezofoil is a relatively non-intrusive measurement technique, it does have a certain thickness. Given the sensitivity of laminar separation bubbles to flow instabilities, the step introduced by the piezofoil could potentially act as a source of disturbance. For this reason, the PE substrate at the base of the piezofoil was wrapped around the leading edge of the wing, until an $x/c \approx 0.12$ on the pressure side. On the other end, the PE substrate ended at the trailing edge. This solution eliminated significant steps in the flow, thereby minimizing potential disturbances that could affect the laminar separation bubble.

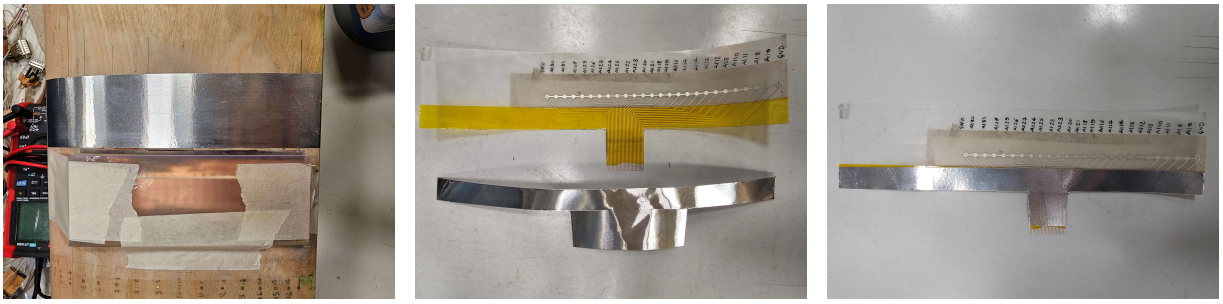

(a) (b) (c)

Figure 2.5: Shielding process of the piezofoil to attenuate the effects of the electromagnetic disturbances. (a) Shielded wings surface. (b) Piezofoil and metal tape mask. Kapton tape was applied on the piezofoil to prevent electrical connection between the piezofoil wires and the metal tape. (c) Shielded piezofoil.

Nonetheless, the 3M 9703 adhesive tape and the PVDF layers didn't wrap around the leading edge or arrive to the trailing edge, but their combined thickness was around $50\mu m$. This already low thickness, in conjunction with the fact that the piezofoil was pressed during installation, brought the thickness to even lower values and was deemed insufficient to produce relevant flow instabilities.

2.4.2. Shielding and Installation

The piezofoil is a high-impedance device and, as such, is very susceptible to electromagnetic interference, especially when considering that the test section and the wing are completely made out of wood and that the pressure fluctuations produced by the laminar separation bubble are quite low, in the order of tens of Pa. However, the extent to which noise could affect the measurements remains unknown. Previous studies [63] [75] investigated the performance of the piezofoil in the presence of turbulent separation bubbles under supersonic conditions (shockwave-boundary layer interaction at Mach 2). In those cases, the supersonic flow ensured large pressure fluctuations, and the wind tunnels, typically constructed from metal, provided a relatively clean measurement environment. The results demonstrated that the piezofoil is a promising measuring device for capturing pressure fluctuations in supersonic flows, however, its behavior in noisier environments and in the presence of low-amplitude signals remained unaddressed.

In the present study, preliminary investigations are carried out to quantify the effects of electromagnetic noise. It is found that such noise significantly impacted the measurements, complicating the analysis of the laminar separation bubble. To mitigate this problematic, two solutions are adopted: first, by shielding the piezofoil on top and below, and second, by heating the piezofoil from inside the wing, more on this in Section 2.4.4. Speaking of shielding, three main shielding parts are installed using conductive metal tape: first, a layer of metal tape is applied on the wing in the same area where the piezofoil is installed; second, an appropriately cut piece of metal tape is applied on top of the piezofoil to cover the wires coming from the sensing elements; finally, the adapter between the piezofoil and the amplifier is wrapped in metal tape. All three pieces are electrically connected and attached to a common electrical ground. Some of the shielding steps can be seen in Figure 2.5. After gluing the shielded piezofoil on the aluminum tape strip on the wing, the piezofoil connector is slid through a thin slot on the right side of the 3D printed plug and connected to the amplifier. The piezofoils sensing elements are located on a plane at around z/c=0.59. The installed piezofoils can be seen in Figure 2.8.

2.4.3. Calibration

In general, each piezofoil is calibrated in a dedicated calibration chamber prior to testing, to ensure uniformity in the piezoelectric material and consistency in the sensitivity of the individual sensing elements. The calibration procedure and the equipment used can be found in the article by Wang et al. [74]. In this study, however, the calibration chamber cannot be used due to the larger-than-usual dimensions of the piezofoils. In the past, ball-drop calibrations had been performed, where a small steel ball was dropped inside a tube and onto each sensing element to provide a known input. This approach proved to be challenging and not repetitive enough for the present study. An alternative idea would have been to install the piezofoil on a flat plate and then subject it to a fully turbulent flow. This way, assuming the

turbulent boundary layer to be produce the same signal on all the sensing elements, a calibration could have been carried out. However, once the piezofoil is glued to a surface it's almost impossible to remove it without damaging it. Therefore, the piezofoils are calibrated on the wing after having installed trip strips near the airfoil leading edge to provide a fully turbulent boundary layer. The wing has non-zero curvature, thus the turbulent signal will not be exactly the same for all x/c locations but it was deemed adequate for the investigation. In any case, previous piezofoil samples realized with the same manufacturing technique, presented good homogeneity in sensibility between the sensing elements, with older designs exhibiting an error of around $\pm 8\%$ from the mean values [74] and newer designs exhibiting an error of around $\pm 4\%$ from the mean value [76], attesting the reliability of the manufacturing process.

2.4.4. Heating

As already stated in Section 2.4.2, with the test section and the subsonic conditions considered in this study, the signal-to-noise ratio of the piezofoil alone is not sufficient to carry out the analysis of the relevant phenomena. In addition to the shielding of the piezofoil, a heating source is installed inside the wing with the goal of producing an heat flux through the piezofoil itself. In fact, the PVDF used in the piezofoil does not only have a piezoelectric effect but also a pyroelectric effect: the latter is caused by a temperature difference across the material resulting in a creation of electric charges on the surface of the material [77], [78]. The test are conducted with a 25°C temperature difference between the piezofoil and the freestream ($\Delta T_{pz-\infty}$), leading to increases in sensitivity of around 20 dB, as can be seen from Figure 2.6.

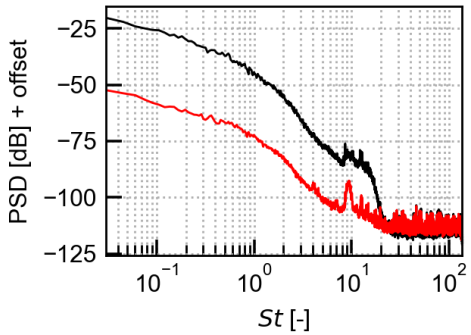

Figure 2.6: Power spectral density for non-heated case (red) and heated case at $\Delta T_{pz-\infty} = 25°C$ (black). The two spectra correspond to the same x/c location, where vortex shedding is taking place.

It needs to be kept in mind that the heating of the flow will affect the transition process more or less, depending on the extent of the heating process. Heating a section of the wing could locally alter the transition process with the result that different measuring device could see different flow behaviors. To avoid this issue, some test are carried out to quantify the influence of heating on the flow. Figure 2.7 shows the influence on the power spectral density (PSD) of different heating temperatures in the case of a 11 m/s flow and with the wing at 4 degrees of angle of attack. From the pictures it can clearly be seen how increasing the temperature difference between the piezofoil and the freestream air ($\Delta T_{pz-\infty}$) the sensitivity of the device increases, producing far more clean spectra. At the same time, the peaks observed between $x/c = 0.438$ and $x/c = 0.475$, and associated to the laminar separation bubble vortex shedding, become increasingly pronounced with rising temperature. However, their frequency and streamwise position remain unchanged, indicating that the transition process is not significantly affected at these temperatures.

2.5. Surface Hot Wire Anemometry

Surface hot wires are measuring devices that consist of thin, electrically heated wires placed flush with a surface and with a tiny slot underneath. They are used to measure wall shear stress and near-wall flow fluctuations. Their working principle is identical to standard constant-temperature hot wire anemometry. An electric current flow through the wire, heating it up, while the Wheatstone bridge maintains the wires temperature constant; as the wire is immersed in an airflow it gets cooled down by convection, requiring an increase in voltage to maintain its temperature, as the flow velocity increases. By directing a known airflow over the wire during calibration, a calibration curve can be generated, allowing the flow velocity to be determined.

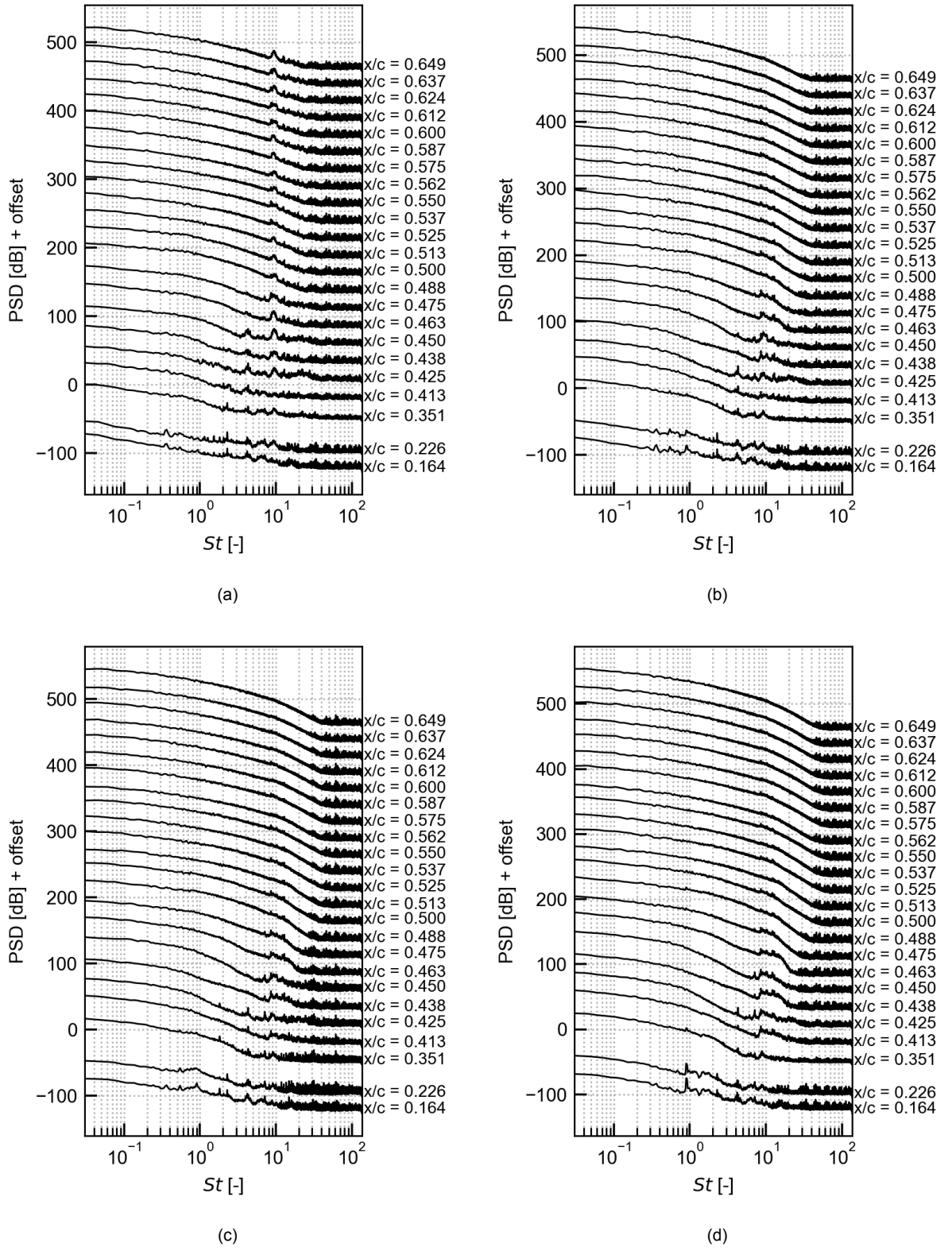

Figure 2.7: Effect of heating on power spectral density. Staggered piezofoil, $\alpha = 4$ deg, $Re = 144,000$, $T_\infty = 22°C$. First two sensors are likely broken. (a) Non-heated. (b) $T_{piezofoil} = 35°C$, $\Delta T_{pz-\infty} = 13°C$. (c) $T_{piezofoil} = 42°C$, $\Delta T_{pz-\infty} = 20°C$. (d) $T_{piezofoil} = 60°C$, $\Delta T_{pz-\infty} = 38°C$.

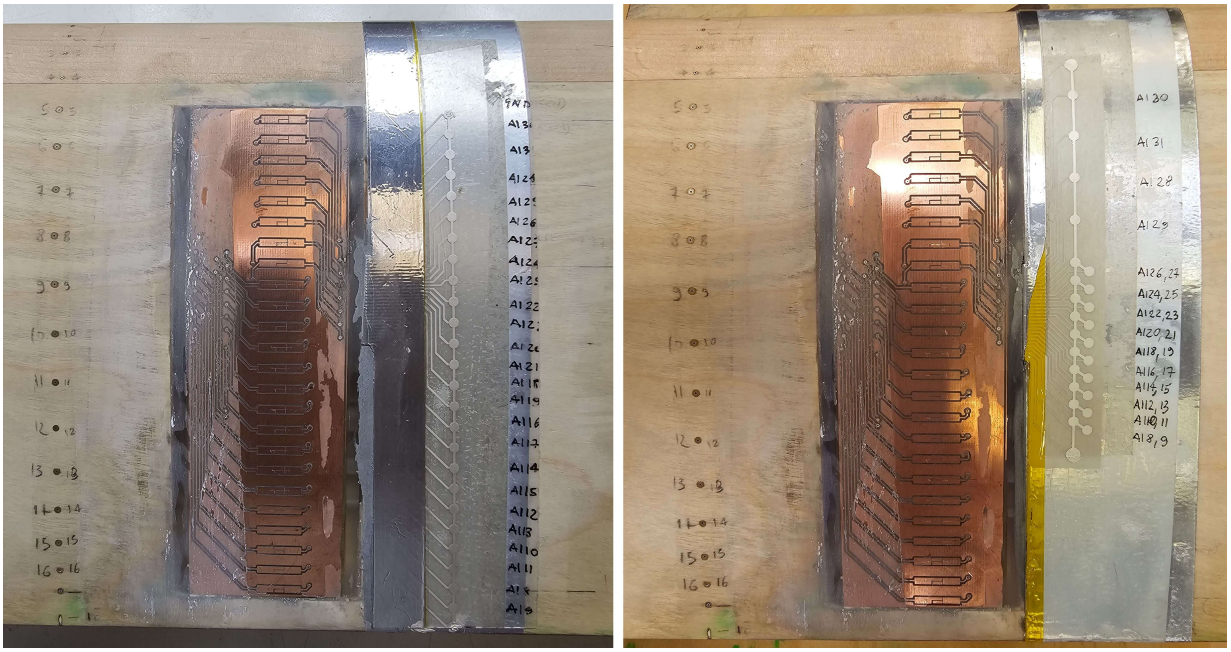

Figure 2.8: In-line (left) and staggered (right) piezofoil installed on the wing. Note the surface hot wire plug to the left of the piezofoil and the surface pressure taps to the left of the plug.

The thin platinum-coated tungsten wire ($\varnothing = 5\mu m$) is welded over a narrow slot ($\approx 0.1mm$) and set under weak tension. [79] The slots are obtained on a photo-etched flexible circuit board that also contains the electrical connection between the hot wires and the acquisition system. Because of the board flexibility, it's possible to integrate the sensor into curved surfaces such as wings. The whole system doesn't work differently from a standard hot wire setup: also in this case, the hot wires are connected to Wheatstone bridges, that have been previously calibrated. Each individual bridge is statically calibrated by assigning the correct value of resistance to the adjustable resistor, and dynamically calibrated by adjusting the hot wire response generated by a square wave. The cut off frequency found through the dynamic calibration was about 40000 Hz.

In the present study, a row of 24 surface hot wires are welded on a circuit board previously embedded onto a 3D printed plug. The spacing between the wires is 6.5 mm and they are placed directly next to the piezofoil. The hot wires lie on a plane at around $z/c = 0.51$. The surface hot wires array can be seen in Figure 2.8 and set up schematics in Figure 2.9.

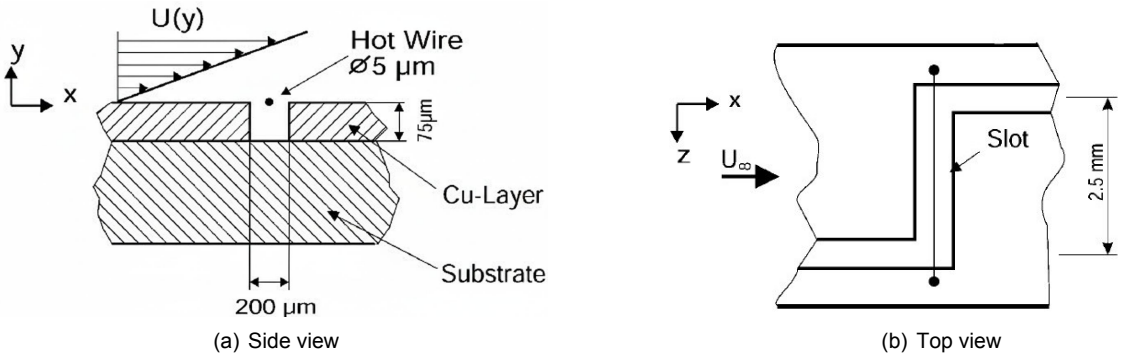

(a) Side view (b) Top view

Figure 2.9: Surface hot wire schematics. [79]

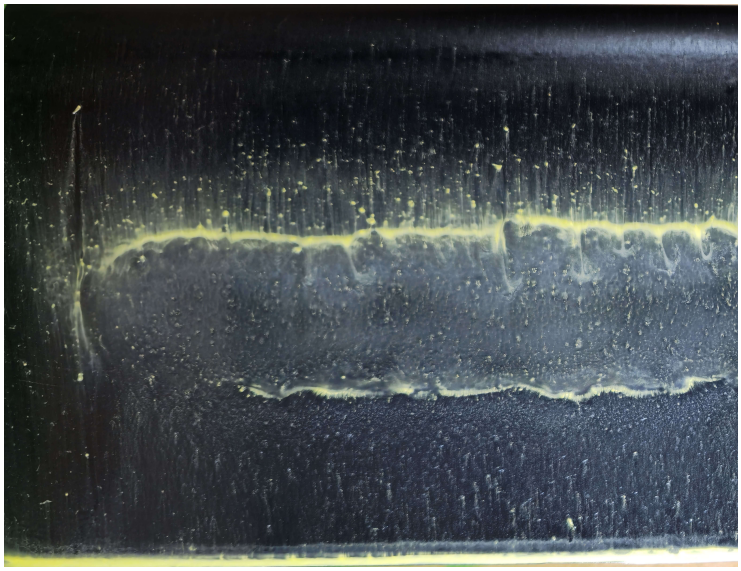

Figure 2.10: Oil flow visualization detail at $\alpha = 1$ deg, $Re = 197,000$. The upstream oil accumulation line individuates the mean separation location while the downstream oil accumulation line individuates the mean reattachment location.

2.6. Oil Flow Visualization

Oil flow visualization employs a thin film of non-volatile liquid to visualize the direction of the streamlines at the surface. The fluid is uniformly applied on the surface and it moves thanks to the shear forces at the wall. Its motion can be recorded and photographed to provide insight into flow behavior. This technique is particularly valuable for investigating flow separation and transition. A very common fluid employed is mineral oil, with or without the addition of pigments or fluorescent additives. The viscosity of the fluid must be selected depending on the speed and duration of the test. In the present work, a mix of equal parts of mineral oil and turpentine, with the addition of a pigment, is used. The wing model is then subjected to 30 minutes of continuous wind tunnel run time at a fixed Reynolds number and angle of attack.

In presence of a laminar separation bubble, the oil pattern shows a specific behavior. In the laminar area upstream of separation, the oil is quickly swept from the surface, leaving smooth oil streaks. At separation, the friction coefficient quickly goes to zero and the oil, vanishing the shear forces, begins to accumulate. Just after separation, in the dead-air-region, there is almost no movement at the wall and the oil largely retains the texture present prior to the wind tunnel run. Transition itself cannot be directly captured by oil flow visualization, as it occurs within the shear layer above the airfoil surface. Downstream of this point, at reattachment, as the rollers shed by the shear layer start to collide with the surface, the shear stress increases and sweeps away the oil both downstream and upstream of the reattachment point: hence, some oil is entrained in the recirculation area inside the bubble, and some is advected by the turbulent reattached boundary layer towards the trailing edge, where it accumulates. Based on this behavior, the mean separation line can be located just before of the first oil accumulation and the mean reattachment line as just after the second oil accumulation, as illustrated in Figure 2.10.

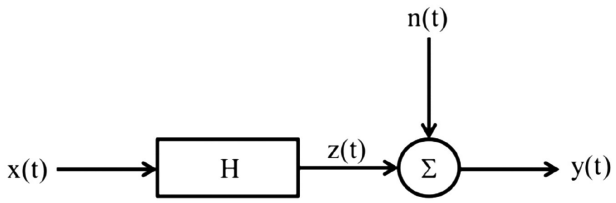

Figure 2.11: Scheme of the single-input/single-output system for the correction technique [80].

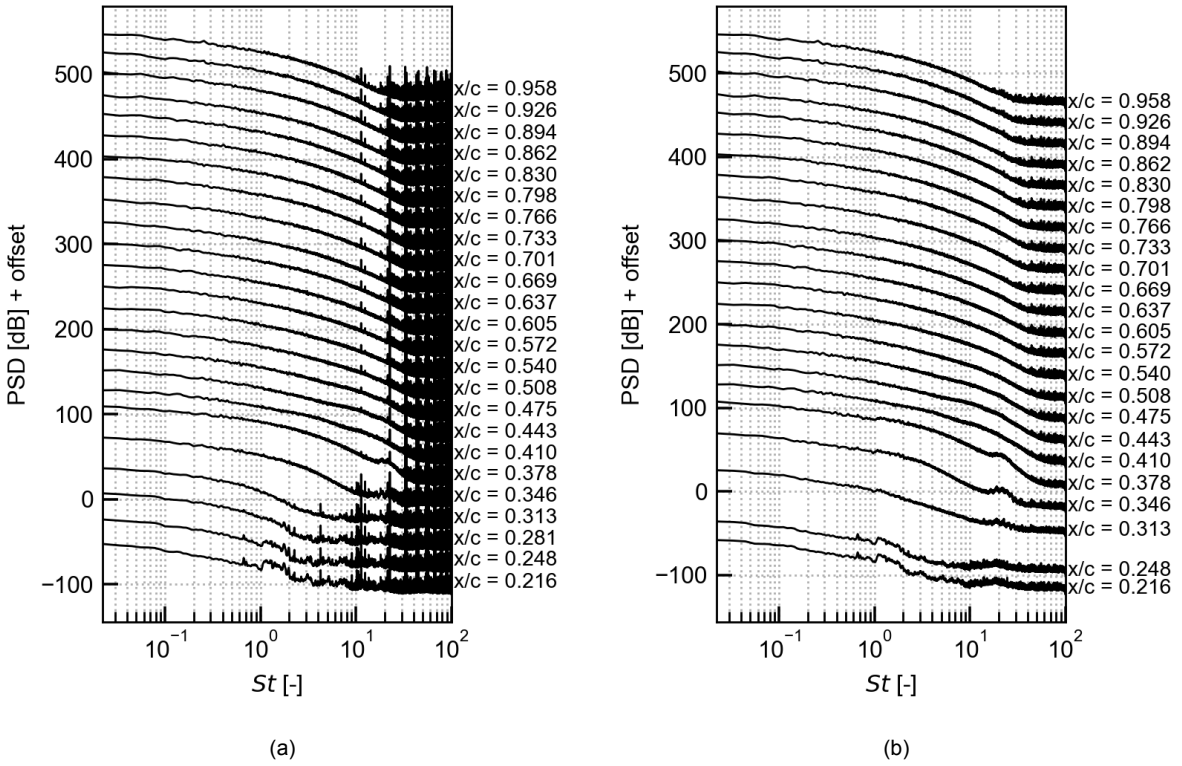

Figure 2.12: Example of the uncorrected (a) and corrected (b) in-line piezofoil spectra at $\alpha = 5$ deg, $Re = 197,000$. The third sensor from the leading edge has been used as the reference sensor in the corrected plot (x/c=0.281) and has been removed.

2.7. Signal Conditioning and Acquisition System

Pressure transducers and surface hot wires follows a more traditional setup: the former feed their signals directly into the acquisition system, while the latter pass the signals through Wheatstone bridges, one for each surface hot wire, before reaching the acquisition system. The piezofoil, on the other hand, outputting voltages in the order of the millivolts (mV), needs an amplification system in order to obtain readable signals with good signal-to-noise ratios. In the present work a charge amplifier has been used. The benefit lies in the fact that the output voltage only depends on the feedback capacitance and not on cable and sensor capacitance, allowing the use of longer cables in the setup. The cut off frequencies of the amplifier were defined starting from its design parameters: the low cut off frequency results in 1.59 Hz while the high cut off frequency lies in the megahertz (MHz) range.

Signal acquisition is carried out with National Instruments PXIe-4497 and PXIe-4303 data acquisition cards. These 24-bit high-speed cards, having 16 and 32 channels respectively, are synchronized in order to measure simultaneously surface hot wires and piezofoil.

The surface pressure taps are recorded with a sampling frequency of 5000 Hz and a sampling time of 30 s, as explained in Section 2.3. Surface hot wires and both piezofoils are recorded at a sampling frequency of 15000 Hz and a sampling time of 30 s. The relatively high sampling frequency is justified by the vortex shedding frequencies, reaching values in the order of 1000-3000 Hz. To ensure adequate resolution, the upper frequency limit is multiplied by a factor of five, resulting in the selected sampling frequency. In all cases, the sampling time of 30 s is chosen to guarantee the convergence of the statistical quantities.

2.8. Data Processing

2.8.1. Signal Filtering

Different methods are present in the existing literature to filter out noise contamination from useful signals. One of the simplest methods concerns the subtraction of the signal acquired in wind off conditions (at $V_\infty = 0$) to the noisy signal that needs to be cleaned. This can help clean out electromagnetic interferences in the spectra but cannot remove noise, from the flow or electromagnetic, that is not present in wind off conditions. A common method employs a subtraction technique where the signal from a reference sensor is subtracted from the contaminated signal. The two pressure transducers should measure fluctuations of equal mean-square values and with uncorrelated turbulent contributions [81]. However, effective use of this method relies on the assumption that the first sensor captures the contaminated signal of interest, while the reference sensor captures only the noise to be eliminated. If this assumption does not hold, undesirable effects may occur, such as zero or negative values in the spectrum. The method used in the present work comes from Weiss et al. [81] and it involves a correction method based on the signals coming from two sensors. This method only yields the spectrum of the corrected signal and it does not require that the two sensors measure the same turbulence statistics [81]. The method is based on single-input/single-output relationship of linear systems, as can be seen in Figure 2.11. First, it is assumed that the input $x(t)$ is the time signal of the noise present in the facility. Then, the linear system H models the flow phenomenon in exam, in this case the laminar separation bubble flow, and its output $z(t)$ represents the fluctuating signal in the LSB caused by the noise signal $x(t)$. $n(t)$ is the fluctuating signal of the phenomenon under study, that is the LSB, thus what it's of experimental interest, and it's uncorrelated with $x(t)$. The total fluctuation measured inside the laminar separation bubble is $y(t) = z(t) + n(t)$. Hence, the signal of interest $n(t)$ cannot be measured directly because the transducers will always measure the total fluctuation $y(t)$. The power spectral density of $n(t)$ ($G_{nn}(f)$) is given by:

$$G_{nn}(f) = [1 - C_{xy}(f)]G_{yy}(f) \tag{2.1}$$

where $G_{yy}(f)$ is the power spectral density of the noisy signal $y(t)$ and $C_{xy}(f)$ is the magnitude-squared coherence function of $x(t)$ and $y(t)$. Assuming that the laminar separation bubble responds linearly to noise fluctuations, and measuring simultaneously the noisy signal $y(t)$ and the noise signal $x(t)$, the power spectral density of the clean signal $G_{nn}(f)$ is given by the part of the power spectral density signal $G_{yy}(f)$ that is uncorrelated with the power spectral density signal $G_{xx}(f)$. This correction method is applied to both piezofoils and surface hot wires data, using as reference sensor one of the first sensors close to the leading edge. The reference sensor spectrum is removed by the corrected power spectral density plots. In this case, the drawback of the method lies in the use of one sensing element as the reference sensor, resulting in the loss of one spectrum in the corrected PSD plot. A better approach would involve a dedicated reference sensor placed upstream of the bubble, only measuring the noise.

Figure 2.12 shows the differences between the power spectral densities of the uncorrected and corrected spectra for the in-line piezofoil. The noise in the laminar spectra, as well as the noise above 1000 Hz, is significantly reduced, greatly improving readability, at the cost of loosing one sensor.

2.8.2. Standard Deviation Normalization

The unfiltered standard deviation plots of the surface hot wires and the piezofoil show great oscillations and peaks in the standard deviation value, especially after reattachment, region where the turbulent pressure fluctuations are expected to be more or less similar in amplitude. For the fully turbulent case without a laminar separation bubble, the standard deviation exhibits a random distribution around an approximately constant mean value, characterized by numerous sharp peaks and oscillations, as can be seen in Figure 2.13. This behavior seems odd, as a more or less constant value of the standard deviation, as x/c increases, is expected for a fully turbulent flow on a wing, as Celik et al. [82] and Branch et al. [83] show. Moreover, the multiple peaks in the standard deviation distribution made more challenging the identification of the peak connected to the shear layer reattachment, as can be seen in Figure 2.13 looking at the green dashed line. This presence of peaks and big oscillations in the standard deviation of both the fully turbulent and non-normalized case are to be attributed to differences in the soldering process of the hot wires on the board. Since they are soldered by hand, different wires can be more or less in tension, resulting in slightly different heights of the individual wires in the boundary layer. To address this inconsistencies between the wires, a normalization of each signal is carried out, dividing the

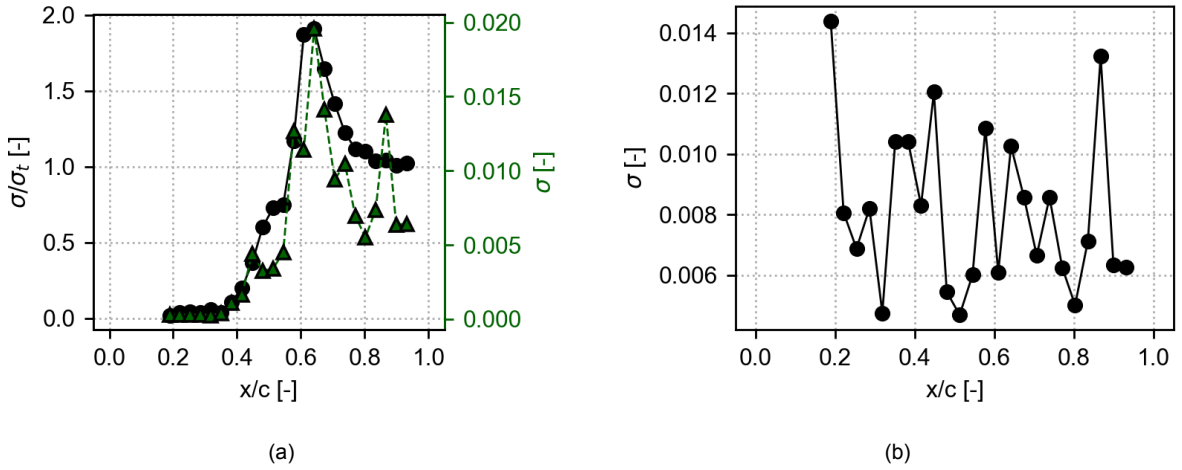

Figure 2.13: (a) Normalized (full black) and non-normalized (dashed green) standard deviation for the surface hot wires at $\alpha = 2$ deg, $Re = 197,000$. (b) Standard deviation of the fully turbulent case (no LSB) for the surface hot wires at $\alpha = 2$ deg, $Re = 197,000$.

raw standard deviation values for the corresponding values in the fully turbulent case. Figure 2.13 (a) show the comparison between the normalized and non-normalized standard deviation over the airfoils surface. The normalized standard deviation results much smoother, shows a distinct peak in the reattachment area and meets the expectations in the turbulent part, after the reattachment peak. Figure 2.13 (b) shows the standard deviation of the fully turbulent case, highlighting the differences in STD at different x/c locations. Differences that should not be as marked in a fully turbulent boundary layer on a wing.

3

Discussion of Results

3.1. Introduction

Three Reynolds numbers and four to five angles of attack, depending on the Reynolds number, were analyzed, as summarized in Table 3.1. The chord-based Reynolds numbers considered, 144,000, 197,000 and 262,000, are representative of conditions where laminar separation bubbles are typically observed. The selected angles of attack, from 1 to 5 degrees in 1 degree increments, ensured the presence of the longest possible LSBs, while still providing sufficiently strong fluctuations to yield a distinct signal. For the staggered piezofoil, the range of angles of attack is slightly narrower and Reynolds-number dependent, ensuring that the LSB remains located within the region of denser sensing elements. The surface hot wires are used to validate the results from the piezofoils. The pressure transducers and the oil flow visualization are used to characterize the mean flow features of the LSB.

$Device$	$Re\ [-]$	$\alpha\ [deg]$	$\Delta T_{pz-\infty}[°C]$
In-line Piezofoil	144,000	1,2,3,4,5	25
	197,000	1,2,3,4,5	25
	262,000	1,2,3,4,5	25
Staggered Piezofoil	144,000	2,3,4,5	25
	197,000	2,3,4,5	25
	262,000	1,2,3,4	25
Surface Hot Wires	144,000	1,2,3,4,5	-
	197,000	1,2,3,4,5	-
	262,000	1,2,3,4,5	-
Pressure Transducers	144,000	1,2,3,4,5	-
	197,000	1,2,3,4,5	-
	262,000	1,2,3,4,5	-
Oil Flow	144,000	1,2,3,4,5	-
	197,000	1,2,3,4,5	-
	262,000	1,2,3,4,5	-

Table 3.1: Cases analyzed in the result section

3.2. Tonal Noise Mitigation

It has long being known that airfoils immersed in an uniform stream at moderate Reynolds number emit acoustic tones. The emission of acoustic tones from airfoils has been subject of research dating back to the 1970s. Among the first investigations can be found the work by Hersh and Hayden [84] and by Paterson et al. [85], which proposed an empirical relation for predicting aerodynamic noise, called the ”Paterson formula”. In the case of low-turbulence intensity inflows and airfoils presenting laminar separation

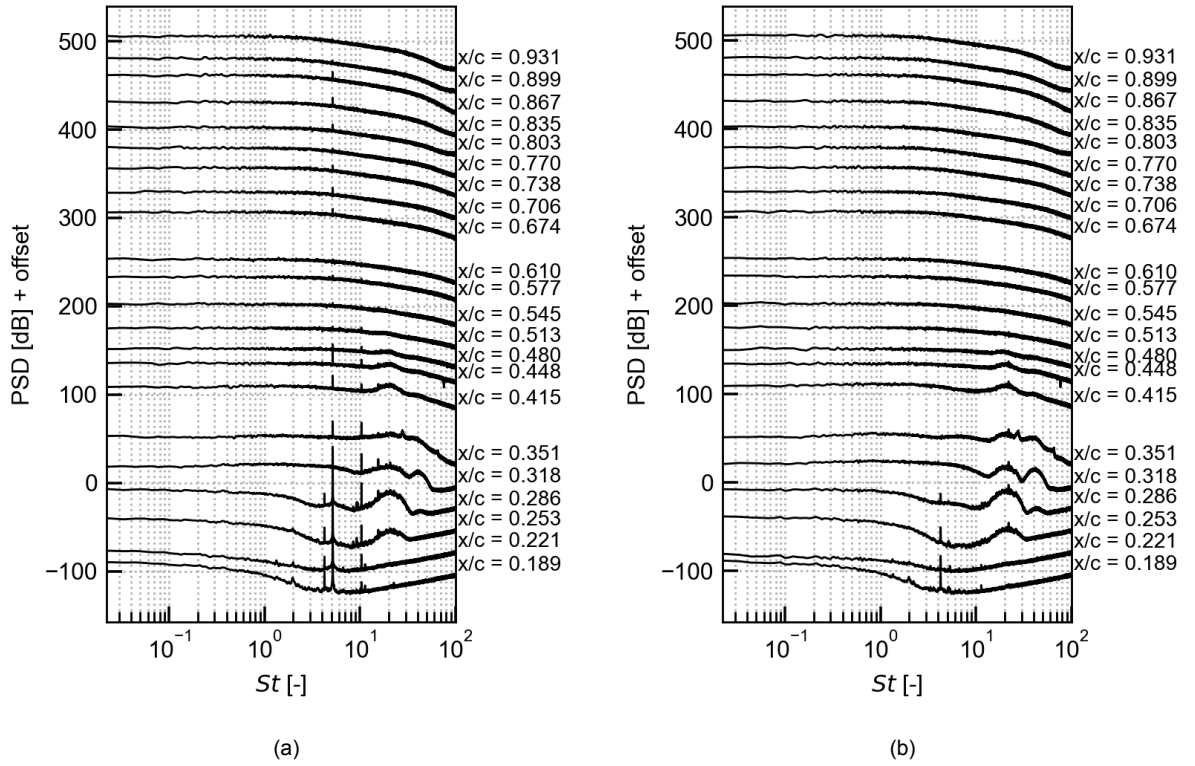

Figure 3.1: Power spectral density surface hot wire anemometry. Effect of the boundary layer tripping on the pressure side at x/c=0.12 on the acoustic tones at $Re = 144,000$ and $\alpha = 4$ deg. (a) No boundary layer tripping. (b) With boundary layer tripping. The empty spaces correspond to removed broken sensors

bubbles, the amplified instability waves roll up into vortical structures (the so called ”rollers”). These vortical structures can interact with the trailing edge, scattering acoustic waves. The generated acoustic waves also travel upstream and trigger the development of new instabilities. Hence, a feedback loop between the acoustic waves at the trailing edge and the laminar boundary layer upstream can form, resulting in a self-produced acoustic excitation that present a periodic vortex shedding at a narrow range of frequencies. [86] The instability waves and the vortical structures shed by the laminar separation bubble usually present high spanwise coherence, resulting in even higher tonal noise, in respect to cases with poorly coherent vortical structures.

The emission of acoustic tones is prominent in the symmetric NACA four-digits profiles, especially the ones with low thicknesses. The NACA 0012 profile is extensively used in tonal noise investigations [87] [88], but also the NACA 0015 and 0018 profiles show this phenomenon. Since tonal noise emission is often a consequence of laminar separation bubbles and since they can render more challenging the frequency domain analysis of the dynamic phenomena pertaining to laminar separation bubbles, in the present investigation it is decided to remove it using boundary layer tripping devices. More specifically, a zigzag tripping tape with a width of 8 mm and spanning the whole wing is installed on the pressure side at a non-dimensional chord length of $x/c = 0.12$. This measure had the objective of inducing the flow transition and creating a turbulent turbulent boundary layer on the part of wing downstream of the zigzag tape. The disappearance of the laminar boundary layer breaks, in theory, the feedback loop between the acoustic waves scattered at the trailing edge and the formation of new instability waves in the laminar boundary layer upstream of the bubble. The boundary layer tripping device is only present on the pressure side of the wing, for obvious reasons, but it’s interesting to mention that during tripping tests on the suction side of the wing, in the case of insufficient boundary layer tripping, the frequency domain analysis shows much cleaner spectra, almost with no acoustic tone presence. This obviously also affects the laminar separation bubble, reducing its length and shifting its position in respect to the case without tripping devices on the suction side. This observation further confirms the fact that the presence of sharp peaks in the spectra is

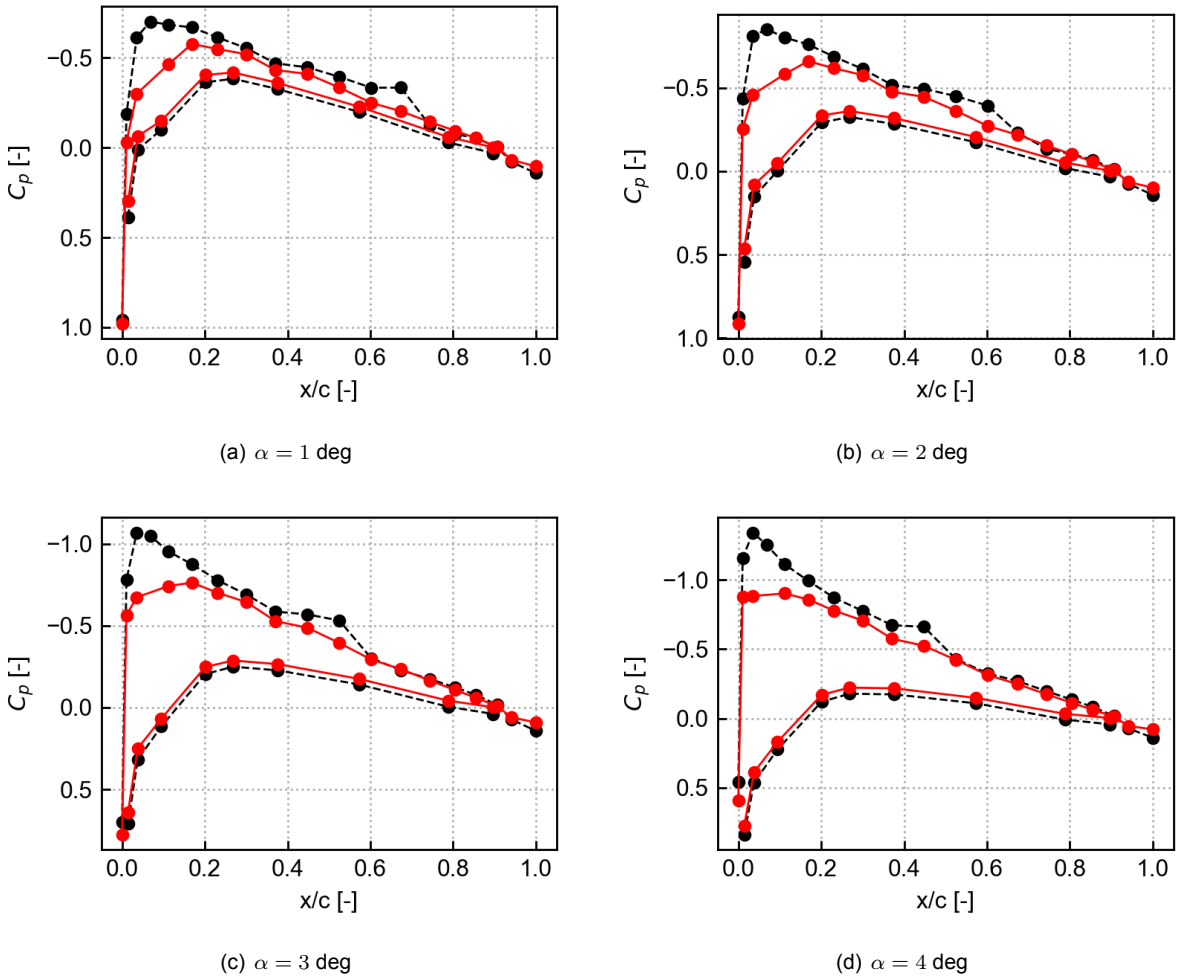

(a) $\alpha = 1$ deg

(b) $\alpha = 2$ deg

(c) $\alpha = 3$ deg

(d) $\alpha = 4$ deg

Figure 3.2: Pressure coefficient distributions at $Re = 197,000$. The red curve corresponds to the fully turbulent case (without LSB) and the black curve corresponds to the non-tripped case. In both cases the pressure side is tripped, as discussed in Section 3.2. In the red curve the 4th pressure transducer from the leading edge on the pressure side has been removed because blocked by the tripping tape.

due to the tonal noise feedback loop mentioned above. The boundary layer tripping tape applied on the pressure side has a positive effect on the full range of speeds and angles of attack investigated and its effect can be seen in Figure 3.1.

3.3. Laminar Separation Bubble Baseline Characterization

One of the most straightforward ways to identify the presence of a LSB is by examining the pressure coefficient distribution. Laminar separation bubbles present an initial plateau in the pressure coefficient distribution, the start of which corresponds to the mean shear layer separation point. If the flow fails to reattach, this constant pressure plateau extends to the trailing edge. When a laminar separation bubble is present, a sudden increase in pressure coefficient, following the constant pressure region, indicates transition and flow reattachment. This behavior can clearly be seen in Figure 3.2. The plots also clearly show that, at constant velocity, the laminar separation bubble moves upstream and becomes smaller as the angle of attack increases. Similarly, at a constant angle of attack, the LSB shifts upstream and decreases in size as the flow velocity increases, as can be seen from Figure 3.3. However, the location of the separation point, marking the onset of the pressure distribution plateau, should be interpreted with caution. The ninth pressure tap from the leading edge on the suction side consistently exhibits a dip in the pressure distribution, suggesting that the separation point is located at this position for different speeds

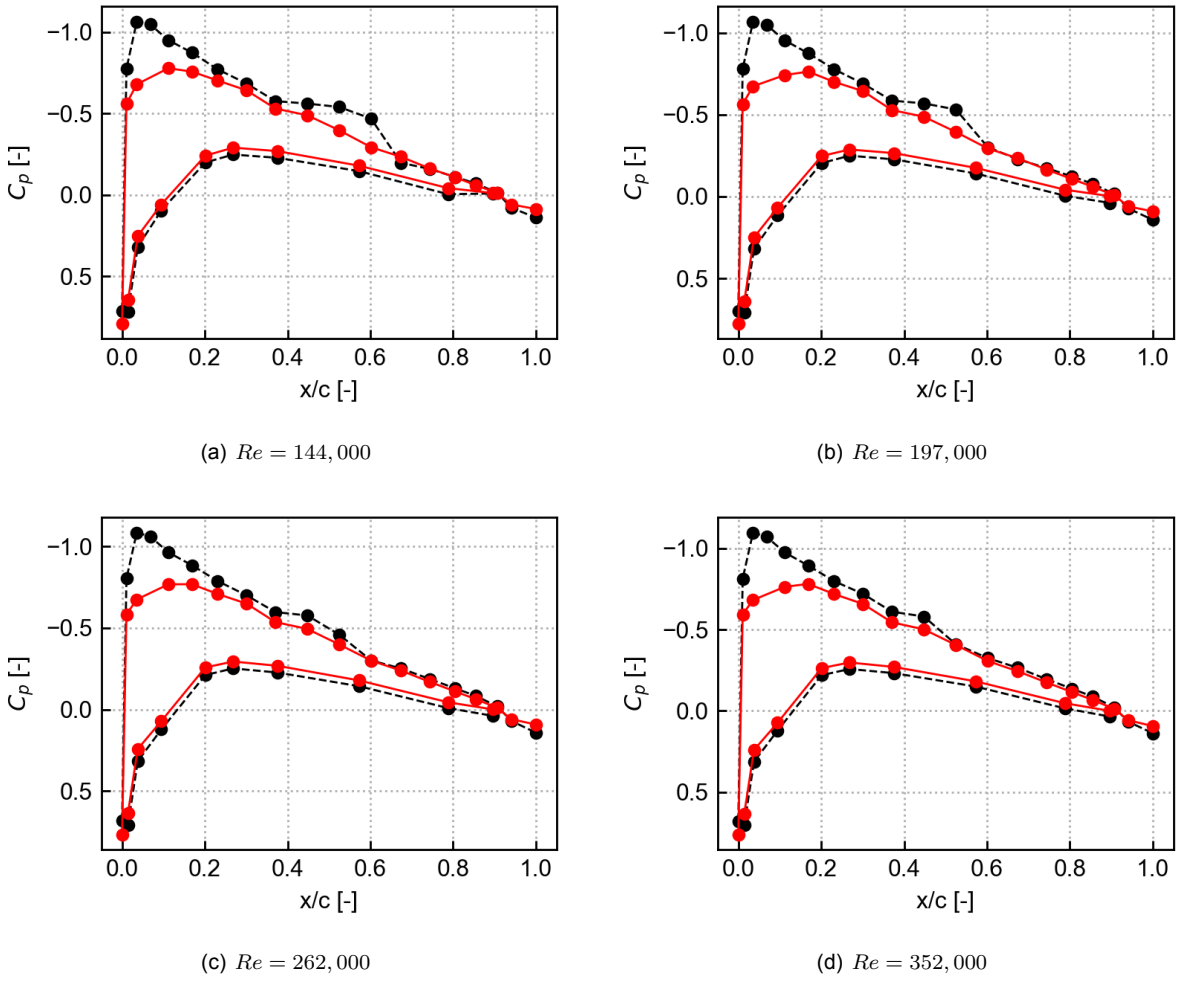

(a) $Re = 144,000$ (b) $Re = 197,000$

(c) $Re = 262,000$ (d) $Re = 352,000$

Figure 3.3: Pressure coefficient distributions at $\alpha = 3$ deg. The red curve corresponds to the fully turbulent case (without LSB) and the black curve corresponds to the non-tripped case. In both cases the pressure side is tripped, as discussed in Section 3.2. In the red curve the 4th pressure transducer from the leading edge on the pressure side has been removed because blocked by the tripping tape

and angles of attack. In addition to the pressure coefficient distribution, the laminar separation bubble position and dimensions can be determined via an oil flow visualization. In the oil flow the bubble moves the oil to form two distinct lines, corresponding to the mean separation line and the mean reattachment line, as can be seen in Figure 3.4. The oil flow visualization indicates a predominantly two-dimensional laminar separation bubble, with a localized oil accumulation observed near the start of the 3D-printed plug. The black plastic foil applied to the wing for the oil flow test introduces a small step at the plug's leading edge due to a setup imperfection. This discontinuity is sufficient to alter the local flow, shifting both the separation and reattachment lines upstream in that region. Consequently, the laminar separation bubble over the plug differs slightly from that observed on the remainder of the wing. In addition, the oil flow visualization displays streamwise streaks just upstream of the separation point, characteristic of laminar flow, as well as an accumulation of oil at the trailing edge, indicative of trailing-edge separation. The visualization also reveals the presence of corner vortices near the wing tips, although their influence on the laminar separation bubble is only marginal.

To estimate the location of separation point and reattachment point from the pressure coefficient distributions, denoted by S and R, respectively, the method presented by Gerakopulos et al. [89] is used. As shown in Figure 3.5 the separation location is estimated as the point of intersection between two linear fits: the first linear fit is applied to the nearly linear pressure recovery region after the suction peak, and the

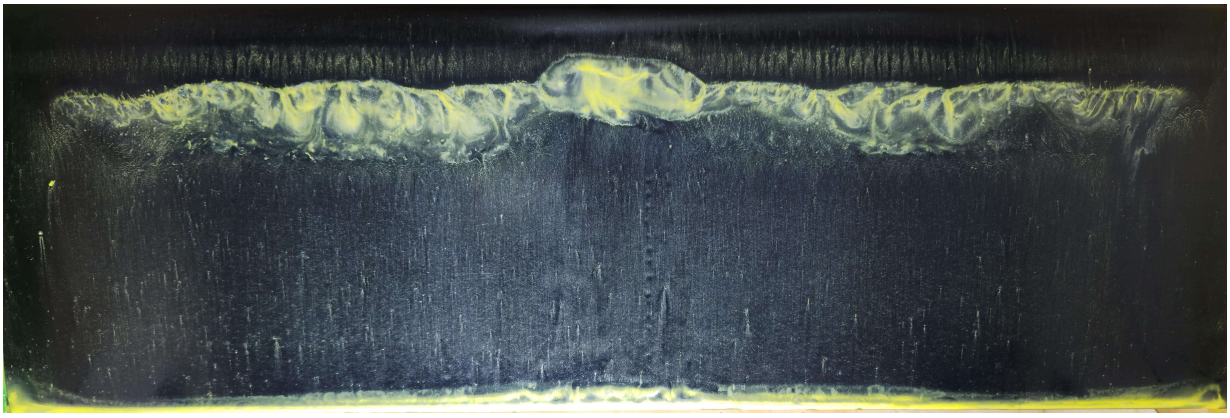

Figure 3.4: Oil flow visualization at $\alpha = 5$ deg, $Re = 262,000$.

second linear fit is applied to the pressure distribution plateau, that denotes the laminar part of the LSB. Reattachment is estimated through a polynomial fit applied to the regions of constant pressure coefficient and of rapid pressure coefficient recovery. The reattachment point can be identified as the location of local minimum of the second derivative of the polynomial fit. In the case depicted in Figure 3.5 the estimated separation point lies at $x/c = 0.3678$ and the estimated reattachment point at $x/c = 0.6020$.

Figure 3.5 summarizes the separation and reattachment locations obtained from the pressure coefficient distributions and oil-flow visualizations. The oil flow results indicate an upstream shift of the separation point with increasing angle of attack or Reynolds number, as expected. In contrast, the pressure transducers consistently suggest a nearly constant separation location, independent of angle of attack and freestream velocity. This apparent discrepancy can be understood by examining the C_p distributions: as previously noted, the ninth pressure tap from the leading edge on the suction side consistently records a higher pressure coefficient than its neighbors, producing the impression of a 'dip' at that position. Since the

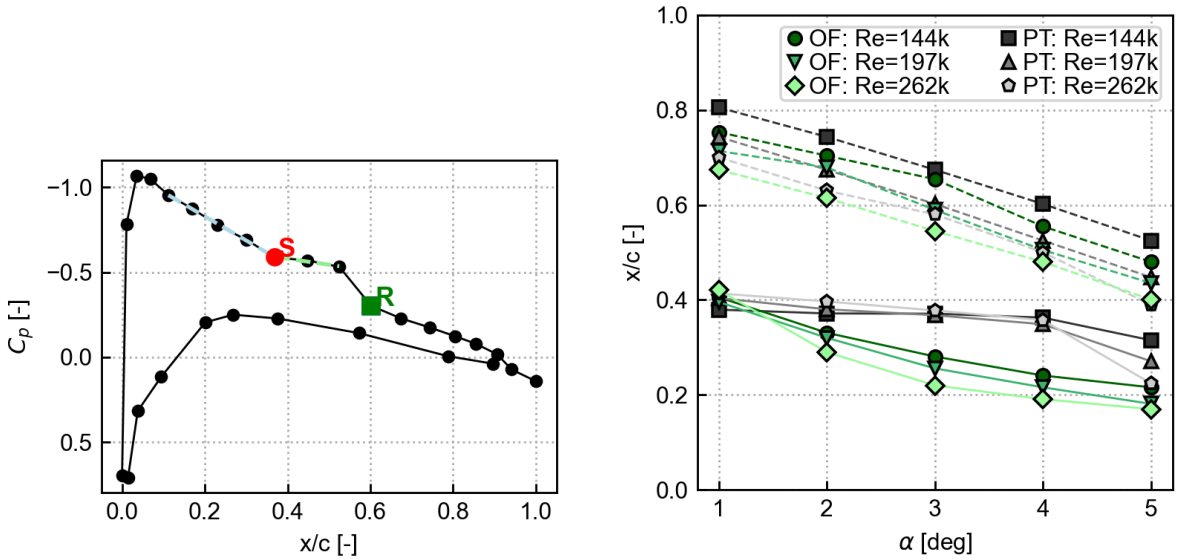

Figure 3.5: (a) Estimation of separation and reattachment location at $\alpha = 3$ deg and $Re = 197,000$. The blue line indicates linear fit of nearly linear region after suction peak, the green line indicates linear fit of the pressure coefficient plateau. (b) Separation and reattachment locations at different angles of attack for different Reynolds numbers. Solid lines indicate separation, dashed lines indicate reattachment.

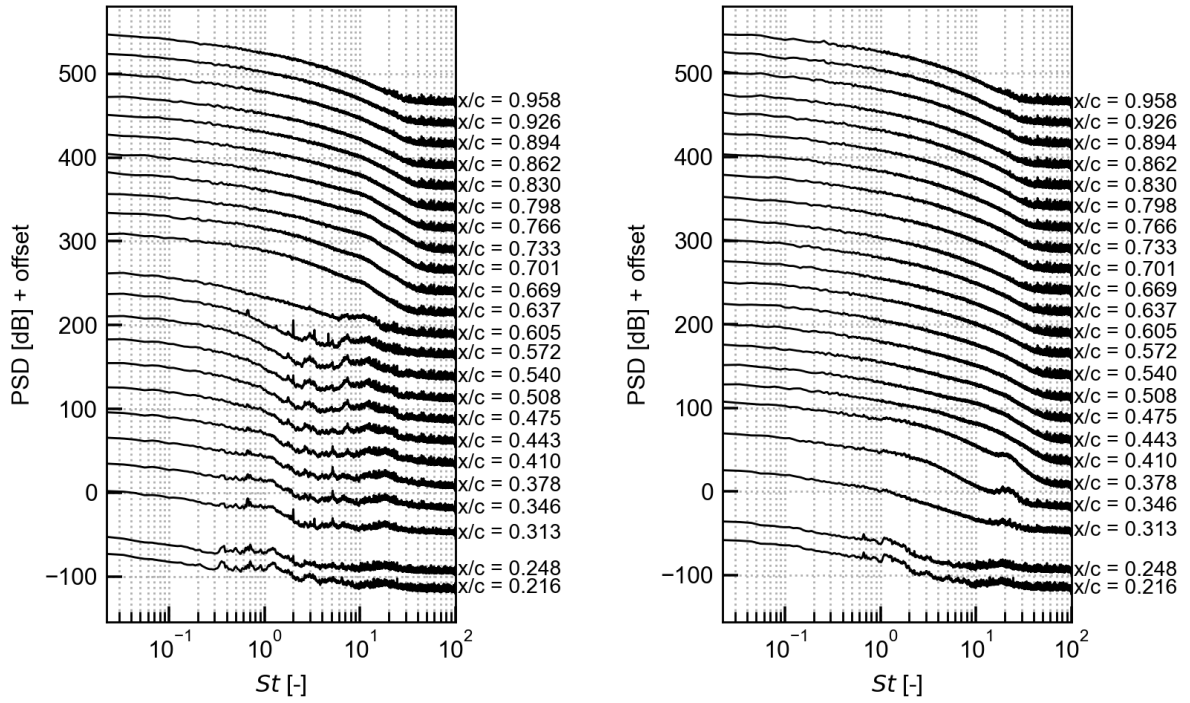

(a) $\alpha = 1$ deg

(b) $\alpha = 5$ deg

Figure 3.6: Power spectra density in-line piezofoil at $Re = 197,000$, $\Delta T_{pz-\infty} = 25°C$. First two sensors are likely broken, third sensor removed because used for filtering.

method used to estimate the separation location from the C_p distribution relies on two linear fits, such an anomaly can lead to a distorted prediction of the true separation point. This behavior may be attributed to limitations of the pressure transducers system, as their readings can be influenced by partially clogged taps or minor tube damage, which contribute to measurement inaccuracies. Regarding the reattachment location, the results from oil flow visualization and pressure taps show good agreement, particularly at the highest Reynolds numbers. Small discrepancies are to be expected, as the oil film, although minimally, does influence the behavior of the laminar separation bubble. Furthermore, both the separation and reattachment locations inferred from the pressure taps are subject to uncertainty, since they are estimated from discrete measurement points. In practice, the actual mean separation and reattachment points most likely lie between two adjacent pressure taps rather than directly on one of them. As expected, the reattachment point shifts upstream with increasing angle of attack or Reynolds number.

3.4. Flow Transition and Vortex Shedding

The mechanism of transition in laminar separation bubbles involves two separate phenomena: first the small flow instabilities in the boundary layer are amplified through the Tollmien-Schlichting waves; then, as the boundary layer separates from the surface, transition shifts to a Kelvin-Helmotz instability driven process. As the flow instabilities reach their climax, no longer being able of continuing to amplify, the flow starts to roll over, creating coherent vortical structures. These structures are commonly referred to as ”rollers” and the process behind them to ”vortex shedding”. It needs to be said that vortex shedding is just an aspect of transition and not a completely separated phenomenon. The rollers, as they move downstream, start to deform, loosing their coherence, until they break down into small scale turbulence. Figure 3.6 illustrates the formation, convection, and decay of coherent vortical structures. The sensors located near the leading edge record laminar flow, characterized by a weak and highly noisy signal. Further downstream, a distinct peak emerges, followed by spectra exhibiting both increased fluctuation amplitude and a clear dominant frequency. In subsequent sensors, this peak persists but progressively diminishes in prominence until the spectra become fully representative of turbulent flow. As expected, increasing angle

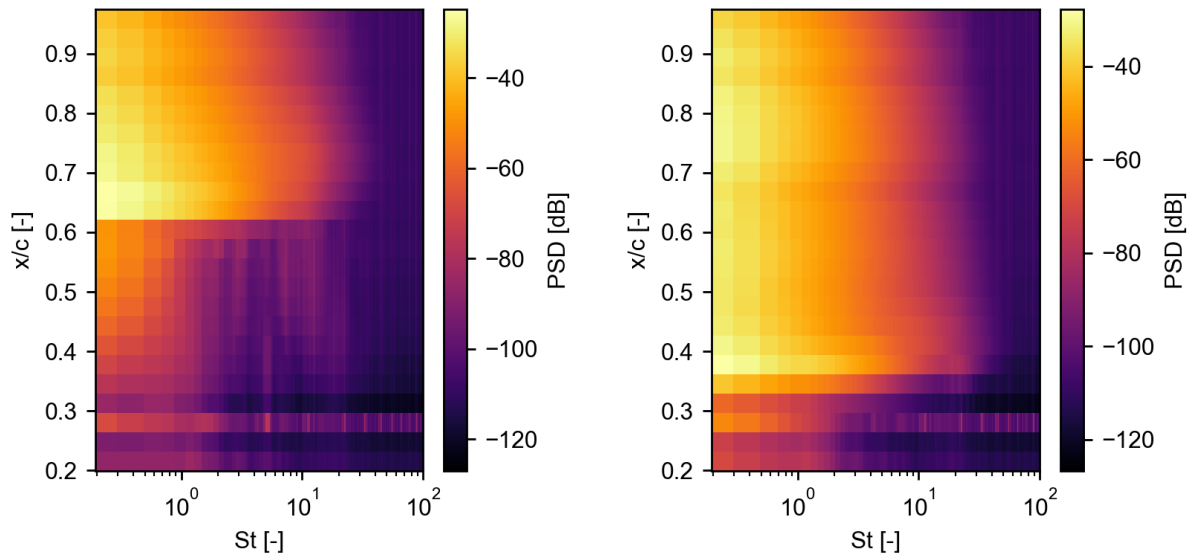

(a) $\alpha = 1$ deg

(b) $\alpha = 5$ deg

Figure 3.7: Power spectra density heatmap in-line piezofoil at $Re = 197,000$, $\Delta T_{pz-\infty} = 25°C$. First two sensors are likely broken, third sensor used for filtering but not removed

of attack or Reynolds number, the emergence of the peak is shifted to more upstream x/c locations and to higher frequencies. The increase in the fluctuations amplitude coincides with the location where the rollers are shed from the shear layer, as will be discussed subsequently. As mentioned in Section 2.4.1, the dimensions of the piezofoil sensing elements result from a trade-off: larger elements provide higher sensitivity but reduced frequency response, whereas smaller elements exhibit the opposite behavior. In the present design, a balance was sought. This explains why, although the frequency response of PVDF is very high, the piezofoil still exhibits a comparatively lower frequency response than other measurement devices of similar sensing element dimensions. This limitation explains the slight negative slope observed in the piezofoil spectra in Figure 3.6, which partially masks the prominence of the vortex-shedding peaks and renders them more difficult to detect. From Figure 3.6 it can also clearly seen how at $\alpha = 1$ degree the vortex shedding peak is less distinctly resolved compared to the $\alpha = 5$ degrees case, as the amplitude of the pressure fluctuations increases with angle of attack.

Figure 3.7 clearly illustrate the increase in amplitude of the pressure fluctuations near reattachment and the negative slope of the spectra discussed above, as the amplitude of the spectra at low frequencies is much higher than at higher frequencies. Though barely, also the vortex shedding peaks can be seen as a slightly more lightly colored areas, especially in the $\alpha = 5$ deg, $Re = 197,000$ case.

The staggered piezofoil, designed to investigate transition and vortex-shedding phenomena in greater detail owing to its higher spatial resolution, successfully captures the peaks associated with vortex shedding and shows good agreement with the in-line piezofoil, as illustrated in Figure 3.8. However, the staggered piezofoil is still affected by the lower frequency response as the in-line piezofoil. An interesting aspect concerns the sensitivity of the staggered sensing elements: toward the trailing edge, some elements exhibit vortex-shedding peaks while adjacent ones do not, resulting in an alternating pattern. For instance, in the case $\alpha = 2$ deg, $Re = 197,000$, where the laminar separation bubble is located closer to the trailing edge, the last sensing element at $x/c = 0.649$ clearly captures vortex shedding, whereas the preceding element does not display a significant peak at the same frequency. Similar behavior is observed in several upstream elements, suggesting that neighboring sensor pairs may not exhibit identical sensitivity. A possible explanation for this behavior can be inferred from the design of the staggered piezofoil. Looking closely at Figure 2.8 it can be seen that the tiny ink traces that transfer the electric charges from the ”out-of-line” sensing elements to the amplifier intersect with the ground ink trace of the ”in-line” sensing elements. This overlap could increase the effective area of the ”out-of-line” elements, thereby enhancing

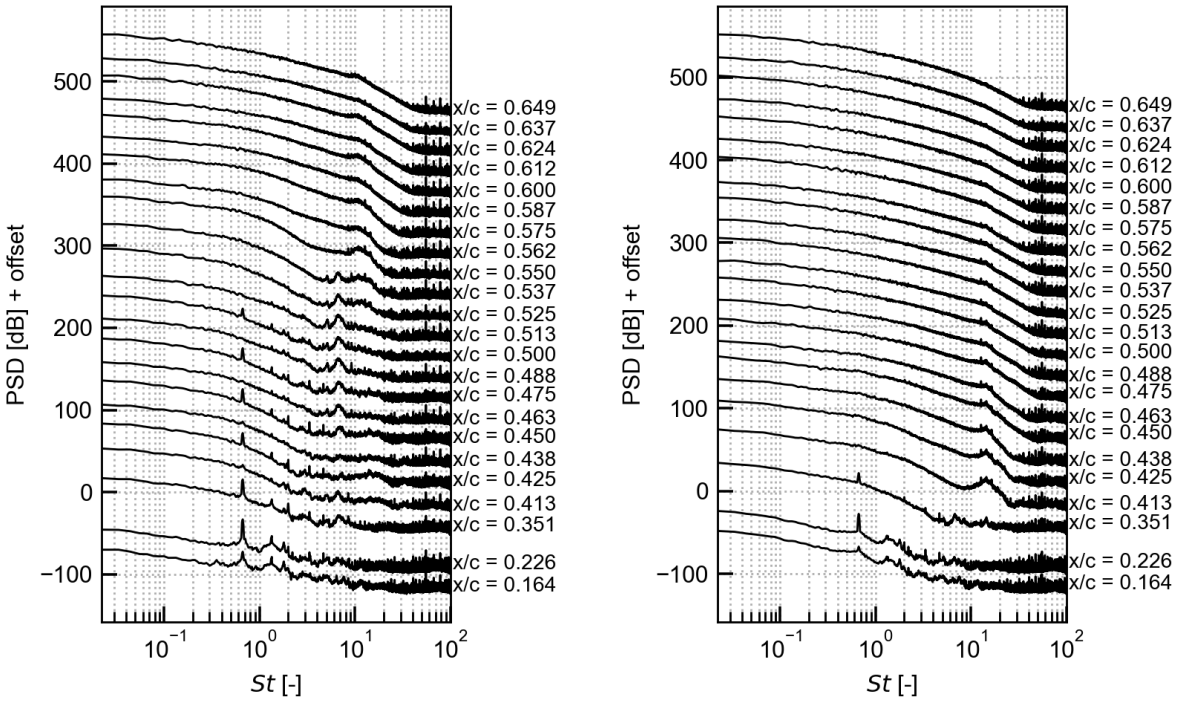

(a) $\alpha = 2$ deg

(b) $\alpha = 4$ deg

Figure 3.8: Power spectra density staggered piezofoil at $Re = 197,000$, $\Delta T_{pz-\infty} = 25°C$. First two sensors are likely broken, third sensor removed because used for filtering

their sensitivity. Furthermore, this configuration could give rise to the formation of a tiny ”secondary sensing element” capable of detecting finer pressure fluctuations associated with smaller vortices that the ”main sensing elements”, due to their larger dimensions, cannot resolve. As a result, the total energy captured may increase.

To get a better idea on the location that records the highest fluctuations, that is the reattachment area, it’s interesting to look at the non-dimensional standard deviation (STD) distribution along the non-dimensional chord length. Figure 3.9 shows the pressure coefficient distribution and the standard deviations of the in-line piezofoil. In the first part the STD is almost zero, due to the very low pressure fluctuations in the laminar boundary layer. Getting past the separation location, the standard deviation slowly start to increase, as the flow instabilities amplify, until reaching the point where a distinct peak is formed. After the peak, the standard deviation decreases and stabilizes around $\sigma/\sigma_t = 1$ which is the STD value of the turbulent boundary layer. The peaks in the standard deviation plots are consistent with the pressure coefficient distributions, although they appear slightly upstream of the estimated reattachment point. This shift arises because the shear layer breaks down at that location, where vortical rollers are formed, leading to strong velocity and pressure fluctuations. This behavior is well documented in the existing literature on laminar separation bubbles [90]–[92]. For instance, analyzing the case at $\alpha = 1$ deg and $Re = 197,000$, the STD shows a peak at $x/c = 0.67$, while the estimated reattachment point from the pressure coefficient distribution lies at $x/c = 0.74$. Thus, the standard deviation peak aligns well with the point that marks the end of the pressure plateau and the start of the pressure rise on the pressure coefficient distribution, just upstream of the reattachment point.

Looking at the standard deviation distribution of the staggered piezofoil, shown in Figure 3.10, there is good agreement with the standard deviation of the in-line piezofoil, especially for the area of the peak. Slight discrepancies are observed in the laminar region, upstream of the reattachment peak, between the two piezofoils. These may be attributed to minor inaccuracies in the installation of the staggered piezofoil, which could introduce small surface irregularities that disturb the flow, resulting in a higher standard deviation than the one expected. Slight differences could also arise due to non-identical and non-uniform heating

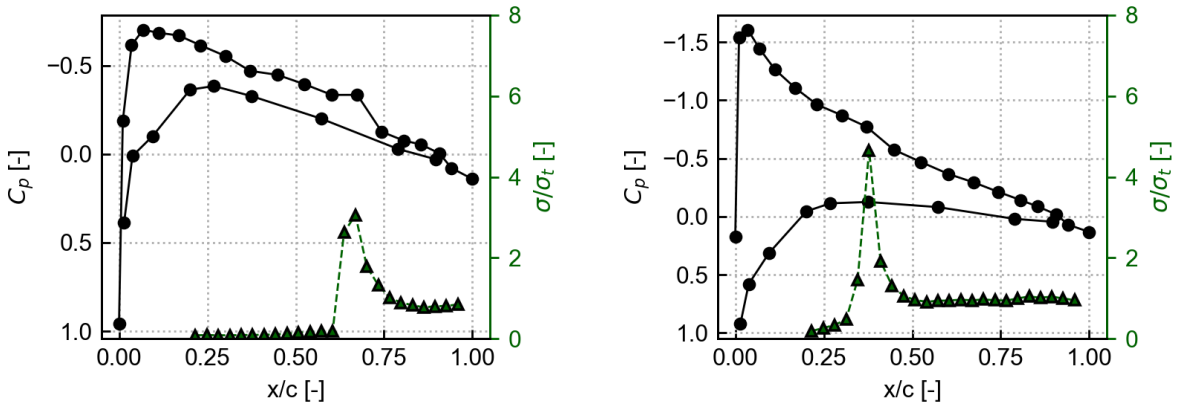

(a) $\alpha = 1$ deg (b) $\alpha = 5$ deg

Figure 3.9: Pressure coefficient distribution and standard deviation in-line piezofoil at $Re = 197,000$, $\Delta T_{pz-\infty} = 25°C$.

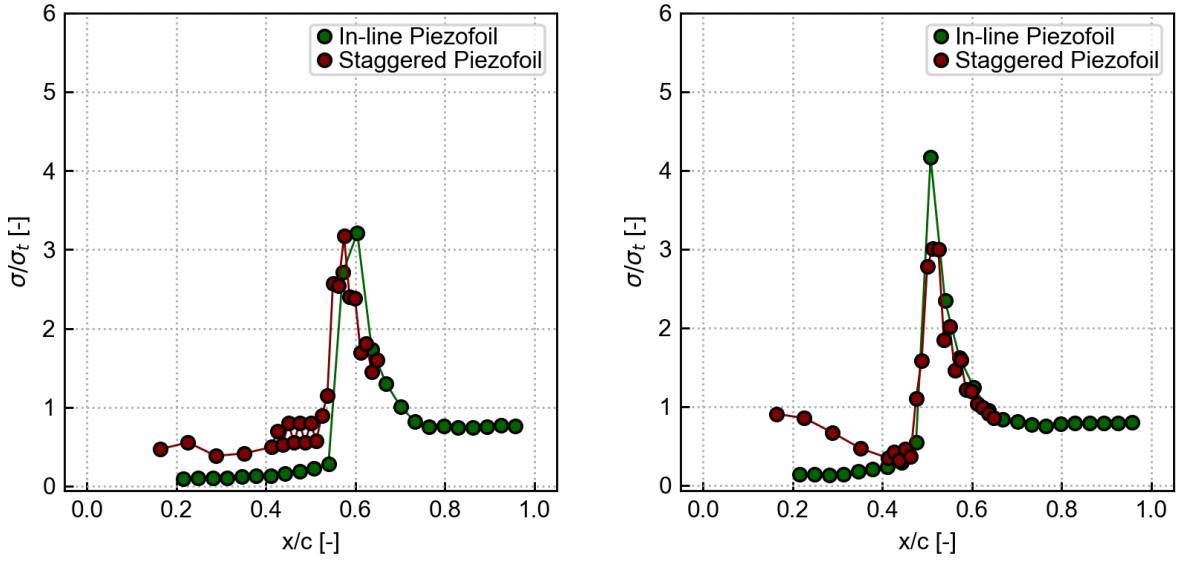

(a) $\alpha = 2$ deg (b) $\alpha = 3$ deg

Figure 3.10: Standard deviation in-line piezofoil and staggered piezofoil at $Re = 197,000$, $\Delta T_{pz-\infty} = 25°C$. First two sensors are likely broken.

of the two piezofoils, producing different sensitivities. An interesting feature observed in the standard deviation of the staggered piezofoil is the presence of minute oscillations measured by adjacent sensors, beginning only from the sixth sensor onward. This behavior is consistent with the trend described earlier in the power spectral density of the staggered piezofoil and further supports the explanation provided in that context, that is the creation of minuscule sensing elements, connected to main ones, forming when a signal trace overlaps with the ground trace.

The shedding of the rollers can also be studied by looking at their convective velocity and at the x/c locations that show the highest correlation. Cross correlation between a sensor mid way between the peak of maximum STD and the trailing edge and all the other sensors is performed to retrieve the time lag associated to specific coherent structures being advected along the wing. The convection speed is then computed knowing the distance between the sensors. The convective motion is inferred from the shift

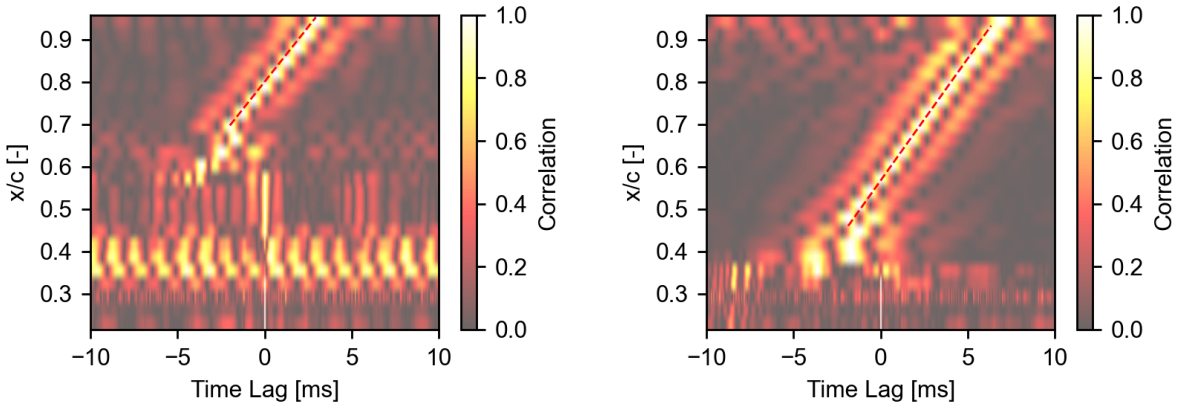

(a) $\alpha = 1$ deg

(b) $\alpha = 4$ deg

Figure 3.11: Cross correlation in-line piezofoil at $Re = 197,000$, $\Delta T_{pz-\infty} = 25°C$. The red dashed line is fit along the location of maximum correlation and its slope coincides with the average convective velocity on the specified portion of the airfoil.

in the location of the correlation peak at different x positions. Figure 3.11 presents the cross-correlation for the in-line piezofoil, and several observations can be made. In the laminar region of the wing, the plot does not exhibit areas of significant correlation, as expected, since the flow lacks coherent structures and the cross correlation maxima mainly lie on the zero time lag line. Some smaller peaks with elevated correlation are present and are likely due to acoustic tones. Further downstream, the cross-correlation map reveals a distinct ridge-shaped feature characterized by high correlation and a positive slope. The points of maximum correlation are identified by light-yellow areas. The locus of the peaks along the ridge (shown in the figure using a dashed line) represents the time delay at which the cross correlation is a maximum for different x/c locations. The correlation peak at a downstream x/c position is obtained by delaying the local signal relative to that measured at the preceding location. This delay represents the average time for flow structures to travel between the two locations and generate a similar correlated wall pressure signal. By calculating the slope of the ridge feature one may estimate the average convection speed (Uc) of the dominant flow structures. Alongside the area of maximum cross-correlation, additional ridge-like features can be observed. These would give the time delay to the highest negative correlation (if the correlation would have been expressed in the range -1,+1), but since the plots are shown only for cross-correlation values between 0 and +1, they appear as regions of positive correlation with slightly lower amplitude.

The appearance of the ridge-shaped feature is in agreement with the location of maximum standard deviation, further confirming its connection with vortex shedding. The peaks of high cross correlation are associated with the advection of coherent structures, namely, the rollers shed from the shear layer, as they convect toward the trailing edge. The slope of the successive peaks does not remain constant and in some cases exhibits a slight S-shaped variation, suggesting reduced convective velocities in the reattachment region and immediately upstream of the trailing edge. In general, the lower velocities observed near reattachment can be attributed to the continued influence of the laminar separation bubble recirculation zone, then, further downstream, as the vortical rollers increase in size, their convection becomes progressively dominated by the freestream velocity, resulting in higher values. Lambert [2] observed a comparable trend on a NACA 0018 airfoil, with convective velocities in the transition region being slightly lower than those measured at and downstream of reattachment. Moreover, his results indicate that the convective velocity is influenced by the merging of successive rollers as well as by the growing disorder associated with the transition to turbulence. The decrease in convective velocity immediately upstream of the trailing edge, observable in some cases, is explained by flow separation occurring in this region, as confirmed by oil-flow visualization. The non-uniformity of convective velocity along the airfoil is expected, since the near-wall velocity varies with flow and surface features. For an airfoil without laminar separation bubbles, the flow near the surface typically decelerates from the suction peak toward the trailing edge, as can also be inferred from typical pressure coefficient distributions.

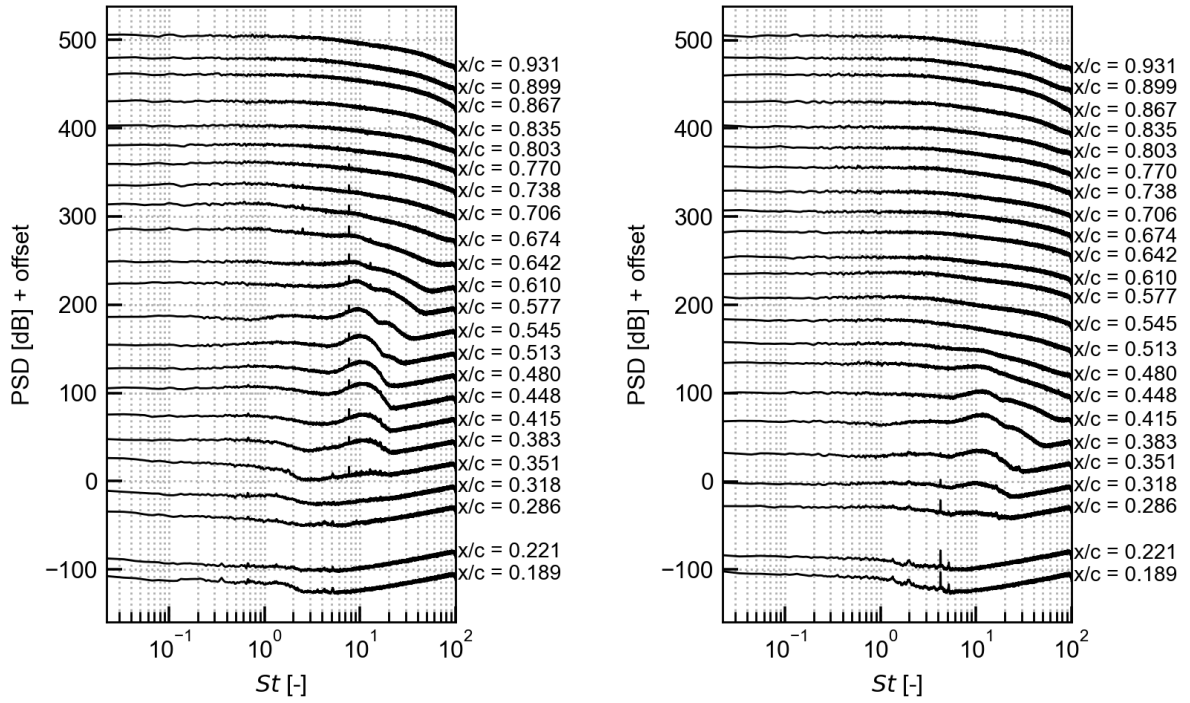

(a) $\alpha = 1$ deg

(b) $\alpha = 3$ deg

Figure 3.12: Power spectra density surface hot wires at $Re = 197,000$. Third sensor has been removed for filtering

The dashed line, obtained by fitting the cross-correlation maxima, extrapolates the average convective velocity beyond the reattachment point. Progressing downstream along the dashed line, the correlation gradually decays, though it remains discernible, reflecting the breakdown and distortion of the rollers during advection. Outside this region of elevated correlation, the plots display values close to zero, as expected. Increases in angle of attack shift the reattachment location upstream and thus, the location where high correlation starts to appear. Increases in Reynolds number not only shift the starting location of high correlation but also produce an increase in the slope of the line, as the convection velocity increases with increases in freestream velocity. The convection velocity derived from the cross-correlation analysis is about $0.66U_\infty$, which falls within the range reported in previous studies. Boutilier and Yarusevych [90] [93] found values ranging from $0.5 - 0.7U_\infty$, and values comprised between $0.5 - 0.8U_\infty$, depending on the angle of attack and the Reynolds number. Their experiments were conducted on a NACA0018 airfoil at a Reynolds number ranging from 50,000 to 250,000 and for an angle of attack range going from 0 to 21 degrees.

3.5. Shear Layer Flapping

Flapping is essentially an up-and-down motion of the separated shear layer at very low frequency that affects the whole shape and dimension of a laminar separation bubble. This phenomenon happens at significantly lower frequencies than vortex shedding and it occurs in an irregular and intermittent fashion and it is probably quantifiable only in a statistical sense [19]. Flapping is driven by altered stability characteristics of the shear layer and its ability to amplify the disturbances and it is due to variations in the incoming disturbances themselves. Thus, flapping is closely connected to vortex shedding in the reattachment area and to the turbulence intensity of the incoming flow [94], [95]. The random incoming disturbances in the flow get amplified in the shear layer and, based on their original amplitude and on the stability properties of the shear layer, they affect in different ways the vortex shedding process. Depending on how vortex shedding is affected, the reattachment process changes, shifting the instantaneous position of the reattachment point, and in turn affecting the mean flow characteristics of the LSB (the diving streamline moves depending on

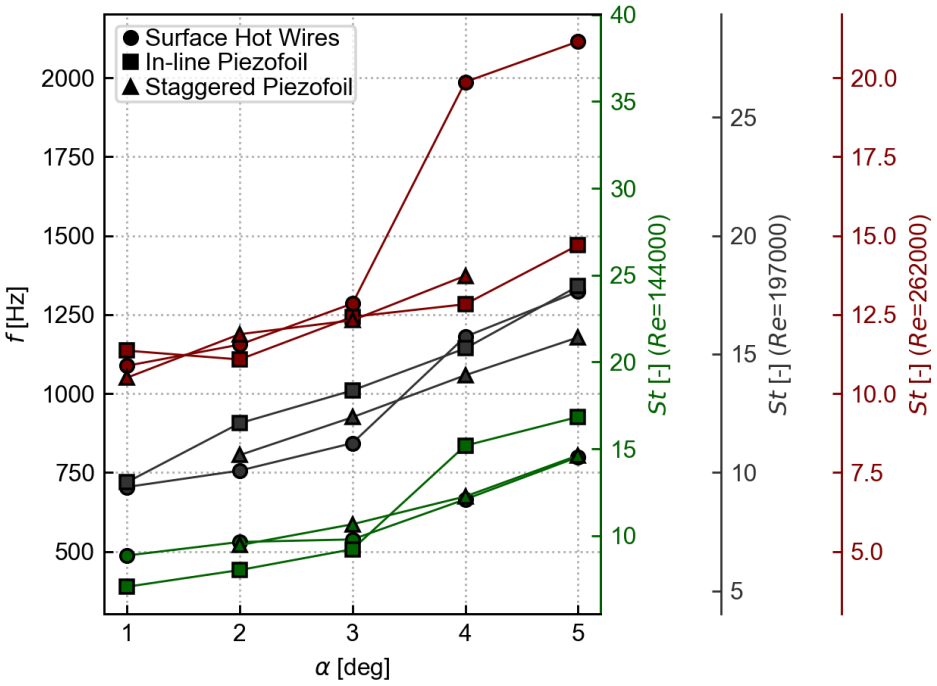

Figure 3.13: Vortex shedding frequencies ans Strouhal numbers at different Reynolds numbers and angles of attack for surface hot wires, in-line piezofoil and staggered piezofoil. In green $Re = 144,000$, in gray $Re = 197,000$, in red $Re = 262,000$.

the changes in the pressure distribution). In other words, a feedback loop creates between the disturbances interacting with reattachment, and affecting the stability characteristics of the shear layer, and the transition location, which affects the amplification of following disturbances [95]. The low frequency movement in the streamwise direction of the shear layer close to reattachment consequently implies low-frequency excursions of the separating shear layer [96]. In literature, slightly different explanations for flapping can be found, such as the one from Tafti et al. [97] where flapping is connected to the entrainment of fluid in the LSB thanks to vortex shedding at reattachment. The transport of fluid upstream in the separation zone causes a gradual rise in pressure in that area with the effect of displacing the shear layer. When the laminar separation bubble is not able to sustain that pressure anymore it collapses, bringing the shear layer back to the starting configuration. Such a mechanism could take place in specific conditions (such as short bubbles and very intense shedding) but seems unlikely to be the main responsible of this phenomenon. Flapping is intermittent and random, as the incoming disturbances are, while vortex shedding is characterized by a more distinct frequency, that would also appear when analysing flapping.

Flapping, as it is strongly connected to the disturbances freestream, is commonly found in experimental studies of laminar separation bubbles, while in numerical simulations it is present only for non-zero values of turbulence intensity [97]. Different levels of turbulence intensity will also affect flapping in different ways. In low turbulence intensity environments there are fewer random incoming disturbances and, when arriving, they will yield evident changes in the pressure distribution and thus on the shear layer position, making flapping more easily recognizable. On the other hand, in high turbulence intensity environments, the random incoming disturbances are extremely frequent, distorting the flow to such an extent that the laminar separation bubble diminishes and stabilizes, with a consequent reduction of flapping [95]. In the frequency spectra, flapping can be recognized as increases in amplitude of the curves at very low frequency in the separation area [98]. Moving downstream from the separation point, the low-frequency increase in amplitude should vanish and the higher-frequency peak connected to vortex shedding should increase and spread over [94], [99]. Flapping is also evident when analyzing the standard deviation distribution along the length of an LSB. On the separated shear layer, the wall-normal velocity standard deviation, but more prominently the streamwise standard deviation present high values [95].

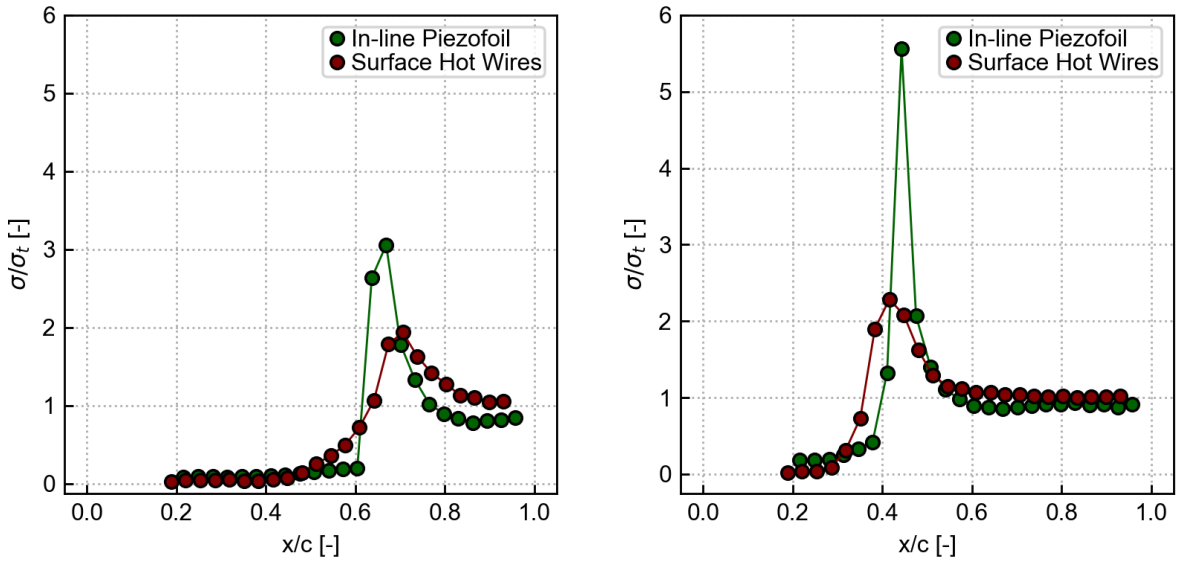

(a) $\alpha = 1$ deg

(b) $\alpha = 4$ deg

Figure 3.14: Non-dimensional standard deviation of surface hot wires (red) and in-line piezofoil (green) at $Re = 197,000$, $\Delta T_{pz-\infty} = 25°C$.

From the measurements analyzed in the present study, no significant signs of flapping can be found and this can be due to different reasons. First and foremost, turbulence intensity. In this study, the turbulence intensity was approximately $TI = 0.14\%$, which is relatively low, though slightly higher than ideal for laminar separation bubble investigations. Studies that have registered flapping show turbulence intensities around $TI = 0.07\%$ [98] and $TI = 0.1\%$ [95], [100]. Another important factor to consider is the sensitivity of the piezofoil: without heating the piezofoil was not able to capture the signals related to vortex shedding, while with heating, vortex shedding could be noticed but far from the frequency resolution of microphones. The pressure fluctuations associated to vortex shedding are considerably higher than the ones related to flapping, hence the difficulty in registering the very low fluctuations of the shear layer moving. It also needs to kept in mind the noise level of the environment, far from ideal. Thus the signal to noise ratio at separation, where the flow is laminar, is considerably worst than at reattachment. Last but not least, an insufficient spatial resolution can also be one of the culprits. If the oscillations of the separation location do not lie close to one of the sensing elements, detecting the already low pressure fluctuations can prove even more challenging.

3.6. Verification and Validation

To validate the piezofoils results, an array of surface hot wires, a well-tested measuring device, is used. Good agreement between the piezofoils and surface hot wires results is found in all the analysis conducted. The main distinction between the surface hot wires and the piezofoil lies in the type of quantity measured: the former records velocity fluctuations, whereas the latter captures pressure fluctuations. This difference has important implications, which will be examined in the present section.

Figure 3.12 shows the power spectral density from the surface hot wires. A very distinct peak can be seen at all angles of attacks and Reynolds numbers, shifting in x/c location and frequency. Moving downstream, the peaks start to be absorbed in the turbulent spectra, as the rollers break up and dissolve. Since the hot wires measure velocity, some differences in the shedding peaks can be observed, namely the presence of double peaks in some of the spectra. This phenomenon can be explained by considering that a single hot wire measures only the magnitude of the velocity vector and is insensitive to flow direction. Within a laminar separation bubble, the flow field is complex and includes regions of recirculation. As a result, some hot wires are located in areas where the flow alternates between upstream and downstream directions. These velocity fluctuations of opposite sign are effectively ”rectified” by the hot wire, which

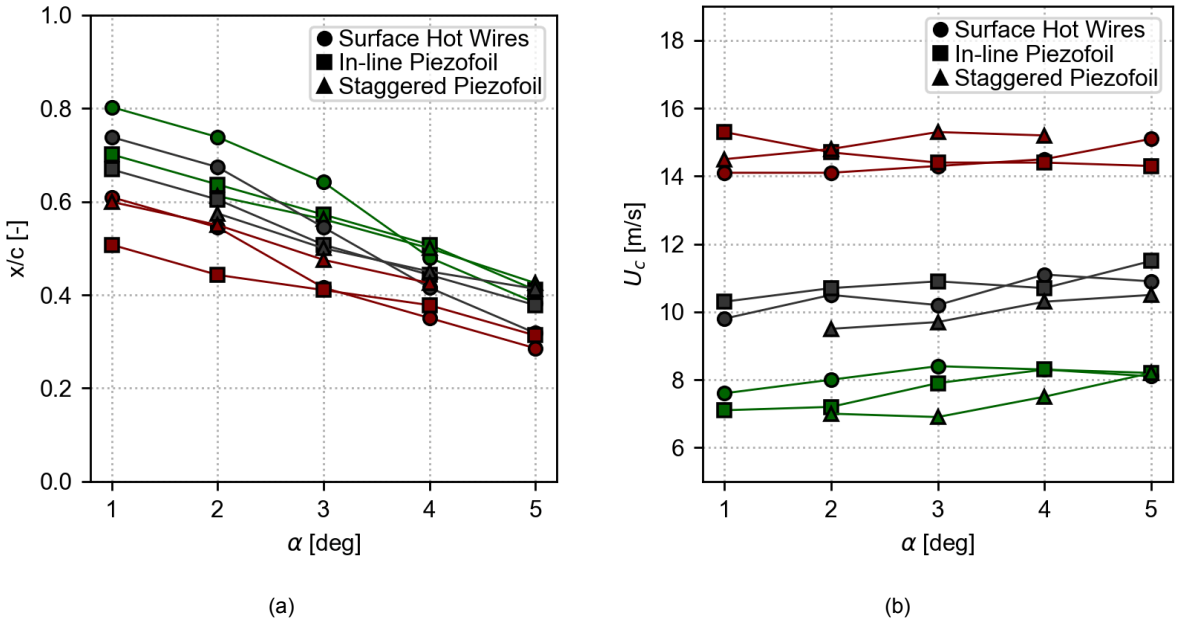

Figure 3.15: (a) Locations of peak standard deviation for surface hot wires, in-line piezofoil and staggered piezofoil. (b) Convection velocities for surface hot wires, in-line piezofoil and staggered piezofoil. In green $Re = 144,000$, in gray $Re = 197,000$, in red $Re = 262,000$.

interprets them all as positive. In a theoretical case where the velocity fluctuations follow a perfect sinusoidal oscillation around zero, the hot wire would output a signal with twice the original frequency due to this rectification. In practice, however, the velocity fluctuations are much less regular, affected by incoming disturbances and flow irregularities, leading to multiple peaks in the spectrum. The ”true” shedding peak is identifiable as the peak appearing always at the same frequency throughout the different x/c positions. Vortex shedding is more pronounced and better resolved by the surface hot wires because these devices measure velocity at a single point in space, that is, they provide a local measurement. In contrast, the piezofoil yields a ”global” measurement, as the pressure it detects is influenced by the flow over a broader area, reflecting the integrated effect of the flow across that region. Moreover, the sensitivity and frequency response is higher than the ones of the piezofoils, enabling the hot wires to capture better the flow features. Figure 3.13 shows the vortex shedding frequencies at different angles of attacks and Reynolds numbers for surface hot wires, in-line piezofoil and staggered piezofoil. The devices show good agreement with only minor discrepancies, especially at the lower angles of attack. At $\alpha = 4, 5$ a sudden increase in vortex shedding frequency is observed in some of the measurement devices. The effect is most pronounced in the surface hot-wire data at $Re = 262,000$, but is also detectable at $Re = 197,000$. A comparable behavior is exhibited by the in-line piezofoil at $Re = 144,000$. The exact cause is not clear and the observed discrepancies may fall within the uncertainty of the measurements. In the case of the surface hot wires at $Re = 262,000$ and $\alpha = 4, 5$ degrees the spectra reveal multiple peaks, which complicate the assessment of the rectification effects and the identification of the true shedding frequency. The present results are consistent with previous findings in the literature. Lambert [2], investigating a NACA 0018 airfoil at $Re = 100,000$ and $\alpha = 5°$, reported a vortex shedding frequency of 650 Hz. Similarly, Kirk and Yarusevych [39] observed a shedding frequency of approximately 250 Hz at $\alpha = 0°$ and about 600 Hz at $\alpha = 5°$ for the same airfoil and Reynolds number. Since the Reynolds numbers considered in the present study are higher, correspondingly higher vortex shedding frequencies are expected. In addition, the airfoils examined here differ slightly from those in the cited studies, which may also contribute to the observed differences.

Examining the standard deviation of the surface hot wires and the in-line piezofoil, as shown in Figure 3.14, reveals excellent agreement, with only minor discrepancies in the exact peak location and magnitude. The difference in location may be attributed to small variations in the laminar separation bubble

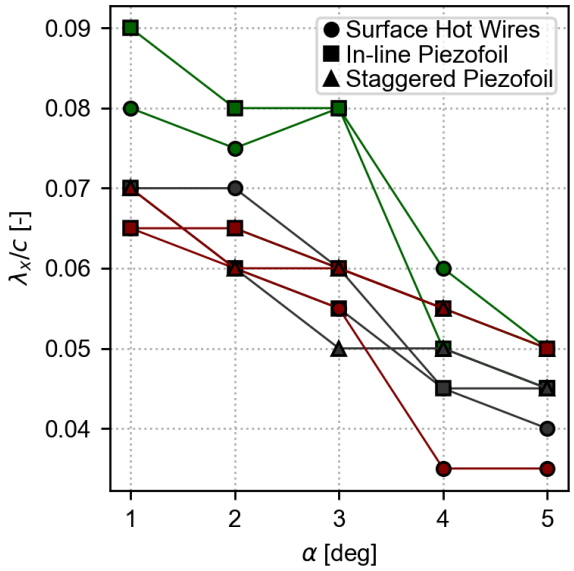

Figure 3.16: Rollers wavelengths computed from convective velocity and vortex shedding frequency for surface hot wires, in-line piezofoil and staggered piezofoil. In green $Re = 144,000$, in gray $Re = 197,000$, in red $Re = 262,000$.

between the two sensor arrays, which are spaced approximately 50 mm apart in the spanwise direction, while the difference in magnitude arises from the different sensitivities of the two devices.

Figure 3.15 (a) presents the locations of maximum standard deviation measured by the three devices across different angles of attack and Reynolds numbers. The maxima occur just upstream of the mean reattachment point, where rollers are shed from the separated shear layer. Overall, the devices show good agreement, particularly at the higher angles of attack. At $Re = 144,000$, the surface hot wires tend to indicate slightly more downstream positions of the maxima at low angles of attack, whereas the in-line and staggered piezofoils remain in close agreement. At the highest Reynolds number, however, the two piezofoils exhibit larger differences: the hot wires agree more closely with the staggered piezofoil at low angles of attack, and with the in-line piezofoil at higher angles of attack.

Figure 3.15 (b) demonstrates that the convection velocity estimated from the three devices are in close agreement, with all indicating values of approximately $0.7U_\infty$. As expected, the convective velocity increases with Reynolds number and shows a slight upward trend with increasing angle of attack. The staggered piezofoil yields lower values at Reynolds numbers of 144,000 and 197,000, while at $Re = 262,000$ it reports values slightly higher than those obtained from the other sensors. These deviations lie within the uncertainty bounds of the measurement techniques and should therefore be interpreted with caution.

Knowing the convective velocity and the vortex shedding frequency, the streamwise wavelength of the rollers can be computed as $\lambda_x = U_c/f_{vs}$. The results are shown in Figure 3.16. The wavelength values range between $0.03 < \lambda_x/c < 0.09$ at different Reynolds number and angles of attack, corresponding to a value of λ_x going from around 6 to 18 mm. This finding is in line with the existing literature. Kurelek et al. [1], Tuna et al. [41] and Michelis et al. [32] found values of $\lambda_x/c \approx 0.05$ m on a NACA 0018 at $Re = 100,000$, $Re = 125,000$ and $Re = 126,000$ respectively. Among the different features, it can be noticed a decrease in wavelength with increases of angle of attack or Reynolds number. This behavior is also confirmed by Lambert [2]. Even though the spacing between sensing elements and hot wires in the in-line piezofoil and surface hot wires is 0.0065 m and, thus in the order of the wavelength, the staggered piezofoil measures similar values, albeit slightly lower. Having the staggered piezofoil a way higher spatial resolution, it should resolve up to smaller wavelengths and with a reduced risk of spatial aliasing. The present study could only investigate the streamwise wavelength λ_x of the rollers and not the spanwise wavelength λ_z, due to the lack of sensors along the span. However, according to the existing literature, the ratio of spanwise to streamwise wavelength should be $\lambda_z/\lambda_x \approx 2$, as already discussed in Section 1.1.5.

4

Conclusions and Recommendations

4.1. Closing Remarks

The research conducted aimed to explore the relevant dynamic phenomena of laminar separation bubbles employing piezoelectric sensors. This section summarizes the main outcomes of the experimental research project. The laminar separation bubble forming on the suction side of a NACA 0015 airfoil at chord-base Reynolds numbers of 144,000, 197,000 and 262,000 has been studied in the boundary layer wind tunnel of the Technische Universität Berlin in a range of angles of attack comprised between 1 and 5 degrees. In total four different measuring techniques have been conducted: static pressure taps and oil flow visualization have been used to characterize the mean flow behavior of the LSB, while two different piezofoil designs have been employed to study the dynamic phenomena of the LSB and surface hot wires have been used to verify the piezofoils results. The suitability of the piezofoils in the laminar separation bubble research is directly linked to the research objective of the thesis, as introduced in Section 1.3, and repeated below for convenience.

Research Objective

Investigate the effects on the surface pressure distribution of the relevant dynamic phenomena in a LSB employing piezoelectric sensors.

To address the research objective stated above, the following research question and subquestions have been answered:

Research Question

How do the pressure fluctuations frequency and amplitude vary in a LSB?

1. What is the streamwise pressure fluctuation distribution in the laminar separation bubble?
2. Can piezofoil and surface hot wires capture shear layer flapping and what is the best location to capture it?
3. Can piezofoil and surface hot wires capture vortex shedding and what is the best location to capture it?
4. Do the velocity and pressure fluctuations match in the reattachment area and, in general, along the length of the LSB?

In general, the baseline characterization of the LSB with pressure taps and oil flow yielded matching results, especially for the reattachment location, while the estimation of the separation location has been hindered by a faulty reading from a pressure tap. Nonetheless, the oil flow provides convincing results also for separation. The transition location could not be estimated due to the fact that the oil flow enables the visualization of the wall streamlines, while transition takes place in the separated shear layer, and due to the insufficient spatial resolution of the pressure taps and to the long tubing between pressure taps and transducer, mostly dampening the pressure fluctuations. For what concerns the dynamic phenomena of the LSB the two piezofoil designs and the surface hot wires are in good agreement. The spectra are similar, with the staggered piezofoil being able to capture more details, due to its increased spatial resolution, and

similar are also the vortex shedding frequencies identified. There is good agreement also on the STD along the airfoils chord, and the point of maximum fluctuations before reattachment is correctly captured. The fact that the shed vortices are adequately resolved is evident also from the cross correlation plots and from the convective velocities computed, showing good agreement between both piezofoils and surface hot wires. Shear layer flapping has not been measured nor with the piezofoils, nor with the surface hot wires.

Specifically addressing the research subquestions, the following remarks can be made.

1. To analyze the streamwise distribution of pressure fluctuations within a laminar separation bubble, it is useful to examine both the standard deviation and the power spectral densities along the non-dimensional chordwise position. The STD reveals very low pressure fluctuations upstream of and immediately after the mean separation point, followed by a slow increase in the fluctuations amplitude and then by a sharp peak just before the mean reattachment location. Beyond this peak, the fluctuations rapidly decrease and stabilize at levels typical of turbulent boundary layers. The sharp rise in STD corresponds to the region where the separated shear layer rolls up, forming vortical structures commonly referred to as ”rollers”. The PSD analysis similarly captures this peak in pressure fluctuation amplitude and further identifies the characteristic frequencies associated with the amplified instabilities and the shedding of vortices. In addition, the spectra confirm the decay of these coherent structures into turbulence downstream of reattachment.
2. With respect to shear layer flapping, nor the piezofoils nor the surface hot wires have been able to provide meaningful data. This behavior may primarily result from the non-optimal sensitivity of the piezofoil, which limits its ability to capture the small amplitude fluctuations characteristic of flapping. Another possible contributing factor is the turbulence intensity during the experiment, which may have been slightly higher than ideal, thus interfering with the accurate detection of the low-frequency flapping motion. For what concerns the surface hot wires, this limitation is linked to the physical quantity they measure. Pressure is a global and continuous variable, whereas velocity is inherently discontinuous and, particularly just downstream of separation, close to zero. This results in a signal-to-noise ratio too low for hot-wire measurements to capture flapping reliably. Consequently, the present study cannot resolve flapping with either piezofoils or surface hot wires, nor can it identify an optimal sensor location. Nevertheless, prior studies suggest that the most suitable measurement region lies near the mean separation location.
3. Concerning vortex shedding, both piezofoils and surface hot wires successfully capture the phenomenon, with close agreement observed among the three devices. The locations of maximum standard deviation of pressure and velocity fluctuations align for all devices within the tested range of angles of attack and Reynolds numbers. Agreement is also observed in the spectra and vortex shedding frequencies, with the exception of $\alpha = 4,5$ degrees at the highest Reynolds number. The cross-correlation analysis further confirms the consistency of the results, yielding comparable convective velocity values. In terms of measurement location, vortex shedding can be effectively characterized throughout the reattachment region and downstream of it. Rollers initiate the roll up just before reattachment and convect downstream while retaining a certain degree of coherence over a considerable distance, in some cases up to the trailing edge. For studies limited to vortex roll-up and shedding frequency, measurements confined to the reattachment region are sufficient. However, investigations into vortex convection and breakdown require a broader measurement domain extending from the mean reattachment location to the trailing edge, depending on the coherence of the vortical structures.
4. Finally, the velocity and pressure fluctuations from surface hot wires and piezofoils, respectively, match well at reattachment and in the LSB. The standard deviation plots clearly show this result. In general, the surface hot wires are able to capture earlier the amplified disturbances and vortex shedding, in respect to the piezofoil. This is related to their different working principles and to their sensitivities.

4.2. Recommendations

Based on the conclusions presented in Section 4.1 the following recommendations are put forward.

1. The wing employed in this study is equipped with 28 pressure taps connected to transducers located outside the model. The spatial resolution is sufficient to characterize long laminar separation bubbles

at low Reynolds numbers and moderate angles of attack, but it does not provide the detail required to resolve shorter bubbles. In addition, the current configuration only enables the analysis of mean flow characteristics, such as pressure coefficient distributions, and cannot resolve the dynamic behavior of the laminar separation bubble. This is due to the long tubing between taps and transducers, which effectively damps pressure fluctuations and preserves only the mean pressure level. This design constraint was imposed by the limited internal space available within the wing model. In future investigations of laminar separation bubbles on wings, a model with a denser spatial resolution of pressure taps is desirable.

2. Since the angle of attack is a critical parameter in the dimensions and behavior of laminar separation bubbles, particular attention must be paid to ensuring its accurate control. In this study, the angles of attack were set by manually rotating the wing and inserting a metal rod into previously drilled holes, whose positions were determined using a digital level. Although this procedure provided satisfactory precision and repeatability, future investigations should employ a more accurate method for controlling the angle of attack, thereby eliminating this parameter as a potential source of uncertainty in measurements taken at nominally identical conditions.
3. The piezofoils design, at the moment, is limited by a number of constraints for what concerns both manufacturing and data acquisition. First and foremost, the manufacturing process only allows screen printing over A4-sized PE sheets, limiting the theoretical maximum dimensions of the foil. Secondly, the dimensions of the sensing elements are constrained by the manufacturing process, since the manual alignment of the layers introduces errors when the elements are made too small. Furthermore, the number of sensing elements is limited by the number of channels in the available amplifier. Transitioning to automated assembly methods could facilitate the fabrication of smaller sensing elements, and the use of an amplifier with a larger number of channels would enable a higher sensor density. However, in the present study, the amplifier was selected primarily for its compact dimensions, as a result of the available space inside the wing model.
4. The limited sensitivity and frequency response observed in the piezofoils can largely be attributed to the dimensions of the sensing elements. As previously noted, a trade-off exists between sensitivity and frequency response: reducing element size enhances frequency response but diminishes sensitivity, whereas larger elements improve sensitivity at the expense of frequency response. Future work should explore the use of smaller sensing elements, within manufacturing constraints, to enhance frequency response, while simultaneously addressing environmental noise reduction. Previous tests conducted in supersonic flows and low-noise environments have demonstrated that the piezofoil performs excellently when operating under high signal-to-noise ratio conditions.
5. The low signal to noise ratio recorded with the piezofoils in unshielded and unheated conditions could also be attributable to the grounding design of the devices. In conjunction with the environmental noise reduction, a redesign of the grounding system might be necessary to increase the signal to noise ratio. The current design presents a ”single ended” configuration where two ground connections are shared among all sensing elements, resulting in separations of several centimeters between the central sensing element and the ground terminals. Redesigning the grounding configuration to employ differential pairs of signal and ground, placing the ground element as close as possible to each sensing element, would theoretically reduce electromagnetic noise contamination in the signal. However, if the existing amplifier configuration is kept, this modification would effectively halve the number of available sensing elements, as each element would require its own dedicated ground connection.
6. In the present configuration, the spanwise distance between the surface hot wires and piezofoil sensing elements is approximately 50 mm. Combined with the manual installation and adjustment of the 3D-printed plug, which may have introduced slight surface differences between the hot-wire and piezofoil locations, this could lead to minor variations in the laminar separation bubble dynamics at the two positions. As a result, coherence analysis between the surface hot-wire and piezofoil signals could not be performed. Future studies should aim to minimize the distance between sensor arrays and, if possible, eliminate the use of insertable plugs, as these can introduce local geometric irregularities that may affect the flow.
7. For the staggered piezofoil, it was observed that overlaps between the signal and ground ink traces may contribute to increased sensitivity. Future research should investigate the development of designs in which each sensing element is divided into two smaller elements with a total area equal

to that of the present configuration. Such an approach would maintain the same overall sensitivity while theoretically enhancing frequency response and energy capture, as the reduced element size would improve the ability to resolve finer-scale flow structures.

8. While modifications to the ground configuration or to the geometry of the sensing elements are expected to yield the largest gains in signal-to-noise ratio, simpler techniques such as heating and signal filtering can also be employed to improve signal quality. In particular, the filtering approach presented in Section 2.8.1 has shown high effectiveness in suppressing common noise by employing a reference sensor and correlating its signal with those of the remaining elements. This method, however, involves the loss of one sensing channel and may inadvertently remove flow-related features, since the reference sensor is located within the flow field. This effect was evident in cases where vortex shedding occurred near the beginning of the piezofoil or of the hot wires plug, as the reference sensor detected the shedding and consequently partially removed it from the other signals during processing. A possible improvement for future studies would be to implement the reference sensing element in the vicinity of the piezofoil connector, inside the wing model, thereby shielding it from the flow while ensuring that it captures the same electromagnetic noise as the rest of the sensors.
9. Although the piezofoil requires only a relatively simple installation procedure, a surface slot is necessary to connect the piezofoils connector to the amplifier. If not properly manufactured, such a slot can introduce noticeable disturbances to the flow. Additionally, on curved surfaces, such as wings, the connector may need to accommodate a double curvature (the external curvature of the wing and the internal curvature required to route the connection to the amplifier), potentially causing the connector to protrude into the flow more than intended. Future studies should account for this constraint during the model design stage or, if not possible, position the slot in flow regions less critical to flow development, such as the trailing edge or the pressure side of the airfoil. This observation is closely related to one of the piezofoil limitations, that is, the fact that it cannot conform to surfaces with double curvature, precluding its application on very complex geometries.
10. In the present work, the two piezofoils could not be rigorously calibrated in their designated calibration chamber due to the large size of the foils. This limitation motivated the use of the on-wing turbulent calibration procedure described in Section 2.4.3. Consequently, the absolute values of the pressure fluctuations could not be obtained. This did not represent a major limitation for the study, as the relative amplitudes of the fluctuations were sufficient for the analysis; however, knowledge of the absolute pressure values would have been useful. Future investigations should therefore consider either developing a larger calibration chamber or adopting an alternative calibration method.

References

[1] J. W. Kurelek, A. R. Lambert, and S. Yarusevych, "Coherent Structures in the Transition Process of a Laminar Separation Bubble," *AIAA Journal*, vol. 54, no. 8, pp. 2295–2309, 2016, ISSN: 0001-1452. DOI: 10.2514/1.J054820.

[2] A. Lambert, "Vortex Dynamics within the Laminar Separation Bubble over a NACA 0018 Airfoil at Low Reynolds Numbers," Ph.D. dissertation, University of Waterloo, 2015.

[3] K. P. Valavanis, Ed., *Advances in Unmanned Aerial Vehicles: State of the Art and the Road to Autonomy*. Dordrecht: Springer Netherlands, 2007, ISBN: 978-1-4020-6113-4 978-1-4020-6114-1. DOI: 10.1007/978-1-4020-6114-1.

[4] Zipline, *About | Zipline Drone Delivery & Logistics*. [Online]. Available: https://www.zipline.com/about.

[5] U. Franke, *Drones in Ukraine: Four lessons for the West*, 2025. [Online]. Available: https://ecfr.eu/article/drones-in-ukraine-four-lessons-for-the-west/.

[6] J. K. Kaldellis and D. Zafirakis, "The wind energy (r)evolution: A short review of a long history," *Renewable Energy*, vol. 36, no. 7, pp. 1887–1901, 2011, ISSN: 0960-1481. DOI: 10.1016/j.renene.2011.01.002.

[7] R. Vos and S. Farokhi, *Introduction to Transonic Aerodynamics* (Fluid Mechanics and Its Applications). Dordrecht: Springer Netherlands, 2015, vol. 110, ISBN: 978-94-017-9746-7 978-94-017-9747-4. DOI: 10.1007/978-94-017-9747-4.

[8] H. P. Horton, "Laminar separation bubbles in two and three dimensional incompressible flow.," Thesis, Queen Mary University of London, 1968.

[9] I. Tani, "Low-speed flows involving bubble separations," *Progress in Aerospace Sciences*, vol. 5, pp. 70–103, 1964, ISSN: 0376-0421. DOI: 10.1016/0376-0421(64)90004-1.

[10] K. L. Hansen, R. M. Kelso, A. Choudhry, and M. Arjomandi, "Laminar Separation Bubble Effect on the Lift Curve Slope of an Airfoil," in *19th Australasian Fluid Mechanics Conference*, Melbourne, 2014.

[11] J. M. Russell, "Length and bursting of separation bubbles: A physical interpretation," Massachusetts Institute of Technology, Department of Aeronautics and Astronautics, Tech. Rep., 1979.

[12] E. Obert, *Aerodynamic design of transport aircraft*. Amsterdam: IOS Press, 2009, ISBN: 978-1-58603-970-7.

[13] G. B. Mccullough and D. E. Gault, *Examples of Three Representative Types of Airfoil-section Stall at Low Speed*, 1951. [Online]. Available: https://ntrs.nasa.gov/citations/19930083422.

[14] S. Pröbsting and S. Yarusevych, "Laminar separation bubble development on an airfoil emitting tonal noise," *Journal of Fluid Mechanics*, vol. 780, pp. 167–191, 2015, ISSN: 0022-1120, 1469-7645. DOI: 10.1017/jfm.2015.427.

[15] E. Benny Thompson and M. Gunasekaran, "Review analysis on laminar separation bubble at low Reynolds numbers," *Journal of Physics: Conference Series*, vol. 2054, no. 1, p. 012 005, 2021, ISSN: 1742-6596. DOI: 10.1088/1742-6596/2054/1/012005.

[16] N. Nati, "Time-resolved 3D PIV analysis of a laminar separation bubble on an unsteady pitching airfoil," Ph.D. dissertation, Technical University of Delft, 2010.

[17] P. R. Owen and L. Klanfer, "On the laminar boundary layer separation from the leading edge of a thin aerofoil," 1955.

[18] O. Marxen, “Viscous-inviscid interaction in laminar separation bubbles,” in *AIAA Scitech 2020 Forum*, ser. AIAA SciTech Forum, American Institute of Aeronautics and Astronautics, 2020. DOI: 10.2514/6.2020-1555.

[19] O. Marxen and D. S. Henningson, “The effect of small-amplitude convective disturbances on the size and bursting of a laminar separation bubble,” *Journal of Fluid Mechanics*, vol. 671, pp. 1–33, 2011, ISSN: 1469-7645, 0022-1120. DOI: 10.1017/S0022112010004957.

[20] U. Rist, “Instability and Transition Mechanisms in Laminar Separation Bubbles,” Tech. Rep., 2003.

[21] E. Reshotko, “Boundary-Layer Stability and Transition,” *Annual Review of Fluid Mechanics*, vol. 8, no. Volume 8, 1976, pp. 311–349, 1976, ISSN: 0066-4189, 1545-4479. DOI: 10.1146/annurev.fl.08.010176.001523.

[22] A. E. Von Doenhoff, *A preliminary investigation of boundary-layer transition along a flat plate with adverse pressure gradient*, 1938. [Online]. Available: https://ntrs.nasa.gov/citations/19930081504.

[23] L. F. Crabtree, “The formation of regions of separated flow on wing surfaces,” Tech. Rep., 1957.

[24] M. Gaster, “The structure and behaviour of separation bubbles,” Tech. Rep., 1967.

[25] M. Dellacasagrande, D. Lengani, D. Simoni, and M. Ubaldi, “An Experimental Database for the Analysis of Bursting of a Laminar Separation Bubble,” *International Journal of Turbomachinery, Propulsion and Power*, vol. 9, no. 1, p. 3, 2024, ISSN: 2504-186X. DOI: 10.3390/ijtpp9010003.

[26] S. Diwan, S. Chetan, and O. Ramesh, “On the Bursting Criterion for Laminar Separation Bubbles,” in *IUTAM Symposium on Laminar-Turbulent Transition*, R. Govindarajan, Ed., Dordrecht: Springer Netherlands, 2006, pp. 401–407, ISBN: 978-1-4020-4159-4. DOI: 10.1007/1-4020-4159-4_57.

[27] T. Michelis, S. Yarusevych, and M. Kotsonis, “Response of a laminar separation bubble to impulsive forcing,” *Journal of Fluid Mechanics*, vol. 820, pp. 633–666, 2017, ISSN: 0022-1120, 1469-7645. DOI: 10.1017/jfm.2017.217.

[28] F. M. White, *Viscous Fluid Flow*. McGraw-Hill Higher Education, 2006, ISBN: 978-0-07-124493-0.

[29] P. K. Kundu, I. M. Cohen, and D. R. D. Ph.D, *Fluid Mechanics*. Amsterdam ; Boston: Academic Press, 2016, ISBN: 978-0-12-405935-1.

[30] U. Rist, U. Maucher, and S. Wagner, “Direct Numerical Simulation of Some Fundamental Problems Related to Transition in Laminar Separation Bubbles,” Institut fur Aerodynamik \ Gasdynamik Universitat Stuttgart, Stuttgart, Tech. Rep., 1996.

[31] T. Michelis, S. Yarusevych, and M. Kotsonis, “On the origin of spanwise vortex deformations in laminar separation bubbles,” *Journal of Fluid Mechanics*, vol. 841, pp. 81–108, 2018, ISSN: 0022-1120, 1469-7645. DOI: 10.1017/jfm.2018.91.

[32] T. Michelis, M. Kotsonis, and S. Yarusevych, “Spanwise flow development within a laminar separation bubble under natural and forced transition,” *Experimental Thermal and Fluid Science*, vol. 96, pp. 169–179, 2018, ISSN: 0894-1777. DOI: 10.1016/j.expthermflusci.2018.02.032.

[33] O. Marxen, M. Lang, and U. Rist, “Vortex formation and vortex breakup in a laminar separation bubble,” *Journal of Fluid Mechanics*, vol. 728, pp. 58–90, 2013, ISSN: 0022-1120, 1469-7645. DOI: 10.1017/jfm.2013.222.

[34] U. Rist and K. Augustin, “Control of Laminar Separation Bubbles Using Instability Waves,” *AIAA Journal*, vol. 44, no. 10, pp. 2217–2223, 2006, ISSN: 0001-1452. DOI: 10.2514/1.17518.

[35] W. Zhang, R. Hain, and C. J. Kähler, “Scanning PIV investigation of the laminar separation bubble on a SD7003 airfoil,” *Experiments in Fluids*, vol. 45, no. 4, pp. 725–743, 2008, ISSN: 1432-1114. DOI: 10.1007/s00348-008-0563-8.

[36] F. Malmir, G. D. Labbio, A. L. Floc’h, L. Dufresne, J. Weiss, and J. Vétel, “Low-frequency unsteadiness in laminar separation bubbles,” *Journal of Fluid Mechanics*, vol. 999, A99, 2024, ISSN: 0022-1120, 1469-7645. DOI: 10.1017/jfm.2024.962.

[37] S. Hosseinverdi and H. F. Fasel, “Laminar-turbulent Transition in a Laminar Separation Bubble in the Presence of Free-stream Turbulence,” *Procedia IUTAM*, IUTAM_ABCM Symposium on Laminar Turbulent Transition, vol. 14, pp. 570–579, 2015, ISSN: 2210-9838. DOI: 10.1016/j.piutam.2015.03.066.

[38] D. Rodríguez, E. M. Gennaro, and L. F. Souza, “Self-excited primary and secondary instability of laminar separation bubbles,” *Journal of Fluid Mechanics*, vol. 906, A13, 2021, ISSN: 0022-1120, 1469-7645. DOI: 10.1017/jfm.2020.767.

[39] T. M. Kirk and S. Yarusevych, “Vortex shedding within laminar separation bubbles forming over an airfoil,” *Experiments in Fluids*, vol. 58, no. 5, p. 43, 2017, ISSN: 1432-1114. DOI: 10.1007/s00348-017-2308-z.

[40] R. Gerakopulos and S. Yaruseyvich, “Novel Time-Resolved Pressure Measurements on an Airfoil at a Low Reynolds Number,” *AIAA Journal*, vol. 50, no. 5, pp. 1189–1200, 2012, ISSN: 0001-1452. DOI: 10.2514/1.J051472.

[41] B. A. Tuna, J. W. Kurelek, and S. Yarusevych, “Surface-Pressure-Based Estimation of the Velocity Field in a Separation Bubble,” *AIAA Journal*, vol. 57, no. 9, pp. 3825–3837, 2019, ISSN: 0001-1452. DOI: 10.2514/1.J058026.

[42] E. Rathakrishnan, *Instrumentation, Measurements, and Experiments in Fluids*. CRC Press, 2007, ISBN: 978-0-8493-0763-8.

[43] S. Tavoularis and J. Nedić, *Measurement in Fluid Mechanics*, 2nd ed. Cambridge: Cambridge University Press, 2024, ISBN: 978-1-009-34362-6. DOI: 10.1017/9781009343657.

[44] G. P. Russo, *Aerodynamic Measurements: From Physical Principles to Turnkey Instrumentation*. Cambridge ; Philadelphia, PA: Woodhead Publishing, 2011, ISBN: 978-1-84569-992-5.

[45] T. G. Beckwith, R. D. Marangoni, and J. H. Lienhard, *Mechanical Measurements*. Addison-Wesley, 1993, ISBN: 978-0-201-56947-6.

[46] Kulite-Semiconductor-Products-Inc., *Kulite pressure transducers distinctively different*. [Online]. Available: https://kulite.com.

[47] Kulite-Semiconductor-Products-Inc, *XCQ-093 Ultraminiature Pressure Transducer*, 2017. [Online]. Available: https://kulite.com/products/product-advisor/product-catalog/standard-version-miniature-pressure-transducer-xcq-093/.

[48] A. M. Hurst, T. R. Olsen, S. Goodman, J. VanDeWeert, and T. Shang, “An Experimental Frequency Response Characterization of MEMS Piezoresistive Pressure Transducers,” American Society of Mechanical Engineers Digital Collection, 2014. DOI: 10.1115/GT2014-27159.

[49] J. B. Barlow, W. H. Rae, and A. Pope, *Low-speed wind tunnel testing*, 3. ed. New York Weinheim: Wiley, 1999, ISBN: 978-0-471-55774-6.

[50] Brüel&Kjaer, *Product Data: Laboratory Standard Microphone Cartridge Types 4160 and 4180*. [Online]. Available: https://www.bksv.com/-/media/literature/Product-Data/bp0459.ashx.

[51] C. Tropea, A. L. Yarin, and J. F. Foss, Eds., *Springer Handbook of Experimental Fluid Mechanics*. Berlin, Heidelberg: Springer, 2007, ISBN: 978-3-540-25141-5 978-3-540-30299-5. DOI: 10.1007/978-3-540-30299-5.

[52] Innovative-Scientific-Solutions-Incorporated, *Fast Pressure Sensitive Paints*. [Online]. Available: https://innssi.com/fast-pressure-sensitive-paints/.

[53] D. Peng and Y. Liu, “Fast pressure-sensitive paint for understanding complex flows: From regular to harsh environments,” *Experiments in Fluids*, vol. 61, no. 1, p. 8, 2019, ISSN: 1432-1114. DOI: 10.1007/s00348-019-2839-6.

[54] S. Mohammadpourfazeli, S. Arash, A. Ansari, S. Yang, K. Mallick, and R. Bagherzadeh, “Future prospects and recent developments of polyvinylidene fluoride (PVDF) piezoelectric polymer; fabrication methods, structure, and electro-mechanical properties,” *RSC Advances*, vol. 13, no. 1, pp. 370–387, 2022, ISSN: 2046-2069. DOI: 10.1039/D2RA06774A.

[55] M. C. Sekhar, E. Veena, N. S. Kumar, K. C. B. Naidu, A. Mallikarjuna, and D. B. Basha, “A Review on Piezoelectric Materials and Their Applications,” *Crystal Research and Technology*, vol. 58, no. 2, p. 2 200 130, 2023, ISSN: 1521-4079. DOI: 10.1002/crat.202200130.

[56] A. Veved, G. W. Ejuh, and N. Djongyang, “Review of emerging materials for PVDF-based energy harvesting,” *Energy Reports*, vol. 8, pp. 12 853–12 870, 2022, ISSN: 2352-4847. DOI: 10.1016/j.egyr.2022.09.076.

[57] C. Moure and O. Peña, “Recent advances in perovskites: Processing and properties,” *Progress in Solid State Chemistry*, vol. 43, no. 4, pp. 123–148, 2015, ISSN: 0079-6786. DOI: 10.1016/j.progsolidstchem.2015.09.001.

[58] J.-F. Li, *Lead-free piezoelectric materials*. Weinheim: Wiley-VCH, 2021, ISBN: 978-3-527-34512-0 978-3-527-81704-7 978-3-527-81707-8 978-3-527-81705-4.

[59] P. Martins, A. C. Lopes, and S. Lanceros-Mendez, “Electroactive phases of poly(vinylidene fluoride): Determination, processing and applications,” *Progress in Polymer Science*, Topical issue on Electroactive Polymers, vol. 39, no. 4, pp. 683–706, 2014, ISSN: 0079-6700. DOI: 10.1016/j.progpolymsci.2013.07.006.

[60] S. Ducharme, T. Reece, C. Othon, and R. Rannow, “Ferroelectric polymer Langmuir-Blodgett films for nonvolatile memory applications,” *IEEE Transactions on Device and Materials Reliability*, vol. 5, no. 4, pp. 720–735, 2005, ISSN: 1558-2574. DOI: 10.1109/TDMR.2005.860818.

[61] N. Ismail, M. Essalhi, M. Rahmati, Z. Cui, M. Khayet, and N. Tavajohi, “Experimental and theoretical studies on the formation of pure β-phase polymorphs during fabrication of polyvinylidene fluoride membranes by cyclic carbonate solvents,” *Green Chemistry*, vol. 23, no. 5, pp. 2130–2147, 2021, ISSN: 1463-9270. DOI: 10.1039/D1GC00122A.

[62] M. Smith and S. Kar-Narayan, “Piezoelectric polymers: Theory, challenges and opportunities,” *International Materials Reviews*, vol. 67, no. 1, pp. 65–88, 2022, ISSN: 0950-6608. DOI: 10.1080/09506608.2021.1915935.

[63] C. Corsi, B. Wang, J. Weiss, and H. D. Ngo, “Development of a PVDF Piezo-Film Sensor for Unsteady Wall-Pressure Measurements in SBLIs,” in *Towards Effective Flow Control and Mitigation of Shock Effects in Aeronautical Applications*, P. Flaszynski, H. Babinsky, and P. Doerffer, Eds., Cham: Springer Nature Switzerland, 2025, pp. 57–72, ISBN: 978-3-031-86605-0. DOI: 10.1007/978-3-031-86605-0_4.

[64] H. Kawai, “The Piezoelectricity of Poly (vinylidene Fluoride),” *Japanese Journal of Applied Physics*, vol. 8, no. 7, p. 975, 1969, ISSN: 1347-4065. DOI: 10.1143/JJAP.8.975.

[65] S. Guo, X. Duan, M. Xie, K. C. Aw, and Q. Xue, “Composites, Fabrication and Application of Polyvinylidene Fluoride for Flexible Electromechanical Devices: A Review,” *Micromachines*, vol. 11, no. 12, p. 1076, 2020, ISSN: 2072-666X. DOI: 10.3390/mi11121076.

[66] M. O. Shaikh, Y.-B. Huang, C.-C. Wang, and C.-H. Chuang, “Wearable Woven Triboelectric Nanogenerator Utilizing Electrospun PVDF Nanofibers for Mechanical Energy Harvesting,” *Micromachines*, vol. 10, no. 7, p. 438, 2019, ISSN: 2072-666X. DOI: 10.3390/mi10070438.

[67] F. Mokhtari, G. M. Spinks, C. Fay, *et al.*, “Wearable Electronic Textiles from Nanostructured Piezoelectric Fibers,” *Advanced Materials Technologies*, vol. 5, no. 4, p. 1 900 900, 2020, ISSN: 2365-709X. DOI: 10.1002/admt.201900900.

[68] P. Shepard, *Implantable Micro-Devices for Self-Charging Pacemakers - News*. [Online]. Available: https://eepower.com/news/implantable-micro-devices-for-self-charging-pacemakers/.

[69] G. Taylor, J. Burns, S. Kammann, W. Powers, and T. Welsh, “The Energy Harvesting Eel: A small subsurface ocean/river power generator,” *IEEE Journal of Oceanic Engineering*, vol. 26, no. 4, pp. 539–547, 2001, ISSN: 1558-1691. DOI: 10.1109/48.972090.

[70] H. Asghari and M. Dardel, “Geometric and structural optimization of fluid energy harvester with high efficiency and bandwidth,” *European Journal of Mechanics - B/Fluids*, vol. 79, pp. 428–443, 2020, ISSN: 0997-7546. DOI: 10.1016/j.euromechflu.2019.10.007.

[71] J. S. Lee, K.-Y. Shin, O. J. Cheong, J. H. Kim, and J. Jang, “Highly Sensitive and Multifunctional Tactile Sensor Using Free-standing ZnO/PVDF Thin Film with Graphene Electrodes for Pressure and Temperature Monitoring,” *Scientific Reports*, vol. 5, no. 1, p. 7887, 2015, ISSN: 2045-2322. DOI: 10.1038/srep07887.

[72] W. Nitsche, M. Swoboda, and P. Mirov, “Shock detection by means of piezofoils,” 1991.

[73] *Wind tunnels - TU Berlin*. [Online]. Available: https://www.tu.berlin/aero/facilities/wind-tunnels.

[74] B. Wang, C. Corsi, T. Weiland, *et al.*, “Screen-Printed PVDF Piezoelectric Pressure Transducer for Unsteadiness Study of Oblique Shock Wave Boundary Layer Interaction,” *Micromachines*, vol. 15, no. 12, p. 1423, 2024, ISSN: 2072-666X. DOI: 10.3390/mi15121423.

[75] C. Corsi, J. Weiss, B. Wang, and H.-D. Ngo, “Wall-pressure measurements in a Mach 2 Turbulent SBLI by Means of a PVDF Piezo-Film Sensor Array.,” in *AIAA AVIATION 2023 Forum*, ser. AIAA AVIATION Forum, American Institute of Aeronautics and Astronautics, 2023. DOI: 10.2514/6.2023-3574.

[76] C. Corsi, *Developing of PVDF Sensor for Unsteady Pressure Measurements - Aero Research Day*, Technische Universität Berlin, 2025.

[77] O. Burkhardt, U. Dinata, C. Warsop, and W. Nitsche, “New Developments in Surface Flow Sensor Technology within the Framework of AEROMEMS,” in *Aerodynamic Drag Reduction Technologies*, P. Thiede, Ed., Berlin, Heidelberg: Springer, 2001, pp. 207–217, ISBN: 978-3-540-45359-8. DOI: 10.1007/978-3-540-45359-8_23.

[78] D. Sturzebecher and W. Nitsche, “Visualization of the Spatial-Temporal Instability Wave Development in a Laminar Boundary Layer by Means of a Heated PVDF Sensor Array,” in *New Results in Numerical and Experimental Fluid Mechanics*, H. Körner and R. Hilbig, Eds., vol. 60, Wiesbaden: Vieweg+Teubner Verlag, 1997, pp. 335–342, ISBN: 978-3-322-86573-1. DOI: 10.1007/978-3-322-86573-1_43.

[79] D. Sturzebecher, S. Anders, and W. Nitsche, “The surface hot wire as a means of measuring mean and fluctuating wall shear stress,” *Experiments in Fluids*, vol. 31, no. 3, pp. 294–301, 2001, ISSN: 1432-1114. DOI: 10.1007/s003480100284.

[80] J. S. Bendat and A. G. Piersol, *Random Data: Analysis and Measurement Procedures*. New York: John Wiley & Sons, 2000, ISBN: 978-0-471-31733-3.

[81] J. Weiss, A. Mohammed-Taifour, and Q. Schwaab, “Unsteady Behavior of a Pressure-Induced Turbulent Separation Bubble,” *AIAA Journal*, vol. 53, no. 9, pp. 2634–2645, 2015, ISSN: 0001-1452. DOI: 10.2514/1.J053778.

[82] A. Celik, L. Bowen, and M. Azarpeyvand, “Experimental investigation on the unsteady surface pressure fluctuation patterns over an airfoil,” *Physics of Fluids*, vol. 34, no. 10, p. 105 134, 2022, ISSN: 1070-6631. DOI: 10.1063/5.0114764.

[83] J. A. Branch, B. Zang, M. Azarpeyvand, D. Jones, E. Jinks, and M. F. Westin, “Steady and unsteady aerodynamic loading of a NACA 16-616 aerofoil in a uniform flow,” *The Aeronautical Journal*, vol. 126, no. 1305, pp. 1897–1923, 2022, ISSN: 0001-9240, 2059-6464. DOI: 10.1017/aer.2022.66.

[84] A. S. Hersh and R. E. Hayden, “Aerodynamic sound radiation from lifting surfaces with and without leading-edge serrations,” Tech. Rep. NASA-CR-114370, 1971.

[85] R. W. Paterson, P. G. Vogt, M. R. Fink, and C. L. Munch, “Vortex Noise of Isolated Airfoils,” *Journal of Aircraft*, vol. 10, no. 5, pp. 296–302, 1973, ISSN: 0021-8669. DOI: 10.2514/3.60229.

[86] S. Pröbstingone, “Airfoil Self-Noise - Investigation with Particle Image Velocimetry,” Ph.D. dissertation, Technical University of Delft, Delft, 2015.

[87] S. Pröbsting, J. Serpieri, and F. Scarano, “Experimental investigation of aerofoil tonal noise generation,” *Journal of Fluid Mechanics*, vol. 747, pp. 656–687, 2014, ISSN: 0022-1120, 1469-7645. DOI: 10.1017/jfm.2014.156.

[88] S. Pröbsting and S. Yarusevych, “Laminar separation bubble development on an airfoil emitting tonal noise,” *Journal of Fluid Mechanics*, vol. 780, pp. 167–191, 2015, ISSN: 0022-1120, 1469-7645. DOI: 10.1017/jfm.2015.427.

[89] R. Gerakopulos, M. Boutilier, and S. Yarusevych, “Aerodynamic Characterization of a NACA 0018 Airfoil at Low Reynolds Numbers,” in *40th Fluid Dynamics Conference and Exhibit*, ser. Fluid Dynamics and Co-located Conferences, American Institute of Aeronautics and Astronautics, 2010. DOI: 10.2514/6.2010-4629.

[90] M. S. H. Boutilier and S. Yarusevych, “Separated shear layer transition over an airfoil at a low Reynolds number,” *Physics of Fluids*, vol. 24, no. 8, p. 084 105, 2012, ISSN: 1070-6631. DOI: 10.1063/1.4744989.

[91] L. Hudy, W. Humphrey, A. Naguib, and S. Bartram, “Wall-pressure-array measurements beneath a separating/reattaching flow region,” in *40th AIAA Aerospace Sciences Meeting & Exhibit*, ser. Aerospace Sciences Meetings, American Institute of Aeronautics and Astronautics, 2002. DOI: 10.2514/6.2002-579.

[92] D. G. Mabey, “Analysis and Correlation of Data on Pressure Fluctuations in Separated Flow,” *Journal of Aircraft*, vol. 9, no. 9, pp. 642–645, 1972, ISSN: 0021-8669. DOI: 10.2514/3.59053.

[93] M. S. H. Boutilier and S. Yarusevych, “Parametric study of separation and transition characteristics over an airfoil at low Reynolds numbers,” *Experiments in Fluids*, vol. 52, no. 6, pp. 1491–1506, 2012, ISSN: 1432-1114. DOI: 10.1007/s00348-012-1270-z.

[94] R. Hain, C. J. Kähler, and R. Radespiel, “Dynamics of laminar separation bubbles at low-Reynolds-number aerofoils,” *Journal of Fluid Mechanics*, vol. 630, pp. 129–153, 2009, ISSN: 1469-7645, 0022-1120. DOI: 10.1017/S0022112009006661.

[95] T. Michelis, “Boundary Layer Separation: Diagnostics and Control,” Dissertation (TU Delft), Technical University of Delft, 2017. DOI: 10.4233/uuid:f5ecca35-71f6-4c99-92e8-a3004113fa53.

[96] F. Malmir, “Numerical Study of Low-Frequency Unsteadiness Phenomena in Laminar Separation Bubbles,” Ph.D. dissertation, Polytechnique Montréal, 2023.

[97] D. K. Tafti and S. P. Vanka, “A three dimensional numerical study of flow separation and reattachment on a blunt plate,” *Physics of Fluids A: Fluid Dynamics*, vol. 3, no. 12, pp. 2887–2909, 1991, ISSN: 0899-8213. DOI: 10.1063/1.858208.

[98] N. J. Cherry, R. Hillier, and M. E. M. P. Latour, “Unsteady measurements in a separated and reattaching flow,” *Journal of Fluid Mechanics*, vol. 144, pp. 13–46, 1984, ISSN: 1469-7645, 0022-1120. DOI: 10.1017/S002211208400149X.

[99] P. G. Wilson and L. L. Pauley, “Two- and three-dimensional large-eddy simulations of a transitional separation bubble,” *Physics of Fluids*, vol. 10, no. 11, pp. 2932–2940, 1998, ISSN: 1070-6631. DOI: 10.1063/1.869813.

[100] K. B. M. Q. Zaman, D. J. Mckinzie, and C. L. Rumsey, “A natural low-frequency oscillation of the flow over an airfoil near stalling conditions,” *Journal of Fluid Mechanics*, vol. 202, pp. 403–442, 1989, ISSN: 1469-7645, 0022-1120. DOI: 10.1017/S0022112089001230.